

Hiroshima University Doctoral Thesis

**Angle-resolved Photoemission
Spectroscopy Study of Many-body
Effects on 3D Topological Insulator
 Bi_2Te_3**

(角度分解光電子分光法による3次元トポロジカル絶縁体
 Bi_2Te_3 の多体効果の研究)

2022

Department of Physical Science,
Graduate School of Science,
Hiroshima University

Amit Kumar

Table of Contents

1. Main Thesis

Angle-resolved Photoemission Spectroscopy Study of Many-body Effects on 3D
Topological Insulator Bi_2Te_3

(角度分解光電子分光法による 3 次元トポロジカル絶縁体 Bi_2Te_3 の多体効果の究)

Amit Kumar

2. Articles

(1) Temperature-dependent band modification and energy dependence of the electron-
phonon interaction in the topological surface state on Bi_2Te_3 .

Amit Kumar, Shiv Kumar, Yudai Miyai, Kenya Shimada

Accepted (12 August 2022), **Physical Review B Letter**

3. Thesis Supplements

(1) Electronic transport studies of Ag-doped Bi_2Se_3 topological insulator.

Shailja Sharma, Shiv Kumar, Amit Kumar, Kenya Shimada, C.S. Yadav

Accepted (16 August 2022), **Journal of Applied Physics**

Main Thesis

HIROSHIMA UNIVERSITY
DOCTORAL THESIS

**Angle-resolved Photoemission Spectroscopy Study of Many-body
Effects on 3D Topological Insulator Bi_2Te_3**

Author: Amit Kumar

Supervisor: Prof. Kenya Shimada

*A thesis submitted in fulfillment of the requirements
for the degree of Doctor of Philosophy
in the*

Department of Physical Science
Graduate School of Science

Higashi-Hiroshima

August 22, 2022

Dedicated
To My Beloved Family and friends

Table of Contents

List of Figures	i
Abbreviation	vii
Abstract	ix
Chapter 1: Introduction to Topological Insulators	1
1.1 Basic Introduction.....	1
1.2 Quantum Topological Phases.....	2
1.2.1 Integer Quantum Hall State	2
1.2.2 Berry Phase and Berry Curvature	5
1.2.3 Chern Number	5
1.3 The Quantum Spin Hall Insulator or 2D Topological Insulator.....	6
1.4 The 3D Topological Insulators	8
1.5 Theoretical Formulation of Topological Insulators	16
1.5.1 Spin-Orbit Coupling	16
1.5.2 TRIM Points	16
1.5.3 Definition of Topological Invariant or Z₂ Invariant	17
Chapter 2: Experimental Background	19
2.1 Single Crystal Growth.....	19
2.1.1 Bridgeman Method.....	19
2.1.2 X-ray Diffraction	21
2.2 Angle-Resolved Photoemission Spectroscopy (ARPES).....	23
2.2.1 Basic Models for ARPES	24
2.2.2 Evolution of Spectral Function	27
2.2.3 Matrix Element Effect	30
2.2.4 Surface Sensitivity of ARPES	32
2.3 Major Component of Laser Based μ –ARPES System.....	33
2.3.1 Sample Preparation for ARPES Measurement	35
Chapter 3: Many-body Interactions	37
3.1 ARPES Spectral Function.....	37
3.1.1 Electron-defect Interactions.....	39
3.1.2 Electron-electron Interactions.....	39
3.1.3 Electron-phonon Interactions	39
3.1.4 A Short Discussion on the Eliashberg Function	40
3.1.5 Evaluation of Coupling Parameter using the Real-part of Self-energy-	42
3.1.6 Coupling Parameter from Imaginary-part of Self-energy	45

3.2 Kramers-Kronig Relation.....	46
3.3 The Electron-phonon Coupling in 3D Topological Insulators.....	47
3.3.1 ARPES Study on 3D TIs.....	48
3.3.2 Helium Atom Scattering Study on 3D TIs	52
3.3.3 Theoretical Studies on TIs	55
Chapter 4: Many-Body Interaction on the Surface of Bi ₂ Te ₃ Crystals.....	59
4.1 Introduction.....	59
4.2 Motivation.....	61
4.3 A short Discussion on the Evolution of Coupling Parameter	62
4.4 Results and Discussion	64
4.4.1 Low Energy Kink Structure	64
4.4.2 Effect of Temperature on the ARPES Band Dispersion	65
4.4.3 Effect of Adsorption/Desorption of Residual Gas Molecules on the TSSs.....	72
4.5 Initial-state Energy Dependence of the EPC Parameter	73
4.6 Temperature Dependence of the Linewidth at the Fermi Level.....	76
4.7 Relaxation Time and Mean Free Path at the Fermi Level	76
4.8 Temperature Dependence Imaginary part of Self-energy	78
4.9 Summary	78
Chapter 5: Conclusion.....	81
References	83
Acknowledgments.....	87

List of Figures

Figures		Page
1.1	Quantum Hall effect (a) An example of an integer quantum Hall effect measurement on InGaAs-based heterostructure in which Hall conductivity σ_{xy} display quantized plateaus at an exact multiple of h/e^2 , figure adopted from ref.[17]. (b) Schematic band structure of a typical insulator and (c) Formation of Landau levels in the presence of the magnetic field, figure adopted from ref. [2].	3
1.2	Chiral edge state at the interface between QH state and insulators. (a) skipping cyclotron orbits in presence of the magnetic field. (b) Electronic band structure of semi-finite band strip band based on Haldane model. A single edge state that connects the valence band and CB, figure adopted from ref. [2]	4
1.3	Quantum Spin Hall effect (a) Depicts a one-dimensional spinless electron transport chain, which has two degrees of freedom: forward (at the upper edge) and backward (at the lower edge) mover, these two degrees of freedom can be represented by symbolic equation $2=1+1$ and separated in QH state. Because of the one-way motion, states are robust, and backscattering is prohibited. (b) depicts a one-dimensional spinful electron transport chain, which has two forward and two backward movers, those are separated in the QH states. Upper edge states have two movers (one forward with up spin and the other backward with down spin) and conversely for lower edge. (c) The scattering of electrons by a nonmagnetic impurity in QSH states adopted two possible paths: clockwise (upper) and counter-clockwise (lower) rotation around the impurity, figure adopted from ref. [7].	7
1.4	Spin polarised band dispersion of Binary $\text{Bi}_{1-x}\text{Sb}_x$, where x is 0.12 to 0.13 on the (111) cleaved surface. Inset shows surface BZ, which represents high symmetry direction. Open circles are used to plot the spin-resolved data, which is then placed on a spin-integrated grayscale diagram. The dispersion curves of spin-up (spin-down) bands are schematically traced by thin (thick) lines, and their spin-up (spin-down) bands are plotted with thin red (thick blue) circles. The dark purple area is the bulk band projection, which is based on ARPES data. At the E_F of $\text{Bi}_{1-x}\text{Sb}_x$ ($x=0.13$), the inset shows a two-dimensional wave-number-resolved photoemission intensity pattern. The $\bar{\Gamma} - \bar{M}$ is represented by the dashed line. This figure is taken from ref.[14].	10
1.5	The Schematic band dispersion of Bi_2Se_3 and Bi_2Te_3 , depicts in (a) and (b), respectively, where Dirac cone-like surface states are in between the bulk bandgap. (c) and (d) Schematic representation of constant energy contours of at E_F for Bi_2Se_3 and Bi_2Te_3 , respectively. Here electron spin is always perpendicular to the wave vector, representing spin-momentum locking. However, Fermi velocity (v_F) is orthogonal to the spin vector for Bi_2Se_3 (figure. c), but to the hexagonal wrapping effect, Fermi velocity (v_F) is not orthogonal to the spin vector for Bi_2Te_3 (figure. d). This figure is taken from ref [14].	11
1.6	Crystal structure of Bi_2Te_3 . (a) crystallographic unit cell, which possesses three quintuple layers (b) depicts in-plane triangular lattice arrangement in one	12

quintuple layer, with three positions A, B, and C. (c) primitive rhombohedral unit cell. (d) The conventional unit cell of Bi_2Te_3 .

1.7	First principle calculation of TIs (a) Schematic band picture of Bi_2Se_3 at Γ point. Here stage (I) shows spitting due to the effect of chemical bonding. On the other hand, stages (II) and (III) represent spitting because of the crystal field and SOC. The dashed line represents the position of E_F . (b) BZ of Bi_2Se_3 , where SBZ are projected on the top. (c) Product of parity at Γ point for the non-trivial topological family. Figures are taken from ref. [9].	15
1.8	ARPES intensity image of Bi_2Se_3 along $\bar{\Gamma} - \bar{M}$ and $\bar{\Gamma} - \bar{K}$ high symmetry directions depict in (a) and (b), respectively. The figure is taken from ref. [29]. (c) depicts ARPES intensity image of Bi_2Te_3 along $\bar{\Gamma} - \bar{M}$ (lower panel) and $\bar{\Gamma} - \bar{K}$ (upper panel) high symmetry directions. The figure is taken from ref. [12].	15
1.9	Depicts the energy states of Kramer pairs. Each Kramer pair states are degenerate at the TRIM points ($k = -k, i.e. k = 0$ and π) due to the periodicity of the Brillouin zone, and this degeneracy is lifted away from the TRIM points, a figure taken from ref. [14].	18
2.1	The schematic picture of our Vertical furnace.	20
2.2	A typical single-crystal Growth profile of Bi_2Te_3 .	20
2.3	The schematic of (a) Bragg's law and (b) X-ray measurement geometry.	21
2.4	Single-crystal X-ray diffraction intensity diagram of Bi_2Te_3 measured at RT.	22
2.5	Refined powder X-ray diffraction data of Bi_2Te_3 : Observed (red circles), calculated (continuous black line), and difference (bottom blue line) profiles obtained after Le-Bail refinement using the $R\bar{3}m$ space group. The vertical bars represent the Bragg peak positions (green).	22
2.6	The schematic of ARPES (a) A basic geometry of ARPES setup, where $h\nu$ in the incident photon energy on the sample, by which electrons are ejected at angles (θ, ϕ) from the sample surface and finally collected by the analyzer. (b) representing the momentum conservation in the photoemission process. (c) depicted energies adopted during the photoemission process, figure adopted from the ref. [47].	25
2.7	The schematic pictorial representation of three-step model.	26
2.8	Interacting and noninteracting case (a) ARPES spectra represents a single electron band crossing across the E_F in (a) non-interaction electron system and (b) strongly interacting electron system, figure adapted from ref. [45].	29
2.9	The schematic diagram of the mirror plane perpendicular to the x - y plane. The figure is taken from ref. [45].	31
2.10	The Universal curve for electron inelastic mean free path in the different elements, figure take from ref. [52].	32
2.11	The schematic of the laser μ -ARPES system (a) depicts the Schematic layout of the laser μ -ARPES system. (b) represents the <i>ex-situ</i> optical focusing	34

	system (c) Schematic diagram of the measurement geometry of the laser-based μ -ARPES system. Figures are taken from ref.[53].	
2.12	The schematic of the single crystal sample geometry mounted inside the ARPES measurement chamber. To ensure the clean surface for measurement, the Ceramic top-post was used to cleave the sample inside the Ultra high vacuum (UHV).	36
3.1	Effect of electron-phonon interaction on band dispersion (a) Schematic representation of band renormalization of the energy band near the E_F , where bare band dispersion ω_0 represented by a dashed line, and solid lines representing the band renormalization $\omega(k)$ at low (blue) and high (red) temperatures. (b) spectral function $A(\omega, k, T)$ representation at low temperature showing sharpening due to band renormalization near E_F . The arrows indicate how the self-energies are related to changes in the band dispersion. The Inset of figure (a) shows self-energies: $Re\Sigma(k, \omega)$ and $Im\Sigma(k, \omega)$ for low (blue) and high (red) temperatures. Figures adapted from ref. [54].	38
3.2	Interband scattering mediated by phonon emission and absorption from a filled circle (final state of the hole) to an open circle (starting state of the hole). Figure adapted from [55].	41
3.3	Self-energies using Debye model (a) Calculated Eliashberg function for Bi_2Te_3 using surface Debye temperature of Bi_2Te_3 , and (b) depicts the $Re\Sigma$ (red) and $Im\Sigma$ (green) part of self-energies calculated using the Debye function at 17K for Bi_2Te_3 , where blue line represents the line on $Re\Sigma$ at E_F and Debye energy $\omega_D (\approx 7meV)$ is the surface Debye temperature of the Bi_2Te_3 .	47
3.4	ARPES spectra of Bi_2Se_3 , measured at various temperatures shown in (a)-(c). Fig. (b) Temperature-dependent $Im\Sigma$ of different cleaved crystals. (c) average of $Im\Sigma$ for all the cleaved samples, EPC parameter evaluated by the gradient fit. Figures adapted from the ref.[57].	49
3.5	ARPES spectra of Bi_2Se_3 , measured at (a) 18 K and (b) 255 K. (c) Low temperature magnified image of left side band from band dispersion depicted in figure 3.5(a), where red line showing evaluated band dispersion from MDC analysis. (c) Temperature-dependent $Im\Sigma$ at E_F for three different samples, where the line represents the gradient fit. Figures adapted from the ref.[58].	50
3.6	ARPES intensity map (a) ARPES spectra of Bi_2Se_3 the $\bar{\Gamma} - \bar{K}$ and $\bar{\Gamma} - \bar{M}$ high symmetry directions at 17 K. (b) MDC along $\bar{\Gamma} - \bar{K}$ direction. Figures (c) and (d) band renormalization (Left side) and extracted self-energies (right side). Figures adapted from the ref.[41].	51
3.7	ARPES spectra of Bi_2Se_3 and Bi_2Te_3 along the $\bar{\Gamma} - \bar{K}$ high symmetry direction at 7 K. Figure (a1)–(a4) corresponds to Bi_2Se_3 , and figure (b1)–(b4) corresponds to Bi_2Te_3 . (a1) and (b1) depict MDC at E_F . (a2) and (b2) depict the Band dispersion map along $\bar{\Gamma} - \bar{K}$ [dashed lines in (a3) and (b3)]. (a3),(b3) Fermi surface map. (a4) and (b4) represent MDC-derived band dispersions near E_F obtained from the data shown in panels (a2) and (b2). The Figures adapted from the ref.[59].	52

3.8	When surface Dirac fermions are taken into consideration, surface phonon dispersion curves along the $\bar{\Gamma} - \bar{M}$ and the $\bar{\Gamma} - \bar{K}$ high symmetry directions look like this: While the estimated surface dispersion curves are shown by black dots, the experimental data are displayed as orange dots with error bars that reflect the instrument resolution. The projection of the bulk bands onto the SBZ is shown by the gray region. Figure adapted from the ref.[60].	53
3.9	HAS measurement on the surface of Bi_2Se_3 . (a) and (b) The energy of a single phonon event as a function of temperature for Sample 1 for Sample 2, respectively. The solid line is a linear fit to the data, and the circles show experimental data. (c) and (d) depict the $\text{Re}\Sigma$ and $\text{Im}\Sigma$ for the isotropic phonon branch, respectively. (e) linewidth due to <i>el-ph</i> scattering. (f) Evaluated EPC parameter using linewidth in figure (f). The figures are adapted from ref.[61].	55
3.10	First principle calculation on Bi_2Te_3 thin films. (a) Phonon DOS $F(\omega)$ for Bulk and for varying thicknesses 1-3 QLs of Bi_2Te_3 (upper panels) and Eliashberg Function $\alpha^2F(\omega)$ of 3 QLs Bi_2Te_3 thin film (bottom panel). (b) Red circles depicted the localized surface phonon modes of the 3 QLs Bi_2Te_3 thin film, and the gray area represents the project of bulk phonon dispersion onto the surface Brillouin zone. Figures adopted from ref.[63].	56
3.11	Band structure calculations of 3 QLs Bi_2Se_3 (a) and 3 QLs Bi_2Se_3 , respectively. The shaded area represents the surface projected bulk states. (c) and (d) depicts the initial energy-dependent magnitude of EPC parameters for Bi_2Se_3 and Bi_2Te_3 , respectively. Solid red circles denote the EPC parameter for the upper Dirac cone and Blue solid circles for the lower Dirac cone. Open red circles denote the intraband contribution for the upper part of the cone, i.e. without coupling to the first bulk-like conduction band. The dashed line represents the DOS. Figures adapted from ref. [64].	57
4.1	ARPES map (a) ARPES intensity plot of Bi_2Te_3 measured along $\bar{\Gamma}-\bar{K}$ at $h\nu=6.3$ eV and at 17 K. (b) MDCs of Bi_2Te_3 along the $\bar{\Gamma}-\bar{K}$ momentum direction. The MDCs at E_F and DP (E_D) are shown in green and red, respectively. (c) Magnified view of the ARPES intensity plot of the rectangle region in Fig. 4.1(a). The solid black line represents peak positions obtained from MDC analyses. (d) Observed Fermi surface at 17 K. (e) Red circles indicate peak positions determined by the MDC analyses. To see the linearity, we plotted a blue dotted line connecting a band point at E_F and a band point at -100 meV.	65
4.2	ARPES map. (a) to (d) APRES results from Bi_2Te_3 at various temperatures, showing the FS (upper panels) and band dispersion along the $\bar{\Gamma}-\bar{K}$ momentum direction (lower panels). Measurements were taken at (a) 17 K, (b) 215 K, and (c) 300 K in the heating process. (d) ARPES result taken at 17 K after RT measurement and re-cooling. The arrows mark the topological surface state (TSS) and CB in the figure.	67
4.3	ARPES intensity map. (a) Band dispersion of sample #2 at 17 K. (b) Temperature-induced energy shift in the E_D . The DP energy (E_D) of sample #1 was determined in the heating process from 17 K to 300 K and that of sample #2 in the cooling process from 300 K to 17 K.	68
4.4	Effect of temperature on TSSs peak width and $-\text{Im}\Sigma(\omega, T)$ of Bi_2Te_3 crystals along $\bar{\Gamma}-\bar{K}$ direction. (a) and (b) illustrates energy-dependent FWHM and the	69

$-\text{Im}\Sigma(\omega, T)$ extracted from MDCs fit by Lorentzian peaks respectively. Red lines represent sample #1 at 17 K measured after 2 hrs of cleave, after that same sample measured at various temperatures up to RT continuously, and yellow lines of sample #1 at 300 K. Thereafter sample was further cooled down to low temperature, and band dispersion was measured again at 17 K after 58 hrs of cleave, as FWHM and the $-\text{Im}\Sigma(0, T)$ shown by blue lines. Green lines represent FWHM and the $-\text{Im}\Sigma(0, T)$ of sample #2 at 17 K, showing similarity with sample #1. Magnitude of FWHM and the $-\text{Im}\Sigma(0, T)$ are very small. Furthermore, as we found, the band dispersion and the $\text{Re}\Sigma$ have no discernible kink structure, implying that electron-phonon coupling is negligible. The intrinsic scattering rate for electron in the TSSs is relatively tiny, as evidenced by these results (small magnitude of $\text{Im}\Sigma$ and no kink structure in the $\text{Re}\Sigma$) [92].

- 4.5 ARPES tilt mapping. (a) Constant energy contours of the Bi_2Te_3 at 17 K were measured after cleavage. (b) Constant energy contours at 300 K in the heating process. 70
- 4.6 Effect of temperature on bulk and surface bands. (a) EDCs of sample #1 at the $\bar{\Gamma}$ point at 17 K (red) and 300 K (green). Solid black lines show the fitting results using a single peak Voight function. (b) The lower panel depicts the energy position of the VB peak (E_{VBP}) and CB bottom (E_{CBB}). The upper panel shows the temperature dependence of the energy difference $\Delta E_1(T) = E_{\text{CBB}}(T) - E_{\text{VBP}}(T)$ at the $\bar{\Gamma}$ point. (c) The temperature-dependent $\left| \text{Im}\Sigma \left(|\vec{k}| = 0, \omega = E_D; T \right) \right|$ at the DP obtained from EDC line widths. The grey shaded areas in (b) and (c) show the reported surface Debye temperature[62]. (d) Plot of $\Delta E_1(T)$ as a function of $-\text{Im}\Sigma(0, E_D; T)$ with a line fit. (e) Temperature dependence of the wave vector (k) and the group velocity (v) at fixed energy (100 meV above the DP). (f) Schematic diagram of effect of temperature on surface and bulk bands. 71
- 4.7 Evaluation of coupling parameter. (a) Evaluated $-\text{Im}\Sigma(\vec{k}, \omega'; T)$ at the initial-state electron energies of 0, 50, and 100 meV obtained from EDC analyses. (b) Evaluated $-\text{Im}\Sigma(\vec{k}, \omega'; T)$ at the initial-state electron energies of 150, 200, and 250 meV obtained from EDC analyses. (c) Evaluated $-\text{Im}\Sigma(\vec{k}, \omega'; T)$ at the initial-state electron energies of 50, 100 and 150 meV obtained from the MDC analyses. 74
- 4.8 Initial energy-dependent EPI coupling parameter. (a) The upper panel shows the EPI coupling parameter as a function of initial-state electron energy with respect to the DP obtained from EDC analyses (open red circles) and MDC analyses (filled red circles). Stars in blue represent the theoretical EPI coupling parameter extracted from ref. [64]. The lower panel illustrates the experimental $-\text{Im}\Sigma(\omega, T)$ at 17 K (red), theoretical DOS (blue), and angle-integrated photoemission spectra (AI-PES in green). (b) Constant energy contours at 17 K showing the appearance (left) and disappearance (right) of the VB maximum. Energies are measured from the DP. (c) ARPES intensity plot along $\bar{\Gamma}-\bar{M}$ at 17 K. 75
- 4.9 Temperature dependence of the linewidth at E_F , $-\text{Im}\Sigma(0, T)$, for two different Bi_2Te_3 samples. Red solid circles and green diamond-like solid shapes denote sample #1 and sample #2, respectively. The lower panel represents the magnitude of the $-\text{Im}\Sigma(0, T)$ of two different samples that overlap. On the 77

other hand, the middle and upper panels represent line fit in the temperature-dependent $-\text{Im}\Sigma(0, T)$ at E_F of sample #1 and sample #2, respectively.

- 4.10 Relaxation time (lower panel) and mean free path (upper panel) at the E_F of two samples evaluated from the temperature-dependent ARPES spectra. Red solid circles and green diamond-like solid shapes are used for sample #1 and sample #2, respectively. The magnitude of the relaxation time and mean free path are almost constant with temperature, implying a negligible change in the scattering at elevated temperatures. 77
- 4.11 Imaginary part of the self-energy ($-\text{Im}\Sigma(\omega, T)$) at various temperatures. The arrow highlights that the peak in $-\text{Im}\Sigma(\omega, T)$ is shifting towards E_F with increasing temperature. We use a vertical offset for better visibility. 78

Abbreviation

APRES	Angle resolved photoemission spectroscopy
BZ	Brillouin zone
CB	Conduction band
DFQ	Dirac Fermion Quasiparticle
DOS	Density of states
DP	Dirac point
E_D	Dirac point energy
E_F	Fermi level
EPC	Electron-phonon coupling
EPI	Electron-phonon interaction
FQHE	Fractional Quantum Hall effect
FS	Fermi surface
IQHE	Integer Quantum Hall effect
QAHE	Quantum Anomalous Hall effect
QL	Quintuple layer
QSHE	Quantum Spin Hall effect
SBZ	Surface Brillouin zone
SOC	Spin-orbit coupling
STS	Scanning Tunnelling Spectroscopy
TRIM	Time-reversal-invariant momenta
TRS	Time reversal symmetry
TSS	Topological surface states
VB	Valance band

Abstract

Topological Insulators (TIs) are a fascinating class of materials that sparked renewed interest in the topological aspects of condensed matter physics. TIs have a gap that separates valance and conduction bands in bulk, but they are distinct from conventional insulators because they have the conducting states at edges or surface, so-called topological edge states or topological surface states (TSSs) inside the gap. These metallic TSSs inside the bulk bandgap of TIs degenerate at the time-reversal invariant momentum (TRIM) and exhibit a Dirac-fermion-like linear dispersion away from the TRIM. The degeneracy at the TRIM is protected by the time-reversal symmetry, which is robust against the scattering by nonmagnetic disorders or crystal defects. Furthermore, the electron spin and momentum directions of the TSSs are locked due to the strong spin-orbit coupling (SOC), which is so-called spin momentum locking. Hence the electron spin direction forms a nontrivial spin texture in the momentum space. Although the helical spin texture of the TSS suppresses the backscattering by the nonmagnetic impurities or lattice defects, there is always the possibility to exist electron-phonon scattering at elevated temperature (due to excitation of phonons at elevated temperature). As the scattering phenomena are directly related to the materials' transport properties, it is indispensable to clarify the electron-phonon interaction in the TIs at elevated temperatures.

In this study, we have chosen the prototypical three-dimensional solid (3D) TI Bi_2Te_3 , the second most studied TI. We have grown Bi_2Te_3 single crystal using the modified Bridgeman method. After the X-ray phase characterization, we systematically investigated the electron-phonon interaction using high-resolution angle-resolved photoemission spectroscopy with focused laser light. We did not observe band renormalization, the so-called kink structure within the Debye energy range at low temperature, indicating weak electron-phonon coupling. As we did not find kink structure at low temperature, we ran detailed temperature-dependent angle-resolved photoemission spectroscopy measurements. We found that the Dirac point

(DP) is shifting upward on heating; however, the DP position is fully recovered at low temperature after the temperature cycle, which confirms the reproducibility. By analyzing the temperature-dependent energy distribution curves, we confirmed for the first time that the temperature-dependent modification of the bulk and the topological surface bands are non-rigid-band-like. We evaluated the electron-phonon coupling parameter at fixed initial energy with respect to the DP. We revealed that the magnitude of the electron-phonon coupling parameter weakly depends on the chosen initial energy state, which is consistent with the first-principle calculation. Our study may provide a deep insight into the doping-dependent transport properties derived from TSSs of Bi_2Te_3 . To clarify the mechanism of superconductivity of Bi_2Se_3 observed upon intercalation with Cu, Sr and Nb, our analysis method can be helpful in examine the role of the electron-phonon interactions in these superconductors. The most important advantage of our analysis method could be that instead of growing many samples with differently tuned chemical potential, one can extract electron-phonon coupling information by choosing the initial-electron state of one sample.

Chapter 1: Introduction to Topological Insulators

1.1 Basic Introduction

One of the essential goals of condensed matter physics is to discover a new state of matter and its classification. In particular, ordered phases such as solids, magnets, and superconductors can be classified by spontaneous symmetry breaking based on Landau's principle; for example, structural phase transitions of solids can be identified by breaking a specific symmetry operation, while magnetic transitions break rotational symmetry of spins. On the other hand, the superconducting transition can be distinguished by gauge symmetry breaking. In addition, solids can be classified into the three states of matter, namely, 1) metals, 2) insulators, and 3) semiconductors/semimetals. These three states can be easily distinguished based on the size of the bandgap between the valence bands (VBs) and conduction bands (CBs) based on the band theory of solids. According to the band theory, an insulator can be defined by filled VBs and empty CBs. The VB maximum and CB minimum energy difference is called a *bandgap*. Because of the large bandgap, electronic conduction is prohibited in insulators unless applied perturbations energetically overcome the bandgap. The conventional insulators are called topologically trivial insulators [1,2]. However, in 1980 von Klitzing *et al.* [3] discovered a new state of matter in a 2D semiconductor that does not fit into the previously known spontaneous symmetry-breaking paradox according to Landau's theory. The most exciting property of the new state is that the material is insulating in the bulk while dissipationless current flow occurs at the sample edges. More surprisingly, these materials show very precise quantized conductivity. This new state is called Quantum Hall (QH) state and this effect is called Quantum Hall Effect (QHE). Moreover, this quantized conductivity was independent of sample size and disorder. Therefore, it was recognized that this is attributable to the topology of the sample. However, the QH state was generally realized at a very low temperature ($\sim 1.5\text{K}$) and very high magnetic field ($\sim 18\text{T}$), which involves a high cost for commercial use [4]. This specific environment limits its further development. But still, this new discovery gave a dream to discover QH without extreme environments. Finally,

Kane & Mele in 2005 [5] and Bernevig & Zhang in 2006 [6] independently proposed Quantum Spin Hall (QSH) state or 2D Topological Insulator (TI). Later in 2007 [7], the QSH effect was experimentally realized in the HgTe QWs; it shares some similarities with the QH state but also has many quantitative differences. The discovery of the QSH effect was the announcement of the beginning of TIs research. The QSH can reveal an electronic edge state similar to the QH due to the inherent nature of strong spin-orbit coupling (SOC) rather than the external magnetic field. The discovery of the QSH has sparked new debate and a spike in modern condensed matter physics. Shortly after the discovery of the 2D TIs, Fu and Kane [8] predicted that the alloy $\text{Bi}_{1-x}\text{Sb}_x$ could be a 3D TI in the selected range of composition x , and consequently experimentally confirmed by Hasan's group using angle-resolved photoemission spectroscopy (ARPES). Later Zhang *et al.* [9] predicted several 3D TIs such as Bi_2Te_3 , Bi_2Se_3 , and Sb_2Te_3 . Soon after experimentally realized by several groups independently [10-12].

The main goal of this chapter is to provide an outline of TIs, as well as a brief review of theoretical concepts, phenomenology, and some details of new Quantum states and their classifications based on excellent comprehensive topological reviews [2,7,13-16].

1.2 Quantum Topological Phases

1.2.1 Integer Quantum Hall State

After discovering the Hall Effect (HE) in 1879, a new quantum state of matter called the Integer Quantum Hall effect (IQHE) was discovered in 1980. Like the Hall effect, von Klitzing *et al.* [3] passed current across one of the planar directions of the 2D electron gas sample, and a magnetic field was applied perpendicular to the plane. As a result, voltage generates in the transverse direction, as in the Hall effect experiment. However, the occurrence of IQHE is limited to the high magnetic field and very low temperature, which results in electron localization along with quantized Landau levels, leading to remarkable quantized Hall conductivity (σ_{xy}) and zero longitudinal conductivity ($\sigma_{xx} = 0$).

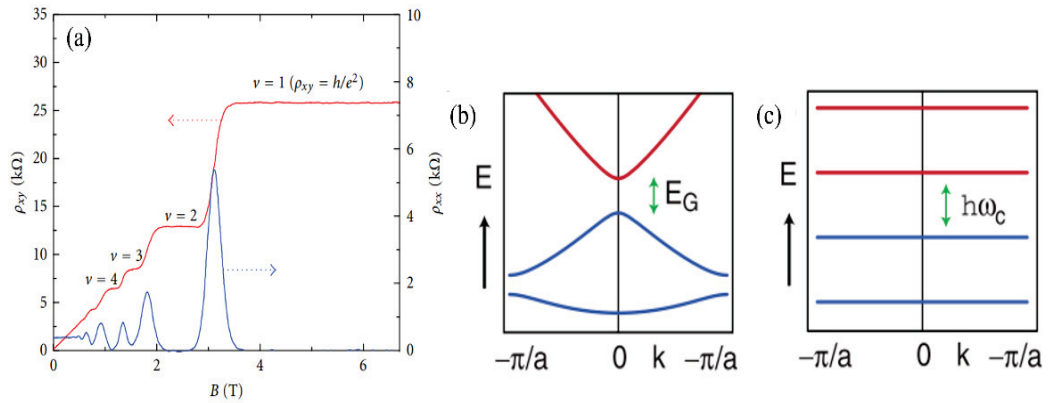


Figure 1.1: Quantum Hall effect (a) An example of an integer quantum Hall effect measurement on InGaAs-based heterostructure in which Hall conductivity σ_{xy} displays quantized plateaus at an exact multiple of h/e^2 , figure adopted from ref. [17]. (b) Schematic band structure of a typical insulator and (c) Formation of Landau levels in the presence of the magnetic field, figure adopted from ref. [2].

The quantized Hall conductivity (σ_{xy}) is given as,

$$\sigma_{xy} = \nu \frac{e^2}{h}, \quad (1.1)$$

Where ν , e , and h are integer values, electron charge, and Planck constant, respectively. The ν is also known to be the Chern number. The more interesting fact is that this quantization of Hall conductivity is measured highly accurately to 1 part in 10^9 [3] and is unaffected by the presence of disorders such as crystal defects. The reason for this accuracy is the motion of electrons in the presence of a magnetic field. When a perpendicular magnetic field is applied to the 2D electrons gas, electrons start rotating in the circular cyclotron orbits due to Lorentz force, and the radius of orbits decreases with increasing magnetic field. For a large magnetic field, electrons in bulk localized (form small, closed circular orbits), make energy levels discrete and quantized, which leads to an insulating character in the bulk because the Fermi level (E_F) lies in the middle of two Landau levels. Electrons near the edges, on the other hand, cannot complete their orbits because of scattering from the boundary; therefore, electrons skip their motion along the edges, forms a one-dimensional moving channel *called* conducting chiral edge states. Therefore, electrons have only unidirectional motion along the edges, even if some impurity or crystal disorder is present in the path of electron motion; still, the electron will bypass these defects due to unidirectional motion along the edges. Fig. 1.2(a)

represents the motion of 2D electrons, and Fig. 1.1(a) and (c) the quantization of energy levels in the presence of a High magnetic field. The theory of Landau quantization explains the discrete and quantized energy levels when electrons are subjected to a magnetic field, as shown in Fig. 1.1(c). Analogous to a quantum harmonic oscillator, the energy eigenvalues of Landau levels are,

$$E_\nu = \hbar\omega_c \left(\nu + \frac{1}{2} \right) \quad (1.2)$$

where, $\omega_c = eB/m$ is the cyclotron frequency. After the discovery of IQHE, Laughlin predicted the fractional quantum Hall effect (FQHE) in 1982 [18], and soon Tsui *et al.* confirmed it experimentally in the 2D electron gas system GaAs/AlGaAs [19]. The FQHE is the phenomenon in which transverse conductivity (σ_{xy}) shows precisely accurate quantized plateaus at the fractional value of ν in equation (1.1). This FQH state is also known as a new quantum state of matter.

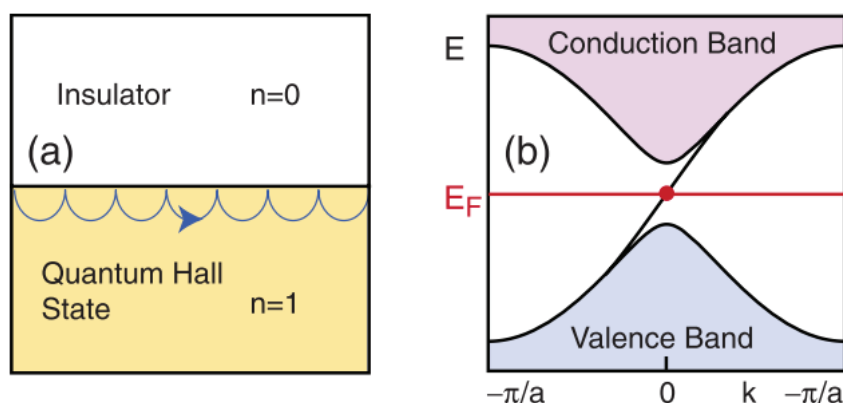


Figure 1.2: Chiral edge state at the interface between QH state and insulators. (a) skipping cyclotron orbits in the presence of the magnetic field. (b) Electronic band structure of semi-finite band strip band based on Haldane model. The figure adopted from the ref is a single edge state connecting the valence band and CB. [2].

Later, Haldane theoretically proposed the Chern insulator [20], which shares short similarities with the QH state. Like the QH state, the Chern insulator shows edge states with nonzero Chern number, but no external magnetic field is needed to realize the insulating bulk. In 2013, He *et al.* [21] also theoretically predicted the Chern Insulator state in the 3D Z_2 Topological Insulators by external magnetic doping, where time-reversal symmetry is broken due to magnetic dopant and no

external magnetic field is required. Such Chern insulators are also called Quantum anomalous Hall effect (QAHE), and this effect is experimentally observed in thin films of Cr doped $(\text{Bi}_{1-x}\text{Sb}_x)_2\text{Te}_3$ [21]. The Chern insulator shows a single-edge state that links the valence band with the CB, as shown in Fig.1.2(b).

1.2.2 Berry Phase and Berry Curvature

Berry delivered one of the most fundamental ideas in the Topological matter field, named the Berry phase [22]. The original basis for Berry's phase is based on the adiabatic approximation of quantum mechanics, which deals with the system linked to a slowly changing environment. In the adiabatic approximation, the Hamiltonian of the system is changed slowly with time, and the system remains in its ground state. Berry Phase (Φ) is just a geometrical phase factor of the eigenstates which undergoes the adiabatic approximation in a closed cycle and is defined as

$$\Phi = \oint_C A_n \cdot dk \quad (1.3)$$

Using Stokes' theorem, one can write the Berry phase as

$$\Phi = \oint_S (\Delta \times A_n) \cdot dk^2 = \oint_S \mathcal{F}_n \cdot dk^2 \quad (1.4)$$

where, A_n is called Berry connection and defined as

$$A_n = -i\langle u_n(k) | \Delta_k | u_n(k) \rangle. \quad (1.5)$$

The connection is a mathematical notion in differential geometry. Here, it is defined in the momentum space under the adiabatic cycle. $\mathcal{F}_n = (\Delta \times A_n)$ is called Berry curvature, analogous to electromagnetism's magnetic field (curl of vector potential).

1.2.3 Chern Number

In the case of IQHE, it is worth noting that the quantization phenomenon in Hall conductivity was predicted theoretically as early as 1974 [23]. Later Thouless, Kohmoto, Nightingale, and den Nijs (TKNN) noticed in 1982 that this phenomenon is not just Quantum mechanical but also topological [24]. TKNN explained that k -space is mapped to a topologically nontrivial Hilbert space in a quantum Hall

system, its topology can be described by an integer topological invariant known as the TKNN invariant ν , and Hall conductivity (σ_{xy}) becomes ν times e^2/h , and this TKNN invariant ν also known as winding number or first Chern number, is equal to Berry phase around the boundary of 2D Brillouin zone (BZ) divided by 2π [14],

$$\nu = \sum_n \nu_n = \frac{1}{2\pi} \oint_{BZ} \mathcal{F}_n \cdot dk^2, \quad (1.6)$$

where, ν_n is the total Chern number, the sum of invariants over occupied states and attain only integer value. As a result of this fact, σ_{xy} is quantized to integer multiples of e^2/h . This Chern number ν plays a significant role in the IQH system and serves as a topological invariant and thus establishes the topological nature of IQH systems.

1.3 The Quantum Spin Hall Insulator or 2D Topological Insulator

The discovery of the new QH state was the premise of the TIs field and gave hope for dissipationless electronic applications. However, a high magnetic field and low-temperature requirement limit its applicability. Later Chern insulator was realized, which did not require an external magnetic field, but internal magnetization still breaks time-reversal symmetry (TRS) in Chern insulators. Can we construct a similar QH-like topological state, which does not require an external magnetic field and preserved TRS? Such motivation derives from the theoretical prediction of Quantum Spin Hall (QSH) insulator or Topological Insulator. Kane and Mele [5] proposed the QSH insulator, followed by Bernevig and Zhang's independent proposal [6]. In general, The QSH insulators effectively superimpose two quantum Hall systems with the spin-polarized chiral edge states. The two states form a time-reversed pair to preserve the total TRS. In each copy of the QH state, the effective magnetic field breaks TRS, but TRS is preserved in the combined version. The reason for this is that the TRS flips the spin direction as well as the magnetic field's direction. To preserve TRS in this scenario, an up-spin electron (for example) traveling clockwise must match with a spin-down electron traveling counter-clockwise, which is indeed the case here [7]. As a result, it turns out that this type of effective magnetic field, which has an opposite sign for opposite spins, can produce due to spin-orbit interaction; in fact, SOC plays a role in the magnetic

field as needed in QHE, and opens a gap in the bulk electronic structure and separate the gapless edge states in presence of TRS. Hence, Chiral spin phenomena on QSH states are the consequence of SOC, hence the consequence of heavier elements.

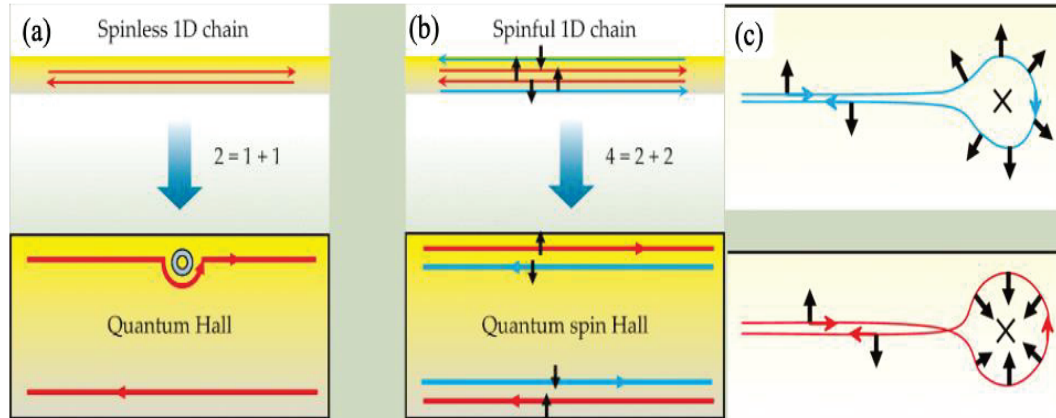


Figure 1.3 Quantum Spin Hall effect (a) Depicts a one-dimensional spinless electron transport chain, which has two degrees of freedom: forward (at the upper edge) and backward (at the lower edge) mover, these two degrees of freedom can be represented by symbolic equation $2=1+1$ and separated in QH state. Because of the one-way motion, states are robust, and backscattering is prohibited. (b) depicts a one-dimensional spinful electron transport chain, with two forward and two backward movers separated in the QH states. Upper edge states have two movers (one forward with up spin and the other backward with down spin) and conversely for lower edge. (c) The scattering of electrons by a nonmagnetic impurity in QSH states adopted two possible paths: clockwise (upper) and counter-clockwise (lower) rotation around the impurity, figure adopted from ref. [7].

As long as TRS is preserved, backscattering is not permitted in the QSH system. However, suppose a non-magnetic impurity scatters off a right mover with having a spin-up. In that case, it can go around the impurity either clockwise or counter-clockwise (see Fig. 1.3 c) and, in order to move left, it must flip its spin down; hence its spin must rotate at an angle either of π or $-\pi$.

Consequently, the phase difference between two moving paths of spin (which are protected by TRS) is a full 2π $\{\pi - (-\pi) = 2\pi\}$ rotation of electron spin. Under a full 2π rotation, the wave function of a spin-1/2 particle takes on a minus sign, *i.e.*, $\psi(\theta) = -\psi(\theta + 2\pi)$ [1,7,25]. As a result, the two TRS-connected backscattering paths always interfere destructively, results a perfect transmission, and the quantum mechanical probability of backscattering is significantly reduced.

In other words, in the presence of the nonmagnetic impurity, there is no dissipation due to the suppression of backscattering. However, magnetic impurity breaks the TRS in the system, and two paths will no longer interfere destructively, will lead to dissipation.

1.4 The 3D Topological Insulators

Since the discovery of TIs, 3D TIs have gained immense attention and are the most studied topological insulator family till now. To characterize the QSH state in 3D, three theoretical groups discovered the topological characterization of the QSH state in 2006, which was later coined as a 3D TIs [26]. Soon after, Fu and Kane [8] predicted the first-generation 3D TIs phase in actual material such as $\text{Bi}_{1-x}\text{Sb}_x$ ($x = 0.09\sim 0.23$) binary alloy, and suggested that the non-trivial topology of this material can be verified by the study of surface state crossing at the E_F between two time-reversal invariant momenta (TRIM) points using ARPES. This binary alloy possesses two main features: band inversion occurs at an odd number of TRIM points, and the bulk is insulating for some specific composition range. After the theoretical prediction, one year later, Hsieh *et al.* [27] experimentally verified $\text{Bi}_{1-x}\text{Sb}_x$ binary alloy as indeed a 3D TI. This experimental finding was the beginning of the 3D TIs era. One can see band dispersion $\text{Bi}_{1-x}\text{Sb}_x$ ($x=0.13$) alloy in Fig. 1.4; there are three points where surface states cross the E_F [14,28]. This odd number time crossing is the fingerprint signature of the Z_2 -nontrivial nature. However, many times E_F crossing makes surface structure complicated, and it came to know that the chemical composition in the $\text{Bi}_{1-x}\text{Sb}_x$ binary alloy is not stable, along with complex surface structure and narrow bandgap (up to 30 meV, depending on the x). These properties make it unsuitable for future applications. Apart from this Bi and Sb-based alloy, Fu and Kane [8] also predicted some other materials, such as HdTe , α - Sn , and $\text{Pb}_{1-x}\text{Sb}_x\text{Te}$, which could become 3D TIs by breaking the cubic lattice symmetry under the uniaxial stress. After the discovery of first-generation 3D TIs, almost two years later, Zhang *et al.* [9] gave a theoretical prediction of the second-generation of 3D TIs and suggested that Bi_2Se_3 , Bi_2Te_3 , and Sb_2Te_3 could be the 3D TI, but Sb_2Se_3 could not. Soon after the theoretical prediction, Xia *et al.* experimentally verified Bi_2Se_3 in 2009 [29], which shows a single DP at the $\bar{\Gamma}$ point in the surface BZ. Simultaneously Bi_2Te_3 also came in

experimental existence by Chen *et al.* [12] and Hsieh *et al.* [30]. The Sb_2Te_3 was also measured by Hsieh *et al.* [30], however, it was not confirmed as a 3D TI by the ARPES experiment because the measured sample was highly p-type doped. Later Scanning tunneling spectroscopy (STS) experiment confirmed the topological nature in the thin film-grown Sb_2Te_3 samples. Similar to 2D TIs version, band inversion in 3D TIs occurs at the TRIM (Γ point) due to the presence of strong SOC, and bulk is fully insulating (gapped) along with topologically protected metallic surface states forming a single massless Dirac cone in the insulating gap. One can see in the schematic diagram in Fig. 1.5 (c) and (d), the momentum and electron spin of the Topological surface states (TSSs) are locked due to the SOC, yielding a peculiar helical spin texture in the momentum space [1,11]. As long as TRS is preserved, the helical spin texture of the TSSs prevents electron backscattering due to lattice defects or nonmagnetic impurities [31,32], and enhances the quasiparticle lifetime, electrical conductivity, and mobility. However, one can introduce surface magnetic ordering by the magnetic element doping or deposition on the surface of 3D TIs and can break TRS, which make the system fully insulating or trivial TIs. The metallic nature of the TSSs is robust against the perturbations that conserve the topological numbers, which is characterized by symmetry properties of the energy bands under the strong SOC [1,2].

These second-generation 3D TIs have attracted much interest not only for their potential spintronic applications [33] but also for their intriguing physical properties, such as the quantum spin Hall effect (QSHE) [6], quantum anomalous Hall effect [34], Majorana fermions in the superconducting state [35,36], and magnetic monopole [37].

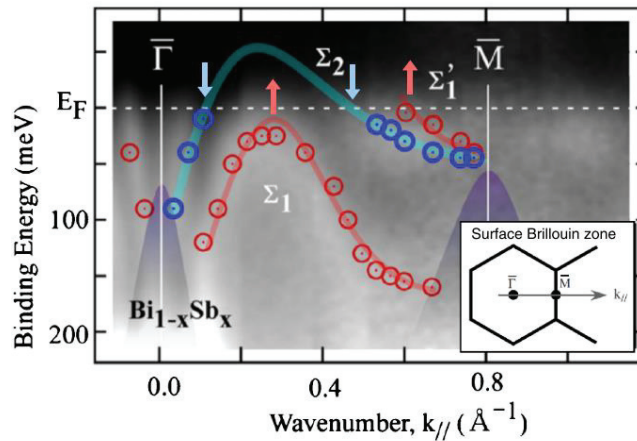


Figure 1.4: Spin polarised band dispersion of Binary $\text{Bi}_{1-x}\text{Sb}_x$, where x is 0.12 to 0.13 on the (111) cleaved surface. Inset shows surface BZ, which represents high symmetry direction. Open circles are used to plot the spin-resolved data, which is then placed on a spin-integrated grayscale diagram. Thin (thick) lines schematically trace the dispersion curves of spin-up (spin-down) bands, and their spin-up (spin-down) bands are plotted with thin red (thick blue) circles. The dark purple area is the bulk band projection based on ARPES data. At the E_F of $\text{Bi}_{1-x}\text{Sb}_x$ ($x=0.13$), the inset shows a two-dimensional wave-number-resolved photoemission intensity pattern. The $\bar{\Gamma} - \bar{M}$ is represented by the dashed line. This figure is taken from ref.[14].

In contrast to 2D Z_2 -type TIs, second-generation 3D TIs have many attractive advantages in pursuing this field. 1) The TSS is not buried in the bulk (see Fig. 1.5 (a) and (b)) and is stable at room temperature (RT) until no magnetic field is present. 2) It is easy to study the transport properties of TSS. 3) One can easily dope magnetic elements in 3D TIs and realize the various physical properties such as magnetism, Quantum anomalous Hall effect, and superconductivity. Since the discovery of the 3D TIs, more than a hundred 3D Z_2 TIs have been identified. These conditions make 3D Z_2 TIs very promising for spintronic applications. Therefore, this thesis will explain more about the second-generation 3D TIs such as Bi_2Se_3 , Bi_2Te_3 , and Sb_2Te_3 .

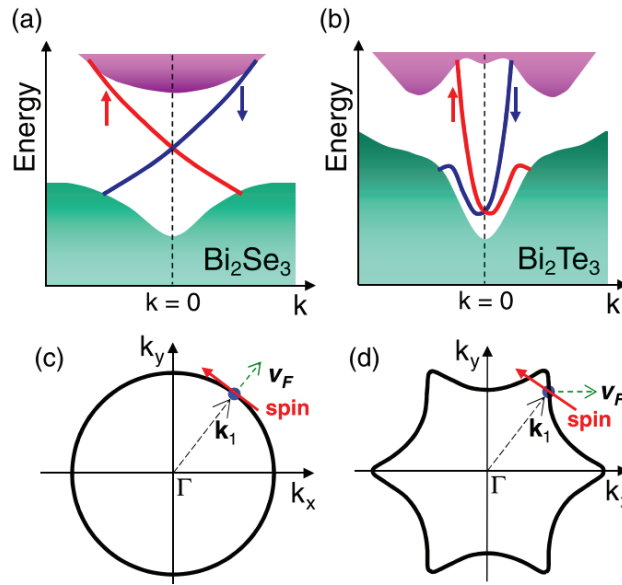


Figure 1.5: The Schematic band dispersion of Bi_2Se_3 and Bi_2Te_3 , depicts in (a) and (b), respectively, where Dirac cone-like surface states are in between the bulk bandgap. (c) and (d) Schematic representation of constant energy contours at E_F for Bi_2Se_3 and Bi_2Te_3 , respectively. Here electron spin is always perpendicular to the wave vector, representing spin-momentum locking. However, Fermi velocity (v_F) is orthogonal to the spin vector for Bi_2Se_3 (figure. c), but to the hexagonal wrapping effect, Fermi velocity (v_F) is not orthogonal to the spin vector for Bi_2Te_3 (figure. d). This figure is taken from ref [14].

All three 3d TIs; Bi_2Se_3 , Bi_2Te_3 , and Sb_2Te_3 , have the same rhombohedral structure with $R\bar{3}m (D_{3d}^5)$ space group [1]. Fig. 1.6 shows the Bi_2Te_3 crystal structure. It possesses a layered structure having three quintuple layers (QLs) stacked along the z-axis. The dashed lines represent one quintuple layer, which is composed of two equivalent Te(1), two equivalent Bi and one Te(2) atomic layers stacking (1 atom per atomic slice). Atomic layers are covalently bonded, while QLs are connected by weak van der Waals (vdW) bonding. Therefore it is easy to cleave mechanically at the adjacent two QLs. As one unit cell has three quintuple layers, each quintuple layer contains five atoms along with about 1 nm stacking thickness along the z-direction. This quintuple layer serves as a building block in the crystal structure. Therefore, one unit cell contains 15 atoms (3 QLs) along with about 3 nm thickness along the z-direction.

Fig. 1.6(b) represents the top view of the crystal structure along the z-direction, showing a triangular lattice arrangement in one QL, which has three A,

B, and C equivalent positions. Figs. 1.6 (c) and (d) represent primitive unit cell (rhombohedral) and conventional unit cell (hexagonal) of Bi_2Te_3 , respectively.

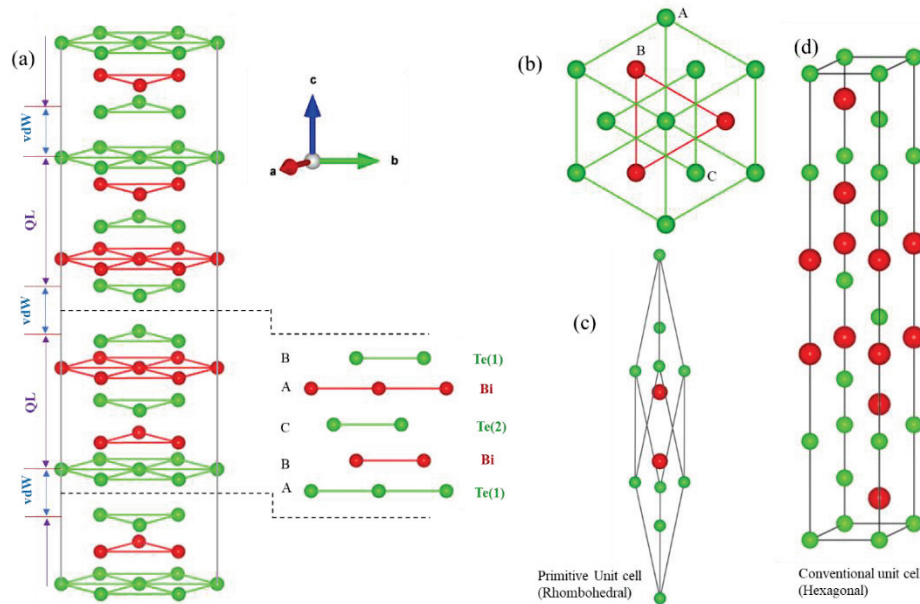


Figure 1.6: Crystal structure of Bi_2Te_3 . (a) crystallographic unit cell, which possesses three quintuple layers (b) depicts in-plane triangular lattice arrangement in one quintuple layer, with three positions A, B, and C. (c) primitive rhombohedral unit cell. (d) The conventional unit cell of Bi_2Te_3 .

Although the second-generation 3D TIs are predicted as completely insulating in bulk along with metallic states at the surface, but in reality, it was found that surface states are consistently hampered by bulk carrier concentration due to intrinsic defects in the crystals. Therefore, controlling the E_F position in these materials is the central issue.

Pure Bi_2Se_3 crystals are generally n-type semiconductors due to inevitable Selenium (Se) vacancies, which act as electron donors. Formation of Se vacancies and anti-site defects occur during the crystal growth; however, Se vacancy defects are dominant over anti-site defects due to significantly less formation energy of Se vacancy. When the Se atom escapes as a vapor, it leaves two electrons left behind in the system, which makes Bi_2Se_3 highly electron-doped. One can understand Se vacancy defects using the Kroeger-Vink notation reaction: $Se_{Se} \rightarrow V_{Se}^{\circ\circ} + Se(g) + 2e'$, showing Se escape as a vapor, which originates doubly positive charged vacancy and releases two electrons in the system. We can minimize the Se vacancy

defects by varying the initial stoichiometry (grown crystals in a Se-rich environment) [38].

In contrast to Bi₂Se₃, the Bi₂Te₃ crystals are generally reported as *p*-type semiconductors due to dominant anti-site defects over Tellurium (Te) vacancy defects. The reaction to anti-site defects is $Bi_{Bi} \rightarrow Bi'_{Te} + Te(g) + h^{\circ}$, showing holes left behind during the formation of this defect. However, Bi-rich grown Bi₂Te₃ crystals quickly invert the carrier concentration, and the system can be an *n*-type semiconductor. Nevertheless, growing crystals suppressing bulk carrier concentration is still challenging. On the other hand, Sb₂Te₃ is always reported *p*-type semiconductor because anti-site defects in Sb₂Te₃ are even 10 times higher than Bi₂Te₃ [39].

First-principle calculations have been done by Zhang *et al.* to understand the second-generation 3D TIs[9]. They picked up a simple model system Bi₂Se₃ and began with the simple atomic energy levels, and then considered spitting of the energy eigenvalues at the TRIM point ($\bar{\Gamma}$) due to crystal field spitting effect and SOC. These splitting are summarized schematically in different stages, as shown in Fig. 1.7(a). Because *p* orbitals are responsible for the states majority close to the Fermi surface, they ignore the effect of *s* orbitals and begin with the atomic *p* orbitals of Bi ($6s^26p^3$) and Se ($4s^24p^4$). Stage (I) shows the effect of chemical bonding within atoms in a QL, representing this problem's most enormous energy scale. According to the parity effect, Bi and Se *p*-orbitals split into three and two energy states, respectively, and these energy states further shifted their positions due to hybridization. The next stage (II) represents the effect of crystal field spitting on *p* -orbitals near E_F, where *p_z* Orbital further splitted due to point group symmetry. In the final stage (III), the effect of SOC is considered to combine the spin and angular momenta in the system. If the strength of SOC is large enough, band inversion occurs between the states near E_F, as shown in Fig. 1.7(a). Due to band inversion at the $\bar{\Gamma}$ point, Bi₂Se₃ belongs to a non-trivial insulating phase family. Similar band structure analysis suggests that Bi₂Te₃ and Sb₂Te₃ also belong to the non-trivial insulating phase family, whereas Sb₂Se₃ is not.

Fig. 1.7(b) depicts the 3D BZ of Bi_2Se_3 , where the surface Brillouin zone (SBZ) is projected on top. The TRIM points in the 3D BZ are marked as $\Gamma(0,0,0)$, $L(\pi, 0,0)$, $F(\pi, \pi, 0)$, and $Z(\pi, \pi, \pi)$. The Γ and Z points in 3D BZ are projected to the $\bar{\Gamma}$ point on the SBZ. On the other hand, the L and F points are projected to the \bar{M} point on the SBZ. According to Fu and Kane's [8] proposed model, one can distinguish nontrivial topological nature using parities of the Bloch wavefunctions at the TRIM points in the 3D BZ. Fig. 1.7(c) represents the product of parities at the TRIM point Γ in the 3D BZ, showing odd parity at Γ , which suggests that if SOC is turned on, then at least the parity of one band is reversed in all three compound Bi_2Se_3 , Bi_2Te_3 , and Sb_2Te_3 . On the other hand, the product of parities is even at other TRIM points (L , F , and Z) in the BZ. This study suggests that Bi_2Se_3 , Bi_2Te_3 , and Sb_2Te_3 belong to the non-trivial topological phase. However, in the case of Sb_2Se_3 , the product of parities is even for all four TRIM points, which suggests that SOC is insufficient to invert the bands in Sb_2Se_3 . Therefore, Sb_2Se_3 does not belong to the non-trivial 3D TIs family.

Early ARPES measurement confirmed the surface electronic structure of these second-generation 3D TIs. Fig. 1.8 (a) and (b) depicts band dispersion of Bi_2Se_3 along $\bar{\Gamma} - \bar{M}$ and $\bar{\Gamma} - \bar{K}$ high symmetry directions, respectively. Unlike multiple surface-state found in the $\text{Bi}_{1-x}\text{Sb}_x$, the surface structure of Bi_2Se_3 is relatively simple, showing Dirac-fermion-like linear dispersion forming a single Dirac cone around the $\bar{\Gamma}$ point. Fig. 1.8(e) represent band dispersion of Bi_2Te_3 along $\bar{\Gamma} - \bar{M}$ (lower panel) and $\bar{\Gamma} - \bar{K}$ (upper panel) high symmetry directions, showing similar Dirac-fermion-like linear dispersion with a single Dirac cone at $\bar{\Gamma}$ point. In these ARPES intensity maps, one can see the E_F is located within the CB due to intrinsic defects or vacancy (as discussed above), showing an n -type (electrons majority) semiconductor nature.

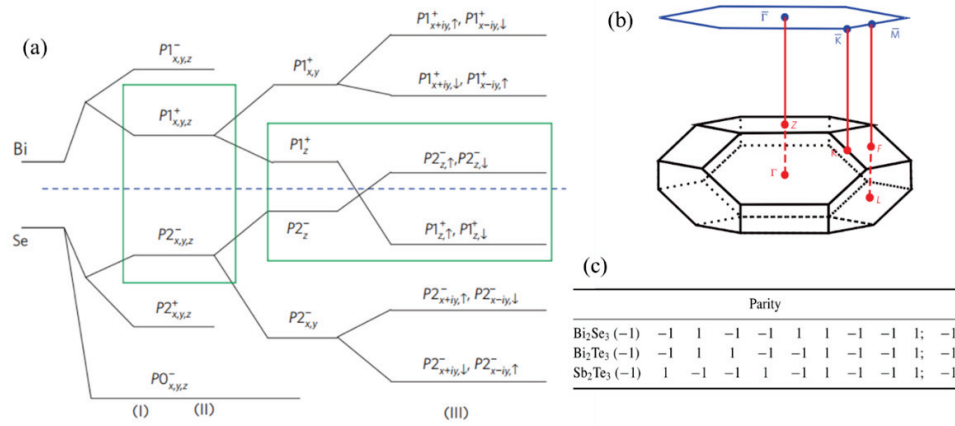


Figure 1.7: First principle calculation of TIs (a) Schematic band picture of Bi₂Se₃ at Γ point. Here stage (I) shows spitting due to the effect of chemical bonding. On the other hand, stages (II) and (III) represent spitting because of the crystal field and SOC. The dashed line represents the position of E_F. (b) BZ of Bi₂Se₃, where SBZ are projected on the top. (c) Product of parity at Γ point for the non-trivial topological family. Figures are taken from ref. [9].

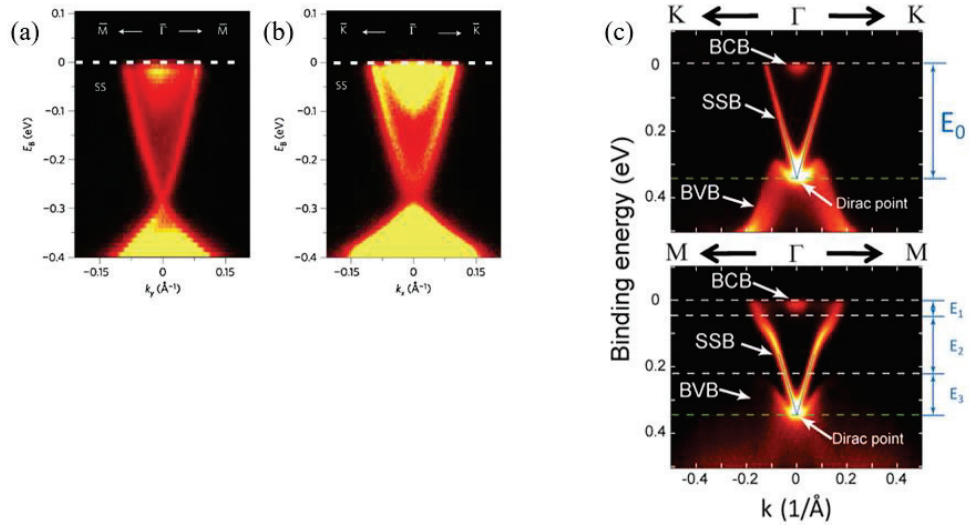


Figure 1.8: ARPES intensity image of Bi₂Se₃ along $\bar{\Gamma} - \bar{M}$ and $\bar{\Gamma} - \bar{K}$ high symmetry directions depict in (a) and (b), respectively. The figure is taken from ref. [29]. (c) depicts ARPES intensity image of Bi₂Te₃ along $\bar{\Gamma} - \bar{M}$ (lower panel) and $\bar{\Gamma} - \bar{K}$ (upper panel) high symmetry directions. The figure is taken from ref. [12].

1.5 Theoretical Formulation of Topological Insulators

1.5.1 Spin-Orbit Coupling

The spin-orbit coupling (SOC) [40] is the interaction between the spin and orbital electron motion, a quantum mechanical relativistic phenomenon. The SOC plays an essential role in condensed matter physics, leading to QSHE, QAHE, and 3DTIs. We can understand the SOC, a charged particle having spin s moving in a static magnetic field with velocity \mathbf{v} . Through Lorentz translation, the traveling electric field is interpreted as a magnetic field B in the particle's reference frame and can be written as

$$B = -\frac{1}{c} \mathbf{v} \times E = \frac{1}{mc} (E \times P), \quad (1.7)$$

Where P is electron momentum, and c is the speed of light. In the case of an electron, it has a magnetic moment (μ_s) that is related to its spin. This magnetic moment (μ_s) feels a force due to an effective magnetic field which is described by a Hamiltonian $H_B = -\mu_s \cdot B$.

The spin-orbit coupling Hamiltonian can be calculated directly from the relativistic Dirac equation with $E = -\nabla V$ is taken into consideration,

$$H_{SOC} = \frac{\hbar}{4m^2c^2} \vec{\sigma} \cdot (\nabla V \times \vec{p}), \quad (1.8)$$

where $\vec{\sigma} = (\sigma_x, \sigma_y, \sigma_z)$ is the Pauli spin metrics, \vec{p} is the momentum operator, and V is the coulomb potential of the atomic core. The gradient ∇V is proportional to the fourth power of atomic number Z , *i.e.*, Z^4 . The heavier elements have stronger SOC.

1.5.2 TRIM Points

Time reversal invariant momenta (TRIM) points are the specific point in the BZ, where two states spin degenerate at ($k = -k$), and the degeneracy is lifted away from the TRIM points. When the system is symmetric under time reversal operation (\mathcal{T}), all first-order parameters, such as velocity and momenta, are reversed under this operation. The following conclusion is enforced in practice by time-reversal symmetry:

$$\mathcal{T} \{E(|k, \uparrow)\} = E(|-k, \downarrow) \quad (1.9)$$

It means that the energy states of the time reversal symmetric system come into pairs at opposite momentum points (k and $-k$), having opposite spin directions. These energy pairs are called Kramers pairs. However, there are some specific points in the BZ, for example, $k = k + G$ (G is the reciprocal lattice vector) where inversion symmetry holds ($k = -k$). That is, if the inversion symmetry (I) holds, the following relation also holds:

$$I \{E(|k, \uparrow)\} = E(|-k, \uparrow). \quad (1.10)$$

If both symmetries (time-reversal symmetry and inversion symmetry) hold simultaneously, then one obtains the following relation:

$$I[\mathcal{T} \{E(|k, \uparrow)\}] = I[E(|-k, \downarrow)] = E(|k, \downarrow) \quad (1.11)$$

$$E(|k, \uparrow) = E(|k, \downarrow) \quad (1.12)$$

It means that the energy states are spin degenerate at these momenta. Those points where spin degeneracy occurs, are called TRIM points, and this degeneracy is lifted away from the TRIM points. One can see in Fig. 1.9, 0 and π (π and $-\pi$ are equivalent points in the Brillouin zone) are the TRIM point, where energy states are spin degenerate due to periodicity in the BZ, and this degeneracy lifted away from the TRI point 0 and π . However, degeneracy at TRIMs is lifted if TRS is broken due to magnetic element doping or applying an external magnetic field.

1.5.3 Definition of Topological Invariant or Z_2 Invariant

The topological nature of insulators is characterized by a Z_2 invariant, named as ν . This topological invariant ν can be calculated by the product of parity eigenvalues of the occupied bands at the TRIM points. At each TRIM point (Λ_i), the product of the parity of all occupied bands can be evaluated as [26];

$$\delta_i(\Lambda_i) = \prod_s \xi_{2s}(\Lambda_i) \quad (1.13)$$

where ξ is the parity eigen value, and $\xi_{2s}(\Lambda_i)$ parity of block wave function at the TRIM points (Λ_i). The Z_2 topological invariant ν is then calculated from the product of the parities of occupied bands at all TRIM points in the Brillouin zone as:

$$(-1)^{\nu} = \prod_{i=1}^{\Lambda_i} \delta_i \tag{1.14}$$

The parity's eigen value assumes two values: +1 (even parity) or -1 (odd parity). So, on the right-hand side of equation (1.14), the product of the parity at TRIM points could be either +1 or -1. Therefore, depending on the topological invariant ν , the parity may take either +1 = $(-1)^{\nu}$ (ν is odd) or -1 = $(-1)^{\nu}$ (ν is even), which is the reason that the parity is mathematically equivalent to \mathbb{Z}_2 . If the topological invariant is $\nu = 1$, then the insulator belongs to the non-trivial topological family called TIs, which indicates an odd number of time parity inversions occur between TRIM points. In the case of $\nu = 0$, the insulator belongs to the normal insulator family called a trivial insulator.

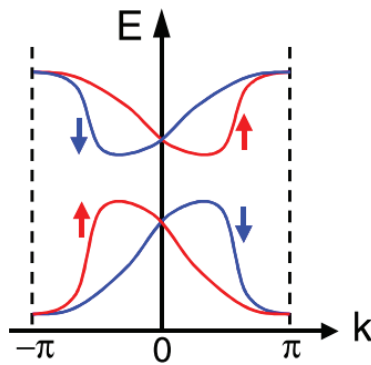


Figure 1.9: Depicts the energy states of Kramer pairs. Each Kramer pair states are degenerate at the TRIM points ($k = -k$, *i.e.* $k = 0$ and π) due to the periodicity of the Brillouin zone, and this degeneracy is lifted away from the TRIM points, a figure taken from ref. [14]

Chapter 2: Experimental Background

This chapter will explain the details of the experimental procedure used in this thesis. First, we will describe single crystal growth, characterization by X-ray diffraction (XRD), and some basics of ARPES. After that, we will explain our laser-based high-resolution angle-resolved photoemission spectroscopy (μ -ARPES) and the sample preparation for ARPES measurement.

2.1 Single Crystal Growth

2.1.1 Bridgeman Method

The Bridgeman method is the most widely used method for growing single crystals [13]. This method is ideal for congruently melting compounds and materials that do not go through phase transitions between melting points. A schematic diagram of our setup is shown in Fig: 2.1. In this technique, polycrystalline samples are kept in a container with a sharp conical bottom made of such as quartz or alumina tubes and heated above the melting point for homogeneous melt. Using the furnace controller, the tube is slowly cooled down with a constant temperature gradient. When the temperature reaches below the melting temperature of the material, crystal growth is initiated at the bottom of the conical tube, and the entire melt liquid converts into the solid-crystalline ingot. A long duration of annealing below the melting temperature help to find a bigger size crystal. However, it is optional depending on the requirement of the sample size. In general, the temperature gradient is provided by the translation motion of the tube in two-zone furnaces (Hot to cold zone). However, one can provide a temperature gradient using a precise temperature controller without translation motion; this is what indeed we used in our crystal growth.

High-quality Bi_2Te_3 single crystals were grown using a Bridgeman method (direct melt reaction) in a vertical tubular furnace. High purity (5N) Bi and Se with a molar ratio of 3:2 were mounted in a quartz ampule and sealed with a 10^{-6} Torr vacuum inside. The ampule was hung in a vertical tube furnace and heated above the melting temperature of Bi_2Te_3 from RT to 950 °C within 12 h (see Fig. 2.1). During melting, the ampule was rotated continuously at 5 rpm using an external ac

motor for better homogeneity. After a temperature 950 °C was maintained for 24 h, the ampule was cooled slowly to 550 °C at a rate of 2 °C per hour and then annealed at this temperature for 72 h, followed by the furnace cooling to RT. The crystals for measurements were removed from the cm-sized silver Bi₂Te₃ ingot by cutting perpendicular to the growth direction along the *c*-axis (00*l*). A typical growth profile can be found in Fig. 2.2.

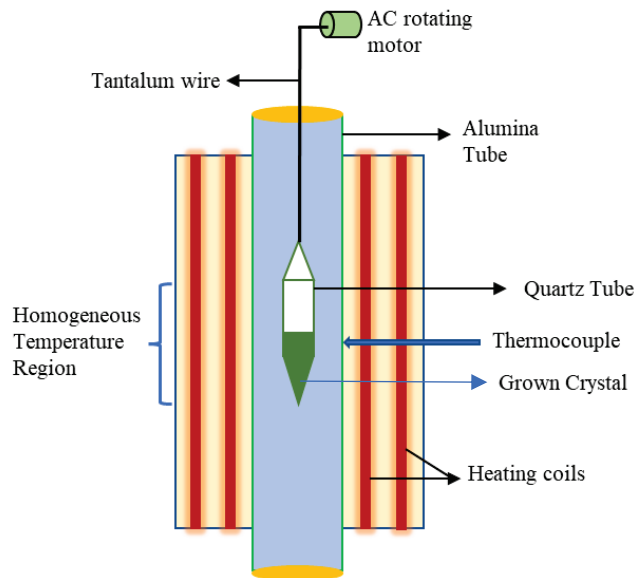


Figure 2.1: The schematic picture of our Vertical furnace.

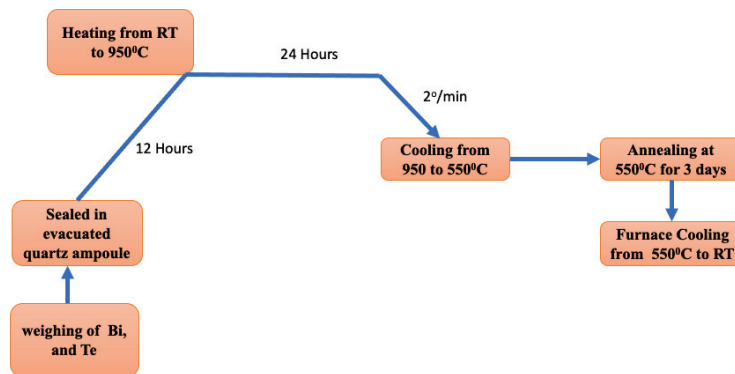


Figure 2.2 A typical single-crystal Growth profile of Bi₂Te₃.

2.1.2 X-ray Diffraction

Bragg's Law

Electromagnetic radiation interacts with matter and gives information about its constituents. Solid crystals have a periodic arrangement of their constituent atoms. On shining the x-ray over the crystal, the x-ray is diffracted by the periodic atoms following Bragg's law. The schematic diagram of Bragg's law is depicted in Fig. 2.3(a).

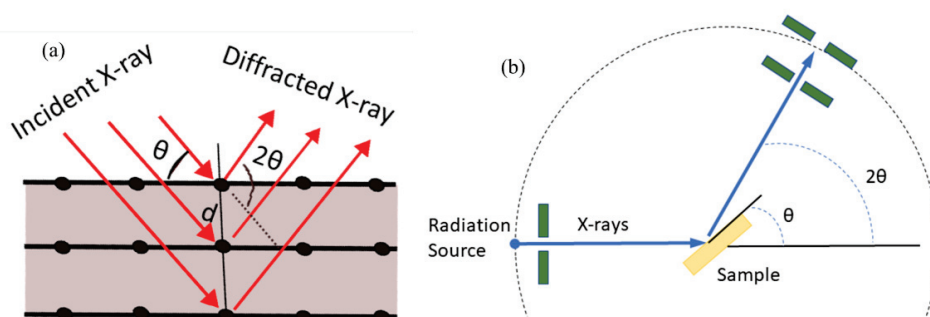


Figure 2.3: The schematic of (a) Bragg's law and (b) X-ray measurement geometry.

The crystal structure consists of d_{hkl} interplanar distance (hkl is Miller indices) and the angle between the incident and the diffracted wave is θ , and the wavelength of the incident X-ray is λ . Bragg's law for diffraction will be $2d_{hkl}\sin\theta = n\lambda$. Diffraction will occur when $\lambda \leq 2d$. Fig. 2.3(a) shows the schematics of diffracted x-ray waves from the lattice planes. The X-ray shines the sample at an angle θ and gets diffracted at 2θ , which is recorded by a detector. A diffractogram is recorded over a complete range of 2θ , and each intense peak is characteristic of the crystal structure. Using Bragg's law Miller indices are confirmed, and then crystal structure is confirmed.

After crystal growth, the preliminary single-crystal phase confirmation and powder X-ray analysis were performed using a Rigaku Ultima IV X-ray diffractometer with $Cu K_{\alpha}$ radiation ($\lambda=1.54 \text{ \AA}$). Fig. 2.4 represents the single-crystal X-ray diffraction (XRD) intensity diagram of Bi_2Te_3 measured at RT. The XRD intensity diagram indicates that the as-grown single crystalline sample is of high quality, which is consistent with previous reports [41,42]. Peak indexing was

performed by using a standard JCPDS file (JCPDS#15-0863) [43]. Moreover, we further confirmed a single-phase using powder XRD of Bi_2Te_3 .

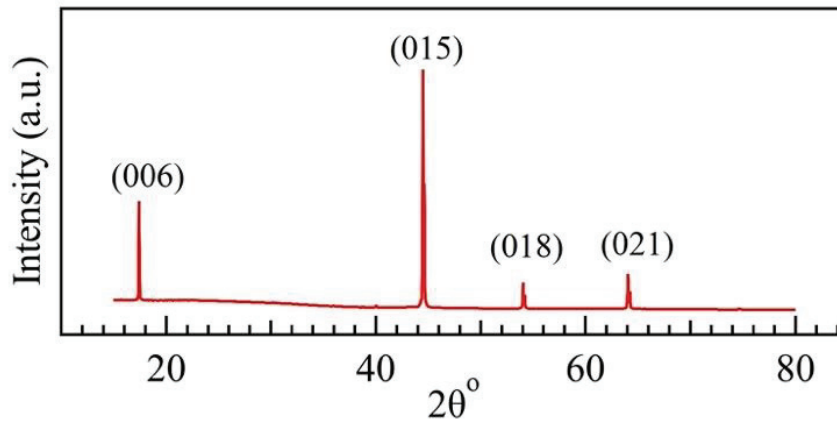


Figure 2.4: Single-crystal X-ray diffraction intensity diagram of Bi_2Te_3 measured at RT.

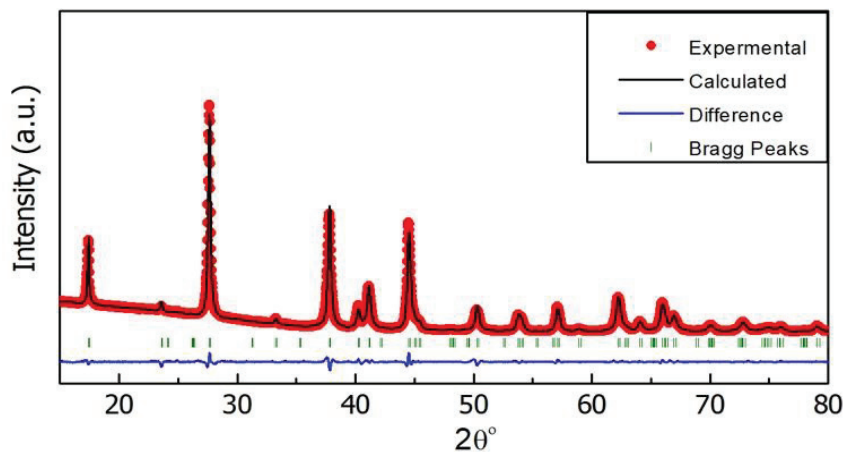


Figure 2.5: Refined powder X-ray diffraction data of Bi_2Te_3 : Observed (red circles), calculated (continuous black line), and difference (bottom blue line) profiles obtained after Le-Bail refinement using the $R\bar{3}m$ space group. The vertical bars represent the Bragg peak positions (green).

Fig. 2.5 shows Le-Bail refinement of the powder XRD data using space group $R\bar{3}m$ (166) achieved by utilizing the Fullprof suite software package. All the peak positions coincide well with the peaks corresponding to the space group (shown by vertical green bars in Fig. 2.5), and the calculated lattice parameters are found to be $a = b = 4.384694 \text{ \AA}$ and $c = 30.499649 \text{ \AA}$ from the refinement, which consistent with previously reported lattice parameters [42].

2.2 Angle-Resolved Photoemission Spectroscopy (ARPES)

The ARPES is one of the most straightforward approaches for investigating the electronic structure of solid surfaces [2,7,44-48], where the distribution of electronic states in the reciprocal space has been analyzed. The basic principle of this technique is based on the photoelectric effect, which was first noticed by Hertz in 1887 [49] and microscopically explained later by Einstein in 1905 [50]. When monochromatized energy photons are incident on the sample surface, electrons absorb the photon's energy and escape into the vacuum with different kinetic energies. These escaped electrons are called photoelectrons, and photoemission spectroscopy (PES) evaluates photoelectrons. In ARPES, kinetic energy along with the angle of escaped electrons are analyzed, and these emitted electrons are collected at a finite acceptance angle by the analyzer, that measures the kinetic energy of each electron at the emission angle by which momentum (\vec{p}) of photoelectron can be determined by using relation,

$$|\vec{p}| = \sqrt{2mE_{kin}} \quad (2.1)$$

where the parallel and perpendicular components of photoelectron momentum (\vec{p}) from the sample surface can be described using polar (θ) and azimuth (ϕ) angles.

A schematic diagram of ARPES geometry is shown in Fig. 2.6(a). When a light energy ($h\nu$) incident on the sample surface, photons are absorbed by the electrons in the material. If the absorbed energy is larger than the work function of a material, then electrons can escape into the vacuum and be detected by the electron analyzer. The number of photoelectrons with a specific kinetic energy (E_{kin}) is counted as a function of polar (θ) and azimuth (ϕ) angles, which are directly related to the energy and momentum of the electron inside the materials.

In the non-interaction picture, considering energy and momentum are conserved in the photoelectric process (Here, photon momentum is neglected because of the low photon energy used), One can calculate the binding energy of the electron in the material using the following relation below [45,51],

$$E_{kin} = h\nu - \Phi - |E_B| \quad (2.2)$$

Here, Φ is the work function of the sample, which is the minimum energy from the E_F to escape the electron to the vacuum level, as shown in Fig. 2.6(c).

The component of electron momentum in all three directions (x , y , and z) can be written as,

$$k_x = \frac{\sqrt{2mE_{kin}}}{\hbar} \sin\theta \cos\phi \quad (2.3)$$

$$k_y = \frac{\sqrt{2mE_{kin}}}{\hbar} \sin\theta \sin\phi \quad (2.4)$$

$$k_z = \frac{\sqrt{2mE_{kin}}}{\hbar} \cos\theta \quad (2.5)$$

Using polar (θ) and azimuth (ϕ) angles. Higher-order BZ can be accessible in the extended-zone scheme using high photon energy or larger polar angles.

2.2.1 Basic Models for ARPES

There are two models that give a basic description of the PES [51].

- (1) One-step model
- (2) Three-step model

The three-step model is simple and most widely used in photoemission, which simplifies the photoemission process into three independent steps, as described in Fig. 2.7. In the sudden approximation, considering a noninteracting electron picture, three step-model is described in the following step:

- (i) An electron is excited from its initial state (E_i) to the final state (E_f) inside the bulk.
- (ii) The excited electron travels through the bulk to the surface.
- (iii) The electron overcomes the surface work function and escapes into the vacuum.

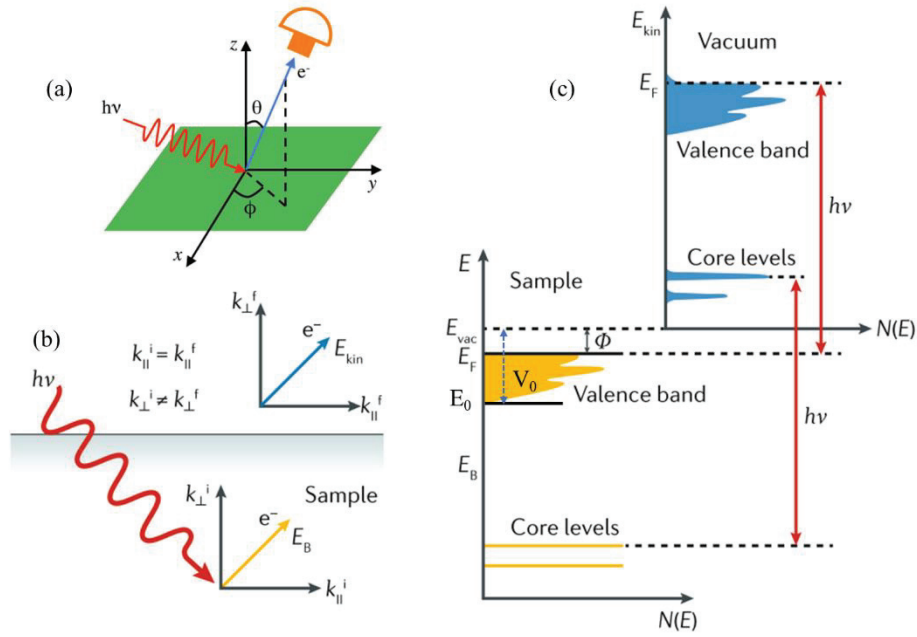


Figure 2.6: The schematic of ARPES (a) A basic geometry of ARPES setup, where $h\nu$ in the incident photon energy on the sample, by which electrons are ejected at angles (θ, ϕ) from the sample surface and finally collected by the analyzer. (b) representing the momentum conservation in the photoemission process. (c) depicted energies adopted during the photoemission process, figure adopted from the ref. [47].

On the other hand, the one-step model is expected to explain photoemission intensity distribution more realistically, though the calculation is much more complicated.

During the excitation process, where the photoelectron (e^-) is emitted from the crystal into the vacuum through the surface, the wave vector ($k_{||}$) parallel to the surface is conserved in this process if there is no electric field parallel to the sample surface. Therefore, the inside wave vector ($k_{||}$) and outside wave vector ($K_{||}$) should be equal, as depicted in Fig. 2.6(b), and can be written as (in extended zone scheme)

$$K_{||} = k_{||} = \frac{\sqrt{2mE_{kin}}}{\hbar} \sin\theta. \quad (2.6)$$

On the other hand, the wave vector perpendicular to the surface (k_{\perp}) is not conserved (i.e. $k_{\perp} \neq K_{\perp}$), because electric potential inside solid and vacuum is different, leading to a non-zero potential gradient (electric field) perpendicular to the sample surface. However, for low dimension systems, such as an ideal 2D

electron system, electron motion is confined within the 2D plane and the dispersion along the k_{\perp} direction (perpendicular to the 2D plane) can be neglected. In this case, it is not necessary to determine k_{\perp} .

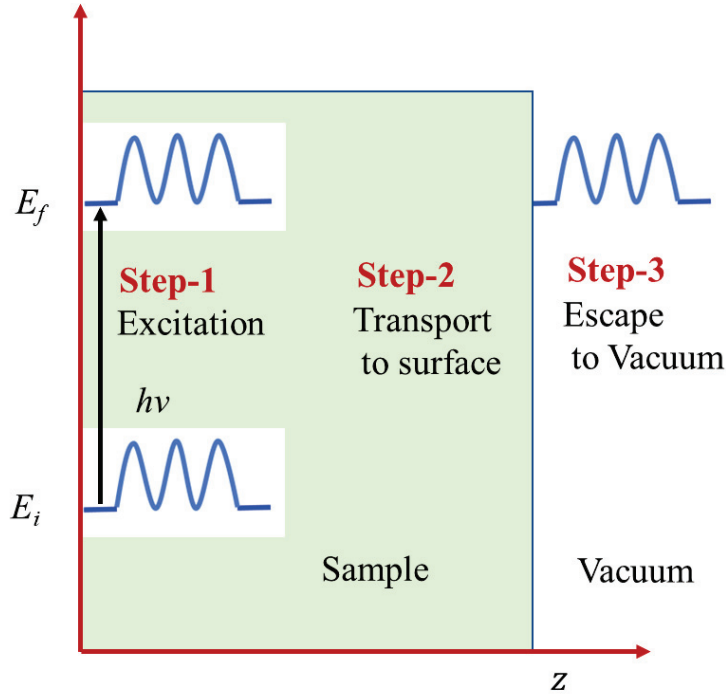


Figure 2.7: The schematic pictorial representation of the three-step model.

On the other hand, in the case of 3D systems band dispersion, k_{\perp} can be evaluated using some assumptions as described below. One should note that excitation is finished in the first step of the three-step model, where only direct (or vertical) transitions are considered. In this step, electron excitation is nearly free electron-like excitation in the solid. However, a final state excited electron is not represented by a simple plane wave-like state but by a Bloch state. Assuming a nearly free electron like picture, the final Bloch state energy can be written as

$$E_f(k) = \frac{\hbar^2 k^2}{2m} - |E_0| = \frac{\hbar^2 (k_{\parallel}^2 + k_{\perp}^2)}{2m} - |E_0| \quad (2.7)$$

$$E_f(k) = E_i(k) + h\nu \quad (2.8)$$

$$E_f(k) = E_k + \Phi \quad (2.9)$$

Here E_0 is the binding energy of the VB bottom with respect to E_F as depicted in Fig. 2.6(c). Using equations (2.6), (2.7), and (2.9), one can calculate the perpendicular component of the wave vector k_{\perp} , and written as:

$$k_{\perp} = \frac{1}{\hbar} \sqrt{2m(E_{kin} \cos^2 \theta + V_0)} \quad (2.10)$$

where V_0 is called inner potential, which is equal to the sum of E_0 and the work function Φ . This inner potential V_0 can be either evaluated by theoretical calculations or experiments. Typical value of V_0 is around 10 eV. One can evaluate V_0 by running the photon energy-dependent ARPES measurements, where the periodic variation of 3D band structures is examined.

2.2.2 Evolution of Spectral Function

Under the three-step model and sudden approximation, photoemission intensity (I) measured in the APRES measurement can be written as [44],

$$I \propto |\langle \psi_f^N | H_{int} | \psi_i^N \rangle|^2 \delta(E_f - E_i - \hbar\omega) f(E, T) \quad (2.11)$$

where the first term $|\langle \psi_f^N | H_{int} | \psi_i^N \rangle|^2$ is the matrix element which represents the transition between an initial state ψ_i^N and final state ψ_f^N due to photon field $H_{int} = \vec{A} \cdot \vec{P}$. The subscript i and f represent the initial and final states, respectively, and superscript N is the total number of electrons, \vec{A} and \vec{P} represent the electromagnetic vector potential and electronic momentum operator, respectively. The matrix element does not directly represent the band dispersion. However, if particular measurement geometries are used, the matrix element can yield valuable orbital information on electronic states. Second term, the delta function $\delta(E_f - E_i - \hbar\omega)$ represents the energy conservation in the photoemission process, where $\hbar\omega$ is the photon energy. Last term, $f(E, T)$ represents the Fermi-Dirac distribution function of electrons at finite temperature.

Under the sudden approximation (emission of the electron is assumed to be sudden and no post-interaction with the system), one can factorize the initial and final state wave functions as a product of one-electron wave function that represents photoelectron and other $N-1$ electrons wave function that treat $N-1$ electrons separately.

$$|\psi_i^N\rangle = |\phi_i^k\rangle|\psi_i^{N-1}\rangle \quad (2.12)$$

$$|\psi_f^N\rangle = |\phi_f^k\rangle|\psi_f^{N-1}\rangle \quad (2.13)$$

where $|\phi_i^k\rangle$ and $|\phi_f^k\rangle$ represent the initial and final state wavefunctions of a photoemitted electron, which has initial momentum k and final kinetic energy E_k . On the other hand, $|\psi_i^{N-1}\rangle$ and $|\psi_f^{N-1}\rangle$ represent initial and final states wavefunction for remaining $N-1$ electron. Using equations (2.12) and (2.13), one can write the transition matrix element as,

$$|\langle\psi_f^N|H_{int}|\psi_i^N\rangle|^2 = |\langle\phi_f^k|H_{int}|\phi_i^k\rangle|^2 |\langle\psi_f^{N-1}|\psi_i^{N-1}\rangle|^2 \quad (2.14)$$

where the first term $|\langle\phi_f^k|H_{int}|\phi_i^k\rangle|^2$ represent the one-electron transition matrix element, and the second term $|\langle\psi_f^{N-1}|\psi_i^{N-1}\rangle|^2$ is for $N-1$ remaining electron, called overlap integral. The second term is the probability of $N-1$ electrons present in the final state f after removing the one electron.

In the case of a weakly interacting electron system, initial and final wavefunctions for remaining $N-1$ electrons can be assumed to equal, i.e. $|\psi_i^{N-1}\rangle = |\psi_f^{N-1}\rangle$, then overlap integral (second term in equation 2.14) will be unity for one particular state and zero for other states. Therefore, the total transition matrix is reduced to one electron transition matrix element, and photoemission intensity can be written as

$$I \propto |\langle\phi_f^k|H_{int}|\phi_i^k\rangle|^2 \delta(E_f - E_i - \hbar\omega) f(E, T) \quad (2.15)$$

Suppose the first term (one electron transition matrix element) of this above equation is non-zero. In that case, ARPES spectra will show a single peak, given by the second term of the above equation, which is a delta function (*i.e.*, noninteracting particle picture) as shown in Fig. 2.8(a).

On the other hand, in the case of a strongly interacting electrons picture, all the terms in the overlap integral will give some value, *i.e.*, it will not be unity. Consequently, ARPES spectra show a broadened peak associated with some

satellite peaks, as shown in Fig. 2.8(b). Assuming the $N-1$ electron final state has m excited eigenstates, the photoemission intensity can be written as

$$I \propto \sum_{f,i,k} |\langle \phi_f^k | H_{int} | \phi_i^k \rangle|^2 A(k, E) f(E, T) \quad (2.16)$$

where $A(k, E)$ is called spectral function, which can be expressed as

$$A(k, E) = \sum_m |\langle \psi_{f,m}^{N-1} | \psi_{i,m}^{N-1} \rangle|^2 \delta(E_f - E_i - \hbar\omega).$$

The spectral function can be evaluated using single-particle green's function as

$$A(k, E) = \frac{1}{\pi} |\text{Im}G(k, E)| \quad (2.17)$$

where $G(k, E)$ can be written using self-energy $\Sigma(k, E)$ of electron

$$G(k, E) = \frac{1}{E - E_k^0 - \Sigma(k, E)} \quad (2.18)$$

where E_k^0 represents the one-electron energy.

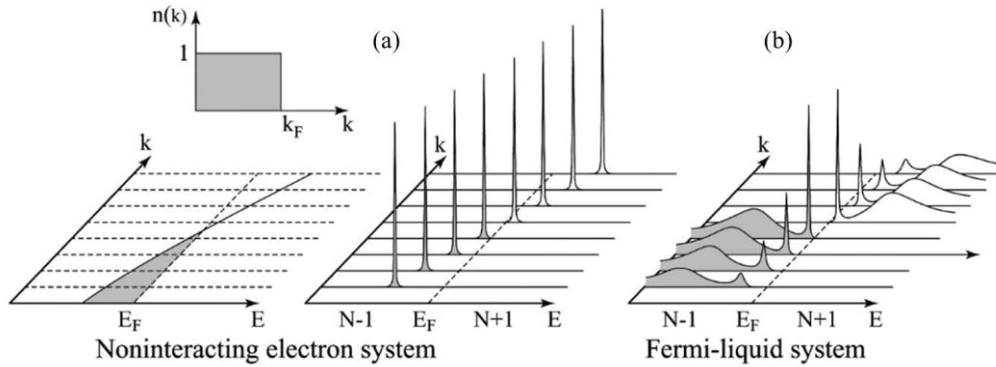


Figure 2.8: Interacting and noninteracting case (a) ARPES spectra represents a single electron band crossing across the E_F in (a) non-interaction electron system and (b) strongly interacting electron system, figure adapted from ref. [45].

Then spectral function $A(k, E)$ can be written as

$$A(k, E) = \frac{1}{\pi} \left| \frac{\text{Im}\Sigma(k, E)}{(E - E_k^0 - \text{Re}\Sigma(k, E))^2 + (\text{Im}\Sigma(k, E))^2} \right|. \quad (2.19)$$

Where $\text{Im}\Sigma(k, E)$ and $\text{Re}\Sigma(k, E)$ are Imaginary and real part of self-energies. The above equation is frequently used and contains all the information of the interacting electron picture, which is often used to extract the self-energies.

2.2.3 Matrix Element Effect

The matrix element is essential in the photoemission intensity [first part in the equation (2.16)]. It is related to the experimental geometry (polarization dependencies) and photoionization cross sections which depend on excitation photon energy. As explained before in section 3.2.2, matrix element can write as

$$|M_{f,i}^k| = |\langle \phi_f^k | H_{int} | \phi_i^k \rangle| \quad (2.20)$$

where $H_{int} = \vec{A} \cdot \vec{P}$ represent the dipole contribution, here \vec{A} is constant vector potential and its direction is parallel to the electric field (\vec{E}) direction, i.e., $\vec{A} \parallel \vec{E}$, which is the deciding factor in defining polarization. The wave function $\phi_f^k(\phi_i^k)$ is the final(initial) electron wave function states. To have nonvanishing photoemission intensity, the integrand of the above equation (2.20), must be an even function with respect to the mirror plane. The simple schematic geometry of a photoemission experimental setup is shown in Fig. 2.9, where a mirror plane is perpendicular to xy plane (sample surface). Here, the photoelectron detection plane is matched with the mirror plane of the crystal; particularly, it is in the xz plane (Fig. 2.9). We assumed that the final-state wave function ϕ_f^k is free-electron-like, and that ϕ_f^k does not change sign under the symmetry operation y to $-y$, even function under the mirror plane. When the direction of the electric field (\vec{E}) or vector potential (\vec{A}) is parallel to the plane of incidence (mirror plane), it is defined as **p**-polarization geometry, and if perpendicular to the plane of incidence (mirror plane), it is defined as **s**-polarization geometry as shown in Fig. 2.9.

As we discussed above for **p**-polarization geometry, \vec{A} lies on the plane of incidence, and the operator part $\vec{A} \cdot \vec{P}$ can be written as $\vec{A} \cdot \vec{P} = -i\hbar(A_x\partial_x + A_z\partial_z)$, which is even under the mirror symmetry operation ($y = -y$). If the initial electron wave function ϕ_i^k is odd under the mirror symmetry operation, i.e., $\phi_i^k(x, -y, z) = -\phi_i^k(x, y, z)$, then the one-electron matrix element ($M_{f,i}^k$) should be exactly zero. Therefore, to have a nonvanishing photoemission intensity, the initial wave function (ϕ_i^k) should be even concerning the mirror plane. On the other hand, in the case of **s**-polarization geometry, \vec{A} is perpendicular to the plane of incidence, and the operator part $\vec{A} \cdot \vec{P}$ can be written as $\vec{A} \cdot \vec{P} = -i\hbar(A_y\partial_y)$, which

is odd under the mirror symmetry operation ($y = -y$). Therefore, to get a nonvanishing photoemission intensity, the initial wave function should be odd with respect to mirror symmetry.

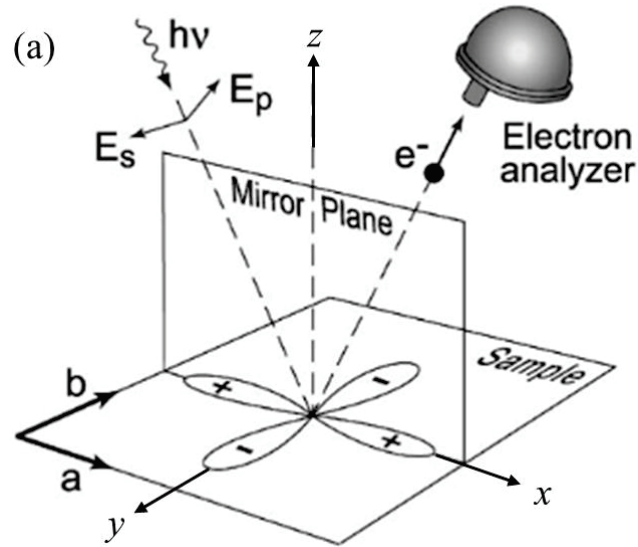


Figure 2.9: The schematic diagram of the mirror plane perpendicular to the x - y plane. The figure is taken from ref. [45].

Thus, there are cases according to the given geometry which permits non-zero matrix element $M_{f,i}^k$ or photoemission intensity.

PES intensity $\propto M_{f,i}^k = \langle \phi_f^k H_{int} \phi_i^k \rangle $	
p -polarization ($\mathbf{A} \parallel$ Mirror plane)	ϕ_i^k even $\langle + + + \rangle \Rightarrow \mathbf{A}$ even
s -polarization ($\mathbf{A} \perp$ Mirror plane)	ϕ_i^k odd $\langle + - - \rangle \Rightarrow \mathbf{A}$ odd

Here \mathbf{A} even denotes p -polarization geometry, and \mathbf{A} odd denotes the s -polarization geometry.

2.2.4 Surface Sensitivity of ARPES

Photoelectrons have a much shorter mean-free path than incident photons, which restricts probing depth and makes photoemission spectroscopy surface sensitive. In the second step of the three-step model, the excited electron had to go through the solid to reach the surface. It may lose energy during this process due to interactions with other electrons, phonons, or contaminants. As a result, the photoemission signal has a continuous background that can be removed if necessary.

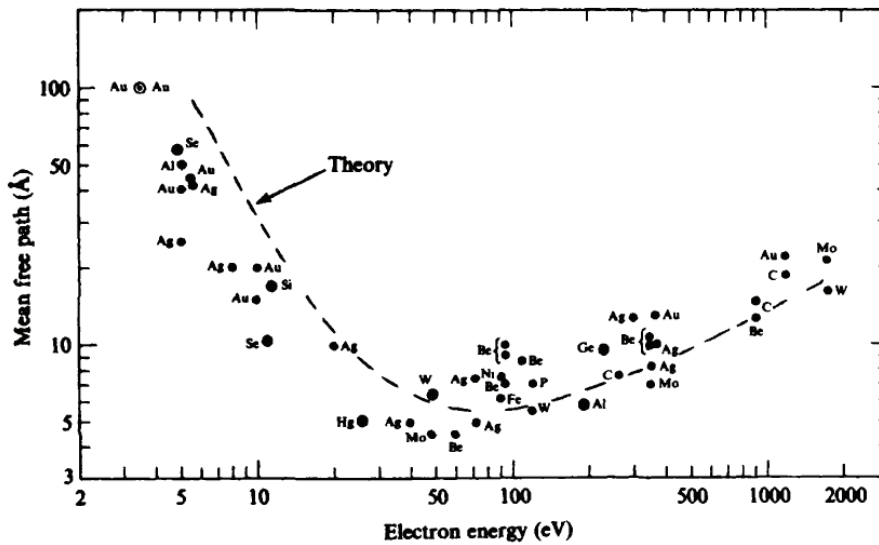


Figure 2.10: The Universal curve for electron inelastic mean free path in the different elements, figure take from ref. [52].

The inelastic mean free path (IMFP) describes how far an electron can go through a solid before becoming inelastically scattered. The inelastic mean free path of electrons formed a universal curve for most elements. The universal curve for the mean free path as a function of electron energy is shown in Fig. 2.10, which shows a minimum mean free path around 50 eV electron kinetic energy in solids. In the case of ARPES spectra taken at photon energies of 20 - 100 eV, the mean free path is around 5 - 10 Å [51,52]. Thus, the ARPES intensity mainly comes from the first few layers of the sample surface, making it an extremely surface-sensitive technique. Due to the small mean free path of excited electrons, ARPES measurements need a very clean, well-ordered surface and ultra-high vacuum (UHV) conditions. This is why we need UHV (usually $\sim 10^{-9}$ pascal) to perform ARPES measurement.

2.3 Major Component of Laser Based μ –ARPES System

We have performed all the ARPES measurements using our state-of-the-art high-resolution laser-based ARPES system at the Hiroshima Synchrotron Radiation Center (HiSOR) laboratory. The layout of our High-resolution μ –ARPES system depicts in Fig. 2.11, showing the component used to produce laser light for measurement, which consists of three main components: (1) Vacuum ultraviolet (VUV) laser system consisting of a green laser (Millenia, Spectra physics), (2) Mode-locked Ti-sapphire laser (Tsunami, spectra physics), and (3) High-order harmonic generator (HarmoniXX, A. P. E.). Firstly, the Ti: sapphire crystal is pumped from the green laser, generating infra-red pulses covering 764–810 nm. These infra-red pulses pass through the nonlinear optical crystals inside the High-order harmonic generator, by which the fourth harmonic is separated, which has a VUV-region from 191 to 210 nm (6.90-5.90 eV). After that, the separated fourth harmonic is guided to the main chamber window for ARPES measurements using an optical setting as shown in Fig. 2.11(a) and finally focused on the sample surface using a focusing lens as marked in Fig. 2.11(b). Emitted photoelectrons from the sample are using equipped with a VG-Scienta R4000 electron analyzer. Specifications of our laser μ –ARPES system are given in table 2.1.

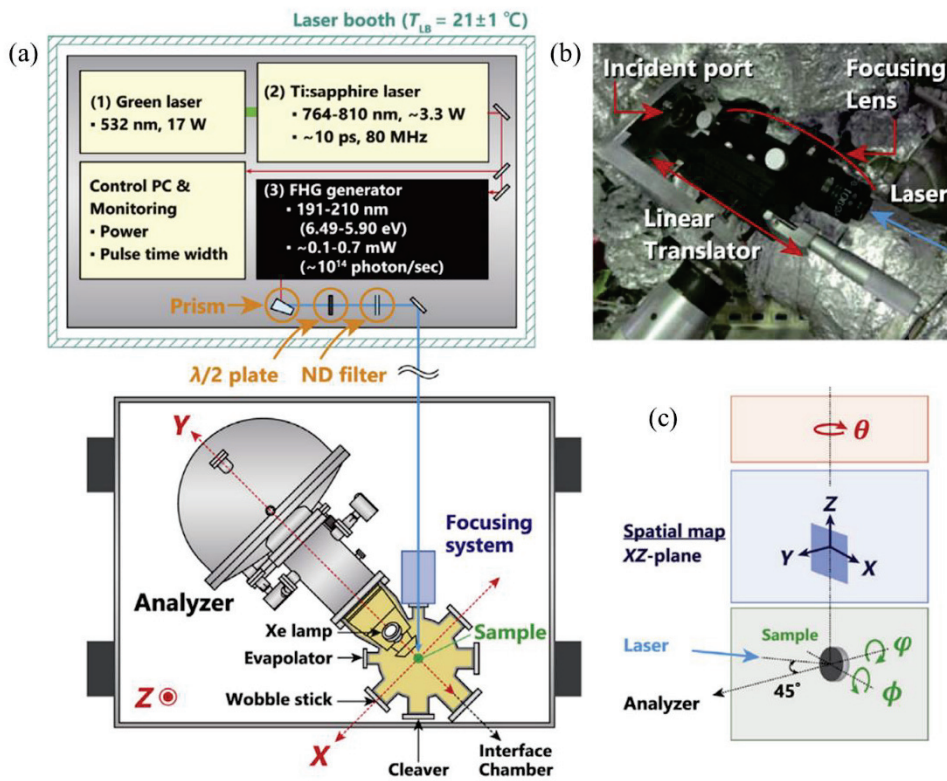


Figure 2.11: The schematic of laser μ -ARPES system (a) depicts the Schematic layout of the laser μ -ARPES system. (b) represents the *ex-situ* optical focusing system. (c) Schematic diagram of the measurement geometry of the laser-based μ -ARPES system. Figures are taken from ref. [53].

In the present ARPES measurements (in this thesis), the photon energy of the laser was tuned to 6.3 eV, and the laser spot size on the sample surface was $<10 \mu\text{m}$ [53]. Fig. 2.11(c) shows the geometry of the μ -ARPES system, where laser light enters at a 45° angle from the analyzer axis. The analyzer slit is aligned with the incidence plane of laser light. Here, the X- and Z-axes of the manipulator are parallel and normal to the analyzer slit, respectively, and the Y-axis is along the analyzer lens axis. The polar (θ), tilt (ϕ), and azimuthal (ϕ) angles are rotation angles around the Z-axis, X-axis, and Y-axis, respectively.

Table 2.1: Specifications of the μ -ARPES system[53]

Photon energy	5.90-6.49 eV
Photon flux	$> \sim 10^{14}$ photons
Repetition rate	~ 80 MHz
Pulse duration	~ 10 ps
Spatial resolution (spot size)	$< 5 \mu\text{m}$
Polarization	LV to LH
Energy resolution	$< 260 \mu\text{eV}$
Angular resolution	$< 0.05^\circ$
Lowest temperature	5.3 K (5-axis) 10 K (6-axis)
Travel range (XY) (Z)	± 15 mm 200 mm
XYZ resolution (nominal) (actual)	± 1 nm $\pm 0.1 \mu\text{m}$

2.3.1 Sample Preparation for ARPES Measurement

Because ARPES is a surface-sensitive probe, it requires a very clean and flat surface to measure them in ARPES. To do so, the sample is mounted in the geometry shown in Fig. 2.12. The crystals are initially chopped into pieces measuring around 1.5 mm, 1.5 mm, and 0.5 mm in size. After that, tiny crystals are mounted on the copper pin using silver epoxy adhesive, which also provides electrical conduction for low electrically conducting samples. Silver epoxy ensures good electrical contact with the sample holder for other samples with weak electrical conductivity. Another layer of epoxy is then used to attach a ceramic top post to the sample. Afterward, the sample is mounted in the load lock sample rack. When the vacuum reaches 10^{-6} Pa inside the load lock, the sample is transferred to the main chamber for ARPES measurement and cooled down to low temperature in a few hours (depending on the measurement requirement). To get a clean surface, the sample was cleaved using *in-situ* using a screwdriver at the base pressure of $\sim 3 \times 10^{-9}$ Pa. The exposed surface was usually gleaming, indicating a flat surface.

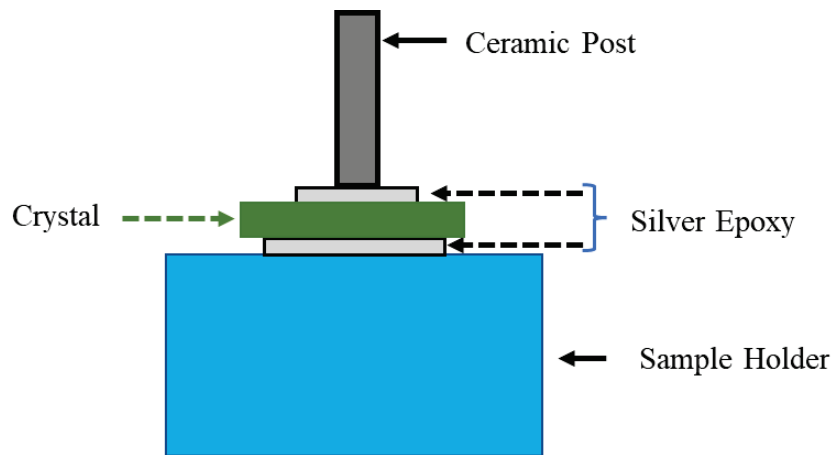


Figure 2.12: The schematic of the single crystal sample geometry mounted inside the ARPES measurement chamber. To ensure the clean surface for measurement, the Ceramic top-post was used to cleave the sample inside (UHV).

Chapter 3: Many-body Interactions

Many-body effects and their interactions are the heart of some of today's most intriguing challenges in condensed matter physics, and complex materials commonly exhibit the simultaneous presence of several effects. Besides other interactions, electron-phonon interaction is one of the fundamental interactions of the quasiparticles in solids, and plays a significant role in the variety of physical phenomena near the E_F , such as electrical conductivity, thermoelectric properties, bandgap, and BCS superconductivity. In fact, electron-phonon interactions are the vital ingredient at elevated temperatures, such as at RT electronic applications. So far, several experimental measurements, such as Helium atom scattering (HAS), and heat capacity measurement, have been utilized to evaluate the electron-phonon interactions. However, ARPES is also very renowned for evaluating electron-phonon interactions due to recent advances. Therefore, in this chapter, we will give the basic theoretical formulation of electron-phonon interaction and its evaluation using ARPES measurements. We will also give a short overview of electron-electron and electron-defect interactions. Apart from this, we will review some of the previous studies of many-body interactions on the surface of TIs using ARPES and other techniques.

3.1 ARPES Spectral Function

As we have described in the previous chapter, under the sudden approximation single particle ARPES spectral function can be written as,

$$A(k, \omega) = \frac{1}{\pi} \left| \frac{\text{Im}\Sigma(k, \omega)}{(\omega(k) - \omega_k^0 - \text{Re}\Sigma(k, \omega))^2 + (\text{Im}\Sigma(k, \omega))^2} \right| \quad (3.1)$$

where $\omega(k)$ and k represent the electron energy and momentum, respectively, and ω_k^0 is the energy for the noninteracting band. The self-energies, such as the Real $\text{Re}\Sigma(k, \omega)$, imaginary $\text{Im}\Sigma(k, \omega)$ part of self-energies, contains all the information about quasiparticle interactions. One can evaluate different type many-body interactions effect such as electron-electron (*el-el*), electron-phonon (*el-ph*), and electron-defect (*el-de*), etc. by analysing the ARPES self-energies. In the coming sections, we will discuss the different types of quasiparticle scattering, such as the *el-el*, *el-ph*, and *el-de* scattering.

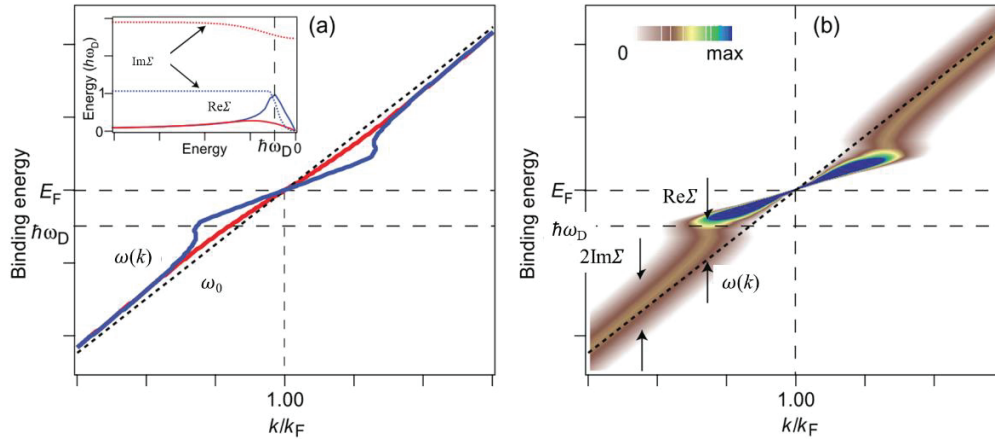


Figure 3.1: Effect of electron-phonon interaction on band dispersion (a) Schematic representation of band renormalization of the energy band near the E_F , where bare band dispersion ω_0 represented by a dashed line, and solid lines representing the band renormalization $\omega(k)$ at low (blue) and high (red) temperatures. (b) spectral function $A(\omega, k, T)$ representation at low temperature showing sharpening due to band renormalization near E_F . The arrows indicate how the self-energies are related to changes in the band dispersion. The Inset of figure (a) shows self-energies: $\text{Re}\Sigma(k, \omega)$ and $\text{Im}\Sigma(k, \omega)$ for low (blue) and high (red) temperatures. Figures adapted from ref. [54].

Fig. 3.1 shows the schematic of the band dispersion, where Fig. 3.1(a) depicts the band renormalization from bare-band dispersion due to *el-ph* interactions at low (blue) and high (red) temperature and peak-like nature in the band dispersion close to E_F at low temperature (blue) marked at characteristic Debye energy. On the other hand, Fig. 3.1(b) shows a schematic of ARPES spectral function at low temperature, showing how self-energies affect the band dispersions. One can see $\text{Re}\Sigma(k, \omega)$ are related to the renormalization (deviation from the bare band) of the energy band close to the E_F , and $\text{Im}\Sigma(k, \omega)$ evolves from the broadening of the energy bands.

The lifetime (τ), the inverse of Line width (Γ) or $\text{Im}\Sigma(k, \omega)$ are directly related to the broadening of energy bands, which characterizes the decay of excited electrons or holes. In general, the total line width is the contribution of mainly three kinds of interactions: *el-de*, *el-el*, and *el-ph* interactions. Total line width can be written as:

$$\Gamma = \frac{\hbar}{\tau} = \Gamma_{el-de} + \Gamma_{el-el} + \Gamma_{el-ph}, \quad (3.2)$$

However, one can analyze each individual interaction separately by using some assumptions. In the coming section, we will discuss these three interactions.

3.1.1 Electron-defect Interactions

The Electron-defect or electron-impurity interactions are the elastic scattering process that limits the mean free path of the excited electrons and contributes to the total line width (Γ). Generally, line width due to electron-defect scattering Γ_{el-de} is not dependent on either energy or temperature and thus only acts as an offset to the total line width Γ at the E_F . However, some defects can be thermally excited in some systems that can enhance the Γ_{el-de} at elevated temperatures.

3.1.2 Electron-electron Interactions

The Electron-electron interactions are the inelastic scattering process that induces many decay channels related to spin density, charge density, single-pair, and triple-pair fluctuations. These *el-el* interactions contribute to the total line width (Γ). However, Γ_{el-el} is dependent on energy; its contribution is more at higher binding energy because the phase space of *el-el* scattering increases. In contrast to Γ_{el-ph} , which increases at high temperatures due to the higher chance of phonon excitations, the temperature dependency of Γ_{el-el} is often relatively minimal. At low temperatures and higher binding energy, the contribution of *el-el* scattering is the dominant scattering process that limits the excited electron lifetime. However, close to the E_F , and especially at high temperatures, Γ_{el-el} can become lower than Γ_{el-ph} .

3.1.3 Electron-phonon Interactions

The Electron-phonon scattering is an inelastic scattering process, a vital scattering process close to the E_F (in the Debye energy range of materials), and has significant temperature dependence. One can separate the Γ_{el-ph} contribution from the total line width Γ experimentally. In the coming sections, we will focus on the theoretical formulation and experimental evaluation of *el-ph* interactions contribution using self-energies.

The Self-energy due to *el-ph* interaction can be derived from the second-order perturbation theory using Matsubara Green's functions. Derived self-energy are following:

$$\Sigma(\omega) = \int_0^{\omega_D} d\tilde{\omega} \alpha^2 F(\tilde{\omega}) P \int_{-\mu}^{\mu'} d\varepsilon \left\{ \frac{f(\varepsilon) + n(\tilde{\omega})}{\omega + \tilde{\omega} - \varepsilon} + \frac{1 - f(\varepsilon) + n(\tilde{\omega})}{\omega - \tilde{\omega} - \varepsilon} \right\} \quad (3.3)$$

$$\begin{aligned} & - i\pi \int_0^{\omega_D} d\tilde{\omega} \alpha^2 F(\tilde{\omega}) \{f(\omega + \tilde{\omega}) + 1 - f(\omega - \tilde{\omega}) \\ & + 2n(\tilde{\omega})\} \end{aligned}$$

$$\Sigma(\omega) = \text{Re}\Sigma(\omega) + i\text{Im}\Sigma(\omega) \quad (3.4)$$

where, f and n are the Fermi and Bose distribution functions, which introduce temperature dependence in the self-energy and $\alpha^2 F(\omega)$ is called the Eliashberg function. From the above equations, $\text{Re}\Sigma(\omega)$ and $\text{Im}\Sigma(\omega)$ parts of self-energies can be written as

$$\begin{aligned} \text{Re}\Sigma(\omega) = \int_0^{\omega_D} d\tilde{\omega} \alpha^2 F(\tilde{\omega}) P \int_{-\mu}^{\mu'} d\varepsilon \left\{ \frac{f(\varepsilon) + n(\tilde{\omega})}{\omega + \tilde{\omega} - \varepsilon} \right. \\ \left. + \frac{1 - f(\varepsilon) + n(\tilde{\omega})}{\omega - \tilde{\omega} - \varepsilon} \right\} \end{aligned} \quad (3.5)$$

$$\begin{aligned} \text{Im}\Sigma(\omega) = -\pi \int_0^{\omega_D} d\tilde{\omega} \alpha^2 F(\tilde{\omega}) \{f(\omega + \tilde{\omega}) + 1 - f(\omega - \tilde{\omega}) \\ + 2n(\tilde{\omega})\} \end{aligned} \quad (3.6)$$

3.1.4 A Short Discussion on the Eliashberg Function

The Eliashberg function is used to quantify the efficiency of scattering electrons, either by absorption (A) or emission (E) of phonon.

$$\alpha^2 F^{E/A}(\varepsilon_i, k; \omega) = \sum_{q, \nu, f} \delta(\varepsilon_i - \varepsilon_f \pm \omega_{q, \nu}) |g^{i, f}(k, q, \nu)|^2 (\omega - \omega_{q, \nu}) \quad (3.7)$$

where, ε_i and ε_f are the initial and final states, which differ by $\hbar\omega$ energy because of absorption and emission of phonon, as shown in Fig. 3.2. The negative (-) and positive (+) sign represents the emission and absorption of phonon, while $g^{i, f}(k, q, \nu)$ represents the *el-ph* matrix element that gives the probability of scattering electrons from an initial state to final states related to a particular phonon mode having momentum q and mode index ν . Summation is taken over for all the final energy states and phonon modes (q, ν).

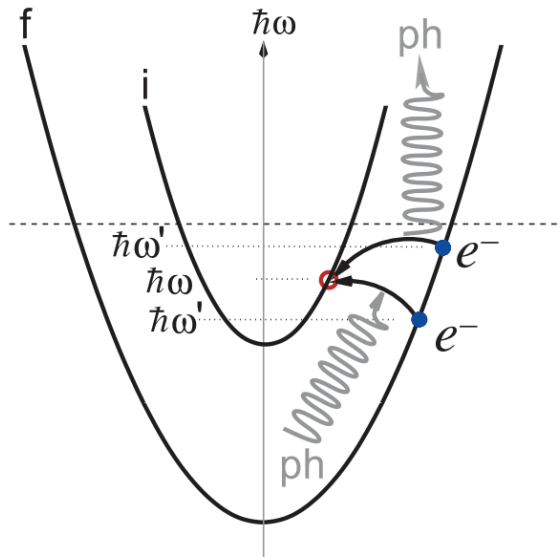


Figure 3.2: Interband scattering mediated by phonon emission and absorption from a filled circle (final state of the hole) to an open circle (starting state of the hole). Figure adapted from [55].

Mass enhancement due to $el-ph$ interactions can be defined by dimensionless coupling parameter λ ,

$$\lambda_{\varepsilon_i, k} = \int_0^{\omega_D} \frac{\alpha^2 F^E(\varepsilon_i, k; \tilde{\omega}) + \alpha^2 F^A(\varepsilon_i, k; \tilde{\omega})}{\tilde{\omega}} d\tilde{\omega}. \quad (3.8)$$

Integration carried out up to maximum phonon frequency or Debye frequency ω_D . Although $el-ph$ scattering is an elastic process, however, changes in the energy of scattered electrons by phonon during absorption or emission of phonon are negligible because phonon energies (in meV) are much smaller than electronic energies (eV). Therefore, one can write:

$$\delta(\varepsilon_i - \varepsilon_f \pm \omega_{q, \nu}) \approx \delta(\varepsilon_i - \varepsilon_f) \quad (3.9)$$

This approximation is called quasielastic approximation, that is $\alpha^2 F^E(\varepsilon_i, k; \omega) = \alpha^2 F^A(\varepsilon_i, k; \omega)$. Therefore, under quasielastic approximation, the coupling constant can be written as-

$$\lambda_{\varepsilon_i, k} = 2 \int_0^{\omega_D} \frac{\alpha^2 F(\varepsilon_i, k; \tilde{\omega})}{\tilde{\omega}} d\tilde{\omega} \quad (3.10)$$

This quasielastic approximation allows us to use the same Eliashberg function for both processes (absorption and emission of phonon).

The *el-ph* interaction basically induces the energy shift (renormalization) from the bare band in the energy dispersion (see Fig. 3.1) and limits electron or hole lifetime. Energy shift or band renormalization is related to the Real part of the electron-phonon self-energy, $\text{Re}\Sigma(\omega)$. On the other hand, lifetime broadening can be evaluated from the imaginary part of electron-phonon self-energy, $\text{Im}\Sigma(\omega)$. As mentioned in equations (3.5) and (3.6), both parts (real and imaginary) of self-energies are fully described by the Eliashberg function. One can calculate the el-ph coupling constant using both the $\text{Re}\Sigma(\omega)$ and $\text{Im}\Sigma(\omega)$ parts of self-energies.

3.1.5 Evaluation of Coupling Parameter using the Real-part of Self-energy-

The electron-phonon coupling (EPC) parameter is commonly determined by the slope of the $\text{Re}\Sigma(\omega)$ at the E_F , that is, $\omega = 0$,

$$\lambda_{\text{ep}} = - \left. \frac{\partial \text{Re}\Sigma(\omega)}{\partial \omega} \right|_{\omega=0} \quad (3.11)$$

Using equation (3.5), we can rewrite,

$$\begin{aligned} &= \lim_{\omega \rightarrow +0} P \int_{-\mu}^{\mu'} d\varepsilon \int_0^{\omega_D} d\tilde{\omega} \alpha^2 F(\tilde{\omega}) \left\{ \frac{f(\varepsilon) + n(\tilde{\omega})}{(\omega + \tilde{\omega} - \varepsilon)^2} \right. \\ &\quad \left. + \frac{1 - f(\varepsilon) + n(\tilde{\omega})}{(\omega - \tilde{\omega} - \varepsilon)^2} \right\} \\ \lambda_{\text{ep}} &= P \int_{-\mu}^{\mu'} d\varepsilon \int_0^{\omega_D} d\tilde{\omega} \alpha^2 F(\tilde{\omega}) \left\{ \frac{f(\varepsilon) + n(\tilde{\omega})}{(\varepsilon - \tilde{\omega})^2} \right. \\ &\quad \left. + \frac{1 - f(\varepsilon) + n(\tilde{\omega})}{(\varepsilon + \tilde{\omega})^2} \right\} \end{aligned} \quad (3.12)$$

(i) Coupling parameter at absolute temperature

At absolute temperature, $T = +0$, Fermi distribution function,

$$f(\varepsilon, T \rightarrow +0) = 1 - \theta(\varepsilon),$$

$$1 - f(\varepsilon, T \rightarrow +0) = \theta(\varepsilon) \quad (3.13)$$

And Bose distribution function,

$$n(\tilde{\omega}, T \rightarrow +0) = 0 \quad (3.14)$$

Then equation (3.12) can be written as,

$$\lambda_{ep} = P \int_{-\mu}^{\mu'} d\varepsilon \int_0^{\omega_D} d\tilde{\omega} \alpha^2 F(\tilde{\omega}) \left\{ \frac{1 - \theta(\varepsilon)}{(\varepsilon - \tilde{\omega})^2} + \frac{\theta(\varepsilon)}{(\varepsilon + \tilde{\omega})^2} \right\} \quad (3.15)$$

Solving the above integral for the metallic system, where chemical potential is usually much higher than Debye energy, $0 < \tilde{\omega} < \omega \ll \mu$, Then the coupling parameter at $T = 0$ can be evaluated as,

$$\lambda_{ep}(0) \cong 2 \int_0^{\omega_D} d\tilde{\omega} \frac{\alpha^2 F(\tilde{\omega})}{\tilde{\omega}} \quad (3.16)$$

(ii) Coupling Parameter at Finite Temperature

Solving equation (3.15) for finite temperature, we will have a coupling parameter at finite temperature. The final result can be written as,

$$\lambda_{ep} = - \left. \frac{\partial \text{Re}\Sigma(\omega)}{\partial \omega} \right|_{\omega=0} = -2 \int_0^{\omega_D} d\tilde{\omega} \frac{\alpha^2 F(\tilde{\omega})}{\tilde{\omega}} \cdot G(y) \quad (3.17)$$

$$G(y) = -4 \left(\frac{y}{\pi} \right)^2 \sum_{k=0}^{\infty} \frac{2k+1}{\left\{ (2k+1)^2 + \left(\frac{y}{\pi} \right)^2 \right\}^2}$$

Here, thermodynamic quantity, $\beta = (1/k_B T)$ & $y = \beta \tilde{\omega}$, Now we solve the above equation for low and high temperatures.

(a) For low temperature

At low temperature, Debye energy is much higher than thermal energy,

$$\omega_D \gg k_B T, \quad y = \beta \tilde{\omega} = \frac{\tilde{\omega}}{k_B T} \gg 1$$

Solving equation (3.17) for the low-temperature region using the above relations, coupling parameter at low temperature can be written as,

$$\lambda_{ep}(T) = - \left. \frac{\partial \text{Re}\Sigma(\omega)}{\partial \omega} \right|_{\omega=0} = 2 \int_0^{\omega_D} d\tilde{\omega} \frac{\alpha^2 F(\tilde{\omega})}{\tilde{\omega}} + \frac{\pi^2}{3} 2 \int_0^{\omega_D} d\tilde{\omega} \frac{\alpha^2 F(\tilde{\omega})}{\tilde{\omega}^3} (k_B T)^2.$$

$$\lambda_{ep}(T) = \lambda(0) + m(k_B T)^2 \quad (3.18)$$

$$\text{Here, } m = \frac{\pi^2}{3} 2 \int_0^{\omega_D} d\tilde{\omega} \frac{\alpha^2 F(\tilde{\omega})}{\tilde{\omega}^3}$$

Therefore, at low temperature, total EPC parameter, $\lambda(T)$ is the contribution of the coupling constant at absolute zero temperature (0 K) and temperature-dependent term (square of temperature).

(b) For High Temperature

At high temperature, Debye energy is much higher than thermal energy,

$$\omega_D \ll k_B T, \quad y = \beta \tilde{\omega} = \frac{\tilde{\omega}}{k_B T} \ll 1$$

In this case, from the equation (3.17),

$$G(y) = -4 \left(\frac{y}{\pi}\right)^2 \sum_{k=0}^{\infty} \frac{2k+1}{\left\{(2k+1)^2 + \left(\frac{y}{\pi}\right)^2\right\}^2}$$

For $y \ll 1$,

$$\frac{2k+1}{\left\{(2k+1)^2 + \left(\frac{y}{\pi}\right)^2\right\}^2} \approx \frac{2k+1}{\{(2k+1)^2\}^2} = \frac{1}{(2k+1)^3}$$

That is,

$$\sum_{k=0}^{\infty} \frac{2k+1}{\left\{(2k+1)^2 + \left(\frac{y}{\pi}\right)^2\right\}^2} = \sum_{k=0}^{\infty} \frac{1}{(2k+1)^3}$$

Using Riemann zeta function, $\xi(s) = \sum_{k=1}^{\infty} \frac{1}{(k)^s}$

$$\begin{aligned} \xi(3) &= \sum_{k=1}^{\infty} \frac{1}{(k)^3} = \sum_{k=1}^{\infty} \left\{ \frac{1}{(2k)^3} + \frac{1}{(2k-1)^3} \right\} = \sum_{k=1}^{\infty} \left\{ \frac{1}{(2k)^3} + \sum_{k=1}^{\infty} \frac{1}{(2k+1)^3} \right\} \\ &= \frac{1}{8} \sum_{k=1}^{\infty} \left\{ \frac{1}{(k)^3} + \sum_{k=0}^{\infty} \frac{1}{(2k-1)^3} \right\} = \frac{1}{8} \xi(3) + \sum_{k=0}^{\infty} \frac{1}{(2k-1)^3} \\ &\therefore \sum_{k=0}^{\infty} \frac{1}{(2k-1)^3} = \frac{7}{8} \xi(3), \xi(3) = 1.202056963 \dots \end{aligned}$$

Therefore,

$$\begin{aligned} G(y) &= -4 \left(\frac{y}{\pi}\right)^2 \sum_{k=0}^{\infty} \frac{2k+1}{\left\{(2k+1)^2 + \left(\frac{y}{\pi}\right)^2\right\}^2} \approx -4 \left(\frac{y}{\pi}\right)^2 \frac{7}{8} \xi(3) = -\left(\frac{y}{\pi}\right)^2 \frac{7}{2} \xi(3) \\ &= -\left(\frac{1}{\pi}\right)^2 \frac{7}{2} \xi(3) (\beta\tilde{\omega})^2 = -\left(\frac{1}{\pi}\right)^2 \frac{7}{2} \xi(3) \left(\frac{\tilde{\omega}}{k_B T}\right)^2 \end{aligned}$$

Using above $G(y)$, Equation (3.17) can be written,

$$\begin{aligned} \lambda_{ep} &= -\left. \frac{\partial \text{Re}\Sigma(\omega)}{\partial \omega} \right|_{\omega=0} = -2 \int_0^{\omega_D} d\tilde{\omega} \frac{\alpha^2 F(\tilde{\omega})}{\tilde{\omega}} \cdot G(y) \\ &= 2 \int_0^{\omega_D} d\tilde{\omega} \frac{\alpha^2 F(\tilde{\omega})}{\tilde{\omega}} \left(\frac{1}{\pi}\right)^2 \frac{7}{2} \xi(3) \left(\frac{\tilde{\omega}}{k_B T}\right)^2 \\ \lambda_{ep} &= \left\{ \frac{7}{\pi^2} \xi(3) \cdot \int_0^{\omega_D} d\tilde{\omega} \alpha^2 F(\tilde{\omega}) \tilde{\omega} \right\} \left(\frac{1}{k_B T}\right)^2 \\ \lambda_{ep} &= b \left(\frac{1}{k_B T}\right)^2 \propto \frac{1}{T^2} \tag{3.19} \\ \text{here, } b &= \left\{ \frac{7}{\pi^2} \xi(3) \cdot \int_0^{\omega_D} d\tilde{\omega} \alpha^2 F(\tilde{\omega}) \tilde{\omega} \right\} \end{aligned}$$

In conclusion, the above equation indicates that the coupling constant is inversely proposal to the square of temperature. Therefore, one can conclude from the above sections (a and b), that at a low-temperature regime (below characteristics Debye temperature), the EPC parameter λ_{ep} is proportional to the square of temperature; on the other hand, at high temperature, inversely proportional to the square of temperature (above characteristics Debye temperature).

3.1.6 Coupling Parameter from Imaginary-part of Self-energy

The $\text{Im}\Sigma$ or line width is essentially the same quantity. It can be written as

$$\Gamma(\omega, T) = \frac{\hbar}{\tau} = 2|\text{Im}\Sigma(\omega, T)| \tag{3.20}$$

From equation (3.6), temperature-dependent $\text{Im}\Sigma$,

$$\begin{aligned} \text{Im}\Sigma(\omega, T) &= -\pi \int_0^{\omega_D} d\tilde{\omega} \alpha^2 F(\tilde{\omega}) \{f(\omega + \tilde{\omega}, T) + 1 - f(\omega - \tilde{\omega}, T) + 2n(\tilde{\omega}, T)\} \\ &= -\pi \int_0^{\omega_D} d\tilde{\omega} \alpha^2 F(\tilde{\omega}) \{f(\omega + \tilde{\omega}, T) + f(\tilde{\omega} - \omega, T) + 2n(\tilde{\omega}, T)\} \end{aligned}$$

At E_F ($\omega=0$),

$$\begin{aligned}\Gamma(0, T) &= 2|\text{Im}\Sigma(0, T)| = 2\pi \int_0^{\omega_D} d\tilde{\omega} \alpha^2 F(\tilde{\omega}) \{f(\tilde{\omega}, T) + f(\tilde{\omega}, T) + 2n(\tilde{\omega}, T)\} \\ \Gamma(0, T) &= 2\pi \int_0^{\omega_D} d\tilde{\omega} \alpha^2 F(\tilde{\omega}) \cdot 2\{f(\tilde{\omega}, T) + n(\tilde{\omega}, T)\} \\ &= 2\pi \int_0^{\omega_D} d\tilde{\omega} \alpha^2 F(\tilde{\omega}) \cdot 2 \left[\frac{1}{e^{\beta\tilde{\omega}} + 1} + \frac{1}{e^{\beta\tilde{\omega}} - 1} \right] \\ &= 8\pi \int_0^{\omega_D} d\tilde{\omega} \alpha^2 F(\tilde{\omega}) \cdot \left[\frac{1}{e^{\beta\tilde{\omega}} - e^{-\beta\tilde{\omega}}} \right]\end{aligned}$$

For elevated temperatures,

$$\omega_D \ll k_B T, \quad e^{\beta\tilde{\omega}} \approx 1 + \beta\tilde{\omega}, \quad e^{-\beta\tilde{\omega}} \approx 1 - \beta\tilde{\omega}$$

Therefore,

$$\begin{aligned}\Gamma(0, T) &= 8\pi \int_0^{\omega_D} d\tilde{\omega} \alpha^2 F(\tilde{\omega}) \cdot \left[\frac{1}{1 + \beta\tilde{\omega} - 1 + \beta\tilde{\omega}} \right] = 8\pi \int_0^{\omega_D} d\tilde{\omega} \alpha^2 F(\tilde{\omega}) \cdot \left[\frac{1}{2\beta\tilde{\omega}} \right] \\ &= 2\pi \cdot 2 \int_0^{\omega_D} d\tilde{\omega} \frac{\alpha^2 F(\tilde{\omega})}{\tilde{\omega}} \cdot \frac{1}{\beta} = 2\pi\lambda(0) \cdot k_B T\end{aligned}$$

Using equation (3.19), one can write

$$\Gamma(0, T) = 2\pi \cdot \lambda(0) \cdot k_B T \quad (3.21)$$

where $\lambda(0) = 2 \int_0^{\omega_D} d\tilde{\omega} \frac{\alpha^2 F(\tilde{\omega})}{\tilde{\omega}}$. The equation (3.21) gives a fascinating conclusion, one can calculate the EPC parameter at zero temperature by analyzing the temperature-dependent line width at the E_F .

3.2 Kramers-Kronig Relation

It is a bidirectional relation, frequently used in mathematics; it connects real and imaginary parts of complex functions. As self-energy is a causal function, it should satisfy the Kramers-Kronig relation. Relations are following;

$$\text{Re}\Sigma_{el-ph}(\omega) = \frac{1}{\pi} P \int_{-\infty}^{\infty} \frac{\text{Im}\Sigma_{el-ph}(\omega')}{\omega' - \omega} d\omega' \quad (3.22)$$

$$\text{Im}\Sigma_{el-ph}(\omega) = -\frac{1}{\pi} P \int_{-\infty}^{\infty} \frac{\text{Re}\Sigma_{el-ph}(\omega')}{\omega' - \omega} d\omega' \quad (3.23)$$

where $P = \text{Cauchy principal value}$. If either $\text{Im}\Sigma_{el-ph}$ or $\text{Re}\Sigma_{el-ph}$ of self-energy is known, one can calculate the other energy easily using the above relations.

Fig. 3.3(a) represents the model Eliashberg function calculated using Debye theory, where the step marked as a Debye cut-off energy $\omega_D (\approx 7\text{meV})$. Fig. 3.3 (b) shows the symmetrized $\text{Re}\Sigma$ (red) and $\text{Im}\Sigma$ (green) part of self-energies at 17K evaluated using the Kramers-Kronig relation. First, we evaluated the $\text{Im}\Sigma$ using the Debye model, then evaluated the $\text{Re}\Sigma$ using the Kramers-Kronig relation.

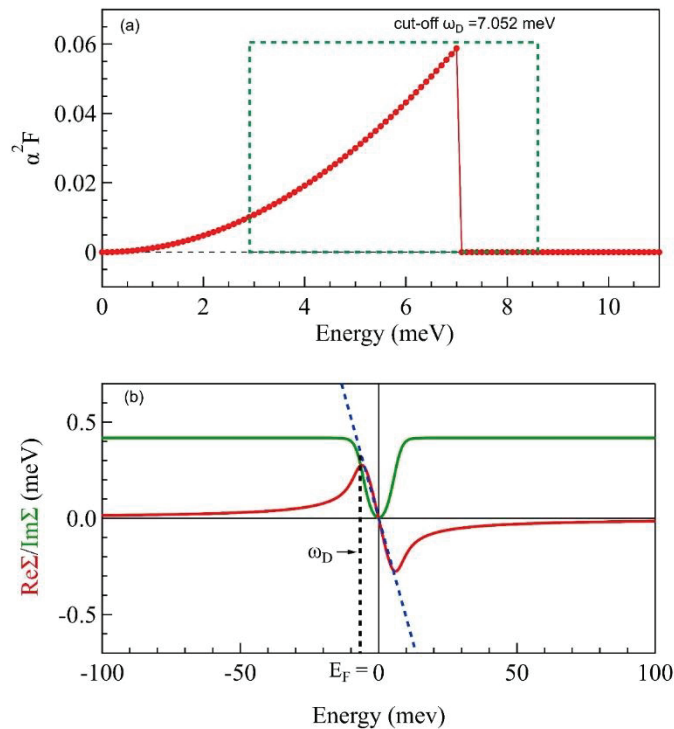


Figure 3.3: Self-energies using Debye model (a) Calculated Eliashberg function for Bi_2Te_3 using surface Debye temperature of Bi_2Te_3 , and (b) depicts the $\text{Re}\Sigma$ (red) and $\text{Im}\Sigma$ (green) part of self-energies calculated using the Debye function at 17K for Bi_2Te_3 , where blue line represents the line on $\text{Re}\Sigma$ at E_F and Debye energy $\omega_D (\approx 7\text{meV})$ is the surface Debye temperature of the Bi_2Te_3 .

3.3 The Electron-phonon Coupling in 3D Topological Insulators

Although Surface Dirac fermions are not allowed to backscatter on the surface of 3D TIs due to spin-momentum locking, but other scattering events (such as $el-el$, $el-ph$, and $el-de$) can affect the ballistic behavior of surface electrons. In general, one can technically grow high-quality single crystals by optimizing the synthesis and minimize the defects in the crystals, which help to minimize the $el-de$ scattering

contribution on the surface of the 3D TIs. However, other scattering events can affect the surface electrons in the 3D TIs. As we discussed in the above sections, the *el-ph* interaction (EPI) is the dominant scattering event over the other scattering, especially at elevated temperatures. Therefore, the EPI would be the main recipe for the surface electrons scattering in the TIs.

So far, many intensive efforts have been made to evaluate EPI strength on the surface of 3D TIs in the last decade using different experimental techniques, for example- ARPES, HAS, and transport measurements. Apart from the experimental analysis, the EPC parameter was also evaluated theoretically using both First-principle calculations and analytical models. However, a consensus about the EPI strength is not achieved because of the conflicting reported values of the EPC parameter. In the context of this section, we will mainly review the previous EPI study on the surface of the 3D TIs such as Bi_2Se_3 and Bi_2Te_3 .

3.3.1 ARPES Study on 3D TIs

Early ARPES study on Bi_2Se_3 suggests that scattering rate is not increased by some adsorbates on the surface because surface states are topologically protected from weak disorder originated from potentials due to adsorbates [56], after that Hoffmann's group evaluated the EPC parameter (λ_{ep}) using temperature-dependent ARPES measurements on Bi_2Se_3 [57]. Fig.3.4 (a)-(c) shows the temperature-dependent band dispersion of Bi_2Se_3 from synchrotron-based ARPES measurement. They focused on the energy range 50 to 100 meV above the DP and found that the evaluated $\text{Im}\Sigma$ was almost constant in this energy range. The EPI parameter was evaluated by the gradient fit in the temperature-dependent $\text{Im}\Sigma$. Fig. 3.4(d) represents the $\text{Im}\Sigma$ at two temperatures for different cleaved samples. Fig. 3.4(e) represents the average of $\text{Im}\Sigma$ for all the samples, EPC parameter evaluated by the line fit using equation (3.21), and evaluated value is $\lambda_{ep} \cong 0.26$. They claimed that this unexpected large value implies a very significant EPC for the topological state. Low temperature kink structure was not resolved in this study.

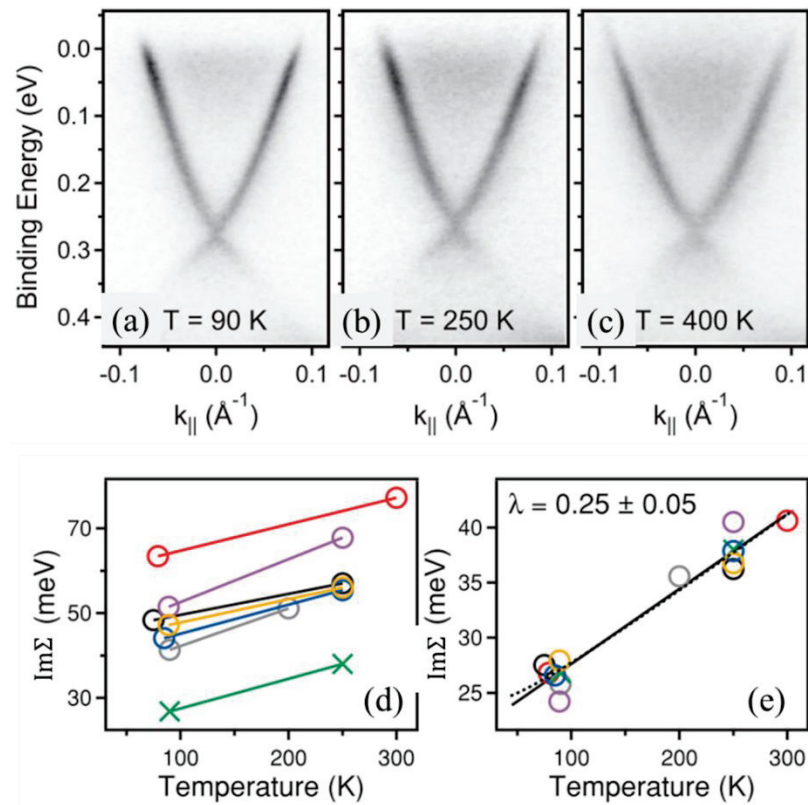


Figure 3.4: ARPES spectra of Bi_2Se_3 , measured at various temperatures shown in (a)-(c). Figure (b) Temperature-dependent $\text{Im}\Sigma$ of different cleaved crystals. (c) average of $\text{Im}\Sigma$ for all the cleaved samples, EPC parameter evaluated by the gradient fit. Figures adapted from the ref.[57].

Soon after this study, Pan *et al.* [58] reported minimal EPC parameter on the TSSs of Bi_2Se_3 . Fig. 3.5(a) and (b) depict the band dispersion of Bi_2Se_3 at 18 K and 255 K, measured using synchrotron-based ARPES. Like R. C. Hatch's report [57], the low-temperature kink structure was also not resolved in this study, as shown in Fig. 3.5(c). Further, they did a temperature-dependent measurement on Bi_2Se_3 and extracted $\text{Im}\Sigma$ at E_F at various temperatures using MDC analysis. Fig. 3.5(d) shows the extracted $\text{Im}\Sigma$ at E_F . By the gradient fit using equation (3.21) in the temperature-dependent $\text{Im}\Sigma(T)$, evaluated EPC parameter was 0.08, which is very low as compared to Hatch's report [57] and one of the weakest coupling parameter ever reported in any material. This small EPC parameter was supported by no appreciable kink found in the magnified band dispersion at low temperature. In both the studies [57,58], they used a synchrotron radiation source, and energy resolution was not better than 8 meV.

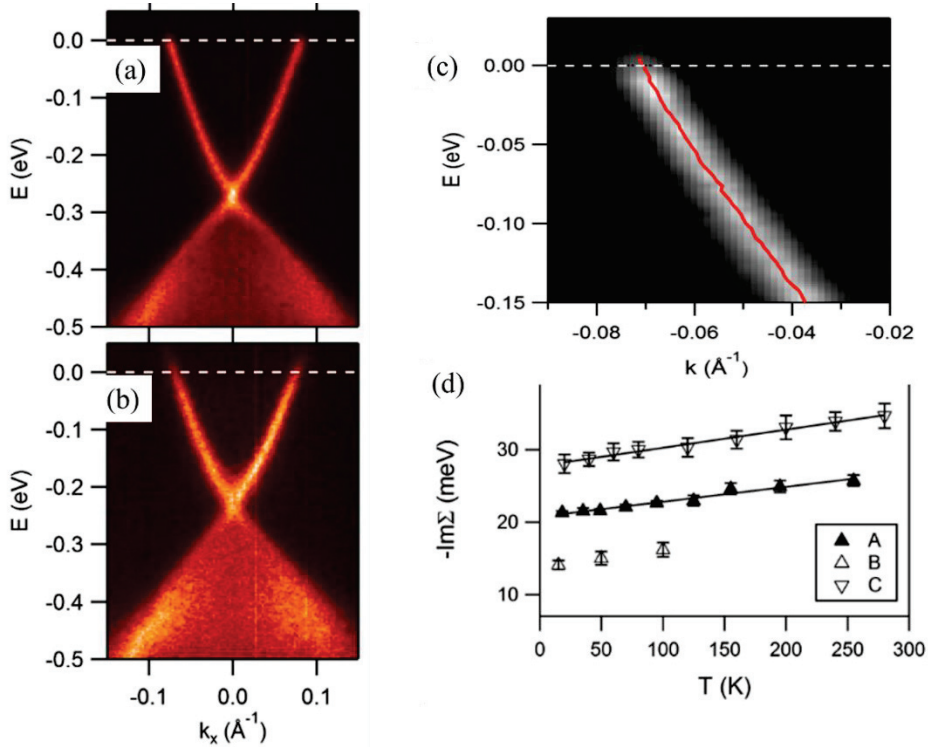


Figure 3.5: ARPES spectra of Bi_2Se_3 , measured at (a) 18 K and (b) 255 K. (c) Low temperature magnified image of left side band from band dispersion depicted in figure 3.5(a), where red line showing evaluated band dispersion from MDC analysis. (d) Temperature-dependent $\text{Im}\Sigma$ at E_F for three different samples, where the line represents the gradient fit. Figures adapted from the ref.[58].

In 2013, Chen *et al.* [41] measured hole chemical composition $\text{Bi}_2(\text{Te}_{3-x}\text{Se}_x)$ with varying x from 0 to 3, using a high-resolution laser-based ARPES system having an energy resolution less than 1 meV, which is much better than the energy resolution in the previous studies. Fig. 3.6(a) shows band dispersion of Bi_2Se_3 along the $\bar{\Gamma} - \bar{K}$ and $\bar{\Gamma} - \bar{M}$ high symmetry directions at 17 K. Fig. 3.6(b) represent MDC along the $\bar{\Gamma} - \bar{K}$ symmetry direction. The left side of Fig. 3.6 (c) and (d) depict the band dispersion from MDC analysis (red points) overlaid by a bare band dashed line along the $\bar{\Gamma} - \bar{K}$ and $\bar{\Gamma} - \bar{M}$ high symmetry directions, where the blue arrow indicates band renormalization (small kink) from the bare band line. The right side of Fig. 3.6 (c) and (d), represents extracted self-energies, where the EPC parameter was evaluated from the gradient fit in $\text{Re}\Sigma$ at E_F . The magnitude of the EPC parameter was reported as 0.17 for Bi_2Se_3 , which deviated from the previous studies on the same TIs material [57,58]. Similarly, the evaluated coupling parameter for n-type Bi_2Te_3 was 0.19. According to their observations, the magnitude of the EPC parameter varies from 0 for p-type Bi_2Te_3 to 0.19 for n-type Bi_2Te_3 , depending on the doping level.

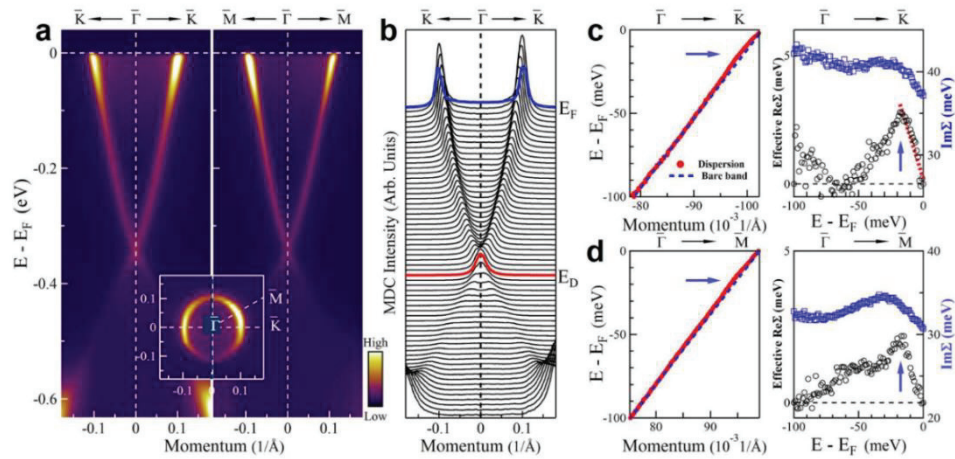


Figure 3.6: ARPES intensity map (a) ARPES spectra of Bi₂Se₃ the $\bar{\Gamma} - \bar{K}$ and $\bar{\Gamma} - \bar{M}$ high symmetry directions at 17 K. (b) MDC along $\bar{\Gamma} - \bar{K}$ direction. Figures (c) and (d) band renormalization (Left side) and extracted self-energies (right side). Figures adapted from the ref. [41].

Soon after, Kondo *et al.* [59] also measured Bi₂Se₃, Cu_xBi₂Se₃, and Bi₂Te₃ using a very-high-resolution laser-based ARPES system. The energy resolution was similar to Chen's results; however, the measured temperature was 7 K. Fig. 3.7 (a2) and (b2) depict band dispersion, and Fig. 3.7 (a3) and (b3) depict Fermi surface (FS) of Bi₂Se₃, and Bi₂Te₃, respectively. By analyzing the band dispersion, they found two kink structures in Re Σ close to E_F , one at 3 meV and the other at 15 meV from E_F , as shown in Fig. 3.7 (a4) and (b4), which suggested that electron coupling with two different phonon modes. From the gradient fit in the Re Σ at E_F , the evaluated EPC parameter is 3, which justify by the electron coupling with spin plasmon. This evaluated coupling parameter is the most extensive EPC parameter ever reported for any material.

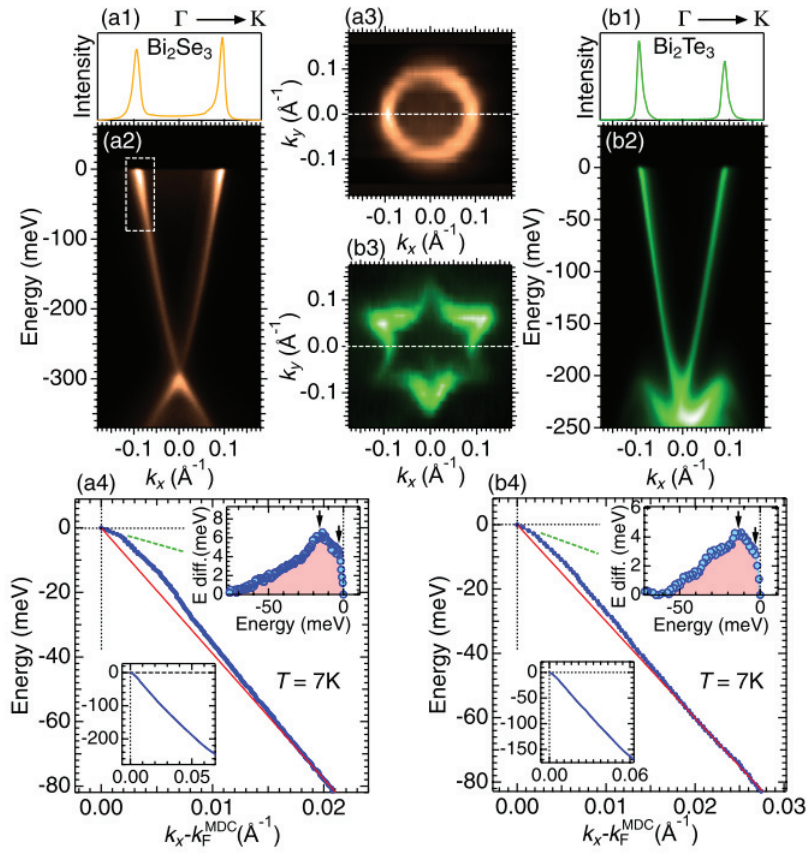


Figure 3.7: ARPES spectra of Bi_2Se_3 and Bi_2Te_3 along the $\bar{\Gamma} - \bar{K}$ high symmetry direction at 7 K. Figure (a1)–(a4) corresponds to Bi_2Se_3 , and figure (b1)–(b4) corresponds to Bi_2Te_3 . (a1) and (b1) depict MDC at E_F . (a2) and (b2) depict the Band dispersion map along $\bar{\Gamma} - \bar{K}$ [dashed lines in (a3) and (b3)]. (a3),(b3) Fermi surface map. (a4) and (b4) represent MDC-derived band dispersions near E_F obtained from the data shown in panels (a2) and (b2). Figures adapted from the ref.[59].

3.3.2 Helium Atom Scattering Study on 3D TIs

The HAS is the surface-sensitive technique (penetration depth $\sim 3\text{-}4 \text{ \AA}$), which provides information about the surface structure and lattice dynamics of material by analyzing the diffracted atom from a monochromatic helium atom impinge on the sample. HAS technique has been used to evaluate the EPC parameter on the surface TIs.

Initially, Surface-phonon dispersions on Bi_2Se_3 (001) were investigated experimentally using HAS technique and theoretically by Zhu *et al.* [60,61]. Fig. 3.8 presents the experimental data as solid orange dots with error bars. The computed surface phonon dispersion curves are represented as black dots superimposed on the experimental data. We will concentrate on two crucial findings concerning Fig. 3.8.

First, they reported that neither the computed nor the observed dispersion curves exhibit a surface Rayleigh branch. Second, the pseudo charge model computations at $\bar{\Gamma}$ indicate the appearance of a "prominent" isotropic parabolic dispersion branch centered at 1.8 THz (7.4 meV). This branch ends in a V-shaped minimum at $q = 0.2 \text{ \AA}^{-1}$, which roughly equates to $2k_F$ of the Dirac fermion quasiparticles (DFQs), indicating the appearance of a significant Kohn anomaly. It displayed a strong Kohn anomaly with a V-shaped minimum at about $2k_F$. It is the surface-phonon branch that is located the lowest in $2k_F$.

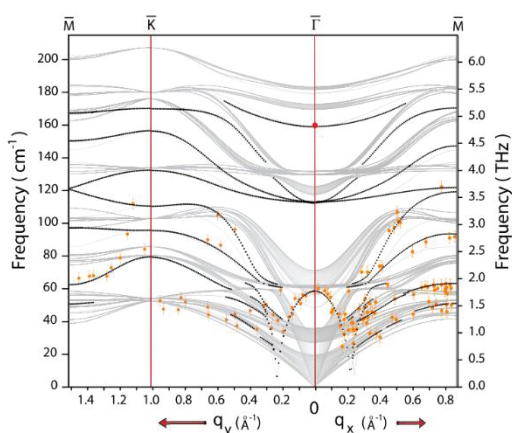


Figure 3.8: When surface Dirac fermions are taken into consideration, surface phonon dispersion curves along the $\bar{\Gamma} - \bar{M}$ and the $\bar{\Gamma} - \bar{K}$ high symmetry directions look like this: While the estimated surface dispersion curves are shown by black dots, the experimental data are displayed as orange dots with error bars that reflect the instrument resolution. The projection of the bulk bands onto the SBZ is shown by the gray region. Figure adapted from the ref. [60].

Later in 2012, the same group, Zhu *et al.* [61] carried out temperature dependent inelastic HAS measurements on the surface of Bi_2Se_3 at various temperatures in the range of 80–300 K. Sample was in situ cleaved along the c -axis (001). In order to evaluate EPC strength, EPC-induced phonon linewidths are required from the phonon measurements. Even for superconductors with significant coupling, phonon line broadenings brought on by EPC are typically modest. Because of the inherent instrument linewidths of a few meVs, such modest broadenings are exceedingly challenging to detect in both neutron and helium scattering experiments. As a result, it is more challenging to isolate EPC contributions from the measured phonon linewidth. In addition to EPC, phonon line broadening is also caused by other inherent factors such as phonon-phonon interaction (anharmonicity), phonon-defect

scattering, and phonon anticrossing with other branches. To retrieve the EPC, an indirect method was applied. The measured surface-phonon dispersion curve was first fitted with the real part of the phonon self-energy. Then, using a Hilbert (or Kramers-Kronig) transform, the imaginary part of self-energy and, consequently, the *el-ph* contribution to the phonon linewidth were determined.

Fig. 3.9 (a) and (b) for two samples show the temperature dependence of the particular branch's phonon mode. The phonon energy shows a very slight increase with temperature. As a result, a linear fit to the data has a very modest slope, which justifies ignoring the temperature dependency, especially when we consider an instrument resolution of approximately 1.5 meV. These findings showed that defects and anharmonicity contributions could be overlooked. They used the best-fit parameters obtained in ref. [60] and evaluated $\text{Re}\Sigma$ for the specific phonon branch at different wave vectors along the $\bar{\Gamma} - \bar{M}$ and high symmetry direction as shown in Fig. 3.9(c). Using the Kramers-Kronig transform [Equation (3.23)], they evaluated $\text{Im}\Sigma$, depicted in Fig. 3.9(d). The phonon linewidth (FWHM) for the specific branch is plotted in Fig. 3.9(e) along the $\bar{\Gamma} - \bar{M}$ high symmetry direction. After that EPC parameter depicted in Fig. 3.9(f), was evaluated using the equation,

$$\lambda_{\beta}(q) = \frac{1}{2\pi N(E_F)} \frac{\gamma_{\beta}(q)}{\hbar^2 \omega_{q,\beta}^2} \quad (3.24)$$

where $N(E_F)$ is the electronic density of states at E_F , and $\omega_{q,\beta}$ is the renormalized surface-phonon frequency for the β branch. They obtained an effective EPC parameter 0.43 for the specific branch, which is greater than previously reported EPC parameter values [57,58] from the ARPES measurements.

Recently in 2017, Tamtogl *et al.* [62] analyzed EPC and surface Debye Temperature on the surface of Bi_2Te_3 by means of temperature-dependent HAS measurement. The thermal attenuation in the diffraction of Helium atom from Bi_2Te_3 was studied in the temperature range between 110 and 335 K. The system shows a typical Debye-Waller behavior with a surface Debye temperature of $\Theta_D = (81 \pm 6)$ K.

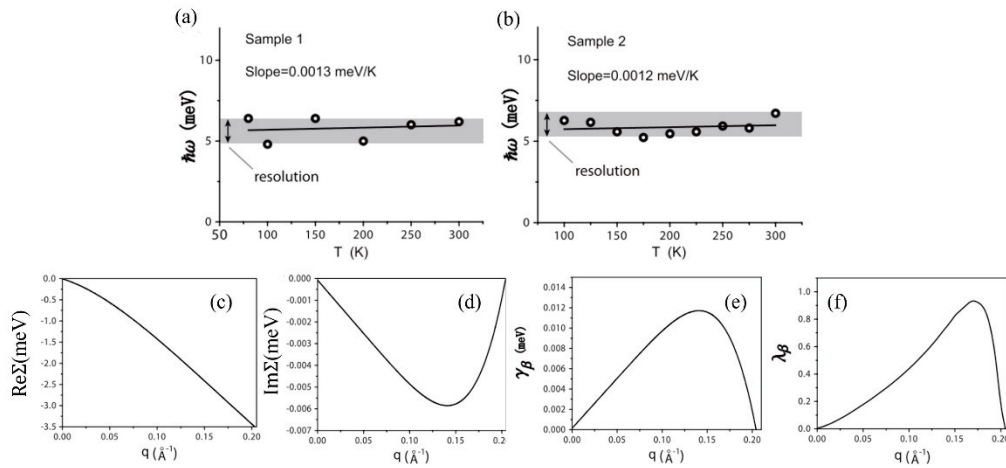


Figure 3.9: HAS measurement on the surface of Bi_2Se_3 . (a) and (b) The energy of a single phonon event as a function of temperature for Sample 1 for Sample 2, respectively. The solid line is a linear fit to the data, and the circles show experimental data. (c) and (d) depict the $\text{Re}\Sigma$ and $\text{Im}\Sigma$ for the isotropic phonon branch, respectively. (e) linewidth due to el - ph scattering. (f) Evaluated EPC parameter using linewidth in figure (f). The figures are adapted from ref.[61].

By adopting a recently developed quantum-theoretical derivation of the Helium scattering probabilities to the case of a degenerate semiconductor, they were able to extract the EPC strength from temperature-dependent Helium atom scattering measurements. Furthermore, the Debye-Waller attenuation, which is directly related to the EPC parameter λ_{ep} , allows them to extract a correctly averaged λ_{ep} for a given surface. Hence, they obtained the λ_{ep} in the range of 0.04–0.11 for Bi_2Te_3 for a charge-carrier density of the order of 10^{20} cm^{-3} .

3.3.3 Theoretical Studies on TIs

As our thesis work basically on the evaluation of EPI on the surface of Bi_2Te_3 TI. Therefore, in this section, we will briefly summarize the theoretical studies on Bi_2Te_3 . The first report came by Huang *et al.* in 2012; they did Density functional perturbation theory calculation in Bi_2Te_3 thin films, and calculated results shown in Fig. 3.10. By including SOC, they analyzed surface-phonon and EPI. In light of the predicted phonon DOS and partial phonon DOS, the shift in lattice dynamical behavior from bulk to the surface was explored. Their findings unequivocally demonstrate that surface phonon softening and stiffening coexist in Bi_2Te_3 ultrathin films. The computed magnitude of the EPC parameter was 0.05, which demonstrates that the EPI

in Bi₂Te₃ films is extremely weak, favoring its use for electronic devices that operate at ambient temperature.

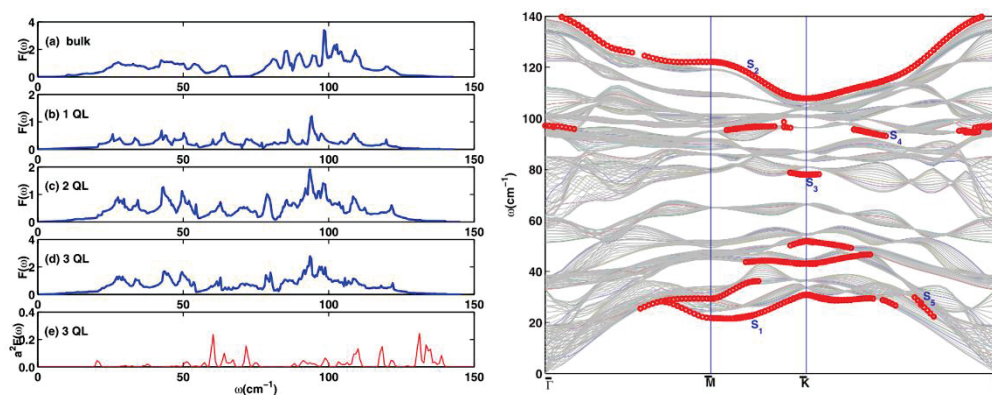


Figure 3.10: First principle calculation on Bi₂Te₃ thin films. (a) Phonon DOS $F(\omega)$ for Bulk and for varying thicknesses 1-3 QLs of Bi₂Te₃ (upper panels) and Eliashberg Function $\alpha^2 F(\omega)$ of 3 QLs Bi₂Te₃ thin film (bottom panel). (b) Red circles depicted the localized surface phonon modes of the 3 QLs Bi₂Te₃ thin film, and the gray area represents the project of bulk phonon dispersion onto the surface Brillouin zone. Figures adapted from ref.[63].

Recently R. Heid *et al.* [64] did ab initio calculation in the metallic surface states of prototype 3D TIs: Bi₂Se₃ and Bi₂Te₃. Fig. 3.11 (a) and (b) depict the calculated band structure of the Bi₂Se₃ and Bi₂Te₃, respectively. Fig. 3.11 (c) and (d) represent the evaluated EPC parameters for the upper and lower cone of both TIs. According to their observation, the EPC parameter weakly depends on the chosen initial electron energy states, and this initial energy-dependent EPC parameter also has some correlation with DOS (shown by dashed line); for example, in the case of Bi₂Te₃, the magnitude of EPC parameter increased closed to DP, because DOS is enhanced, (the VB surrounds DP, so the number of scattering channels are enhanced that's why EPC parameter is enhanced) as shown in the Fig. 3.11(d). On the other hand, the EPC parameter reached at its minimum around 100 meV above the DP, as shown in Fig. 3.11 (d), where DOS also reached its minimum. They discovered a typical linear relationship of the coupling strength on the energy of the quasiparticle as well as a reduction brought on by doping into bulk states. They suggested that both of these characteristics might help to explain why earlier experiments provide a wider range of values for the EPC parameter, despite the fact that findings more significant than 0.2 are incompatible with intrinsic EPI. Their finding neither support the previously reported Kohn anomalies nor the strong mode coupling with the frequency well above

the bulk phonon spectrum. They reported that the intrinsic EPC in the TSSs of 3D TIs is the order of 0.1, which is very small and good enough to support these materials for RT applications.

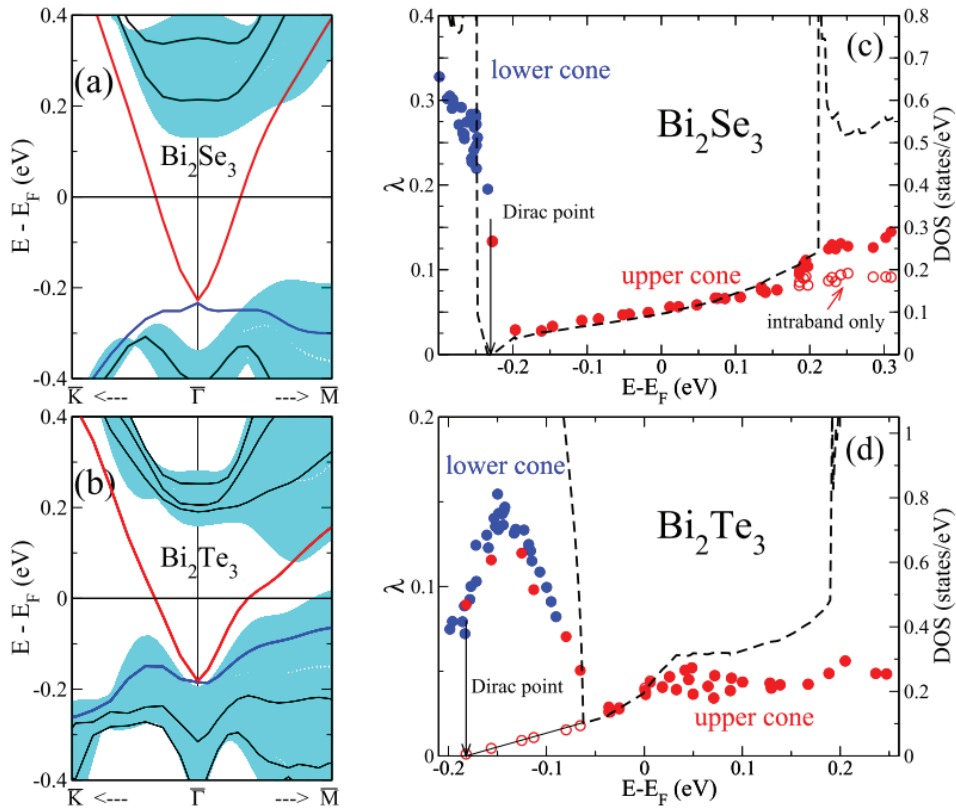


Figure 3.11: Band structure calculations of 3 QLs Bi_2Se_3 (a) and 3 QLs Bi_2Te_3 , respectively. The shaded area represents the surface projected bulk states. (c) and (d) depicts the initial energy-dependent magnitude of EPC parameters for Bi_2Se_3 and Bi_2Te_3 , respectively. Solid red circles denote the EPC parameter for the upper Dirac cone and Blue solid circles for the lower Dirac cone. Open red circles denote the intraband contribution for the upper part of the cone, *i.e.*, without coupling to the first bulk-like CB. The dashed line represents the DOS. Figures adapted from ref. [64].

Chapter 4: Many-Body Interaction on the Surface of Bi₂Te₃ Crystals

The Bi₂Te₃ has been known for a long time as a narrow bandgap semiconductor and rigorously studied as a thermoelectric material [65]. Since the discovery of Bi₂Te₃ as a nontrivial TI in 2009, it has attracted much interest in the past decade [2,7,14,16,66]. As we explained in chapter 1, the electron spin and momentum directions of the TSSs are locked due to the strong SOC, yielding a peculiar helical spin texture in the momentum space [1,11], and this helical spin texture of the TSSs suppresses electron backscattering due to lattice defects or nonmagnetic impurities [31,32], leading to a prolonged quasiparticle lifetime and enhanced electrical conductivity and mobility. However, it is only true in the non-interacting quasiparticle case but does not guarantee in the case of interacting quasiparticle picture. Since many intensive efforts have been applied to revealing the interacting quasiparticle picture in the TSSs of prototypical 3D TIs, Bi₂Se₃, and Bi₂Te₃. According to previous studies, the EPI is the dominant interaction over other interactions in the TIs and plays a significant role at elevated temperatures. This chapter is mainly devoted to the EPI on the surface of Bi₂Te₃ crystals using a High-resolution Laser-based ARPES experiment.

4.1 Introduction

The three-dimensional (3D) TIs, a new quantum state of matter under strong SOC and TRS, have attracted much interest in the past decade [2,7,14,16,66]. Metallic TSSs inside the bulk bandgap of 3D TIs degenerate at the TRIM and exhibit a Dirac-fermion-like linear dispersion away from the TRIM [2]. The electron spin and momentum directions of the TSSs are locked due to the strong SOC, yielding a peculiar helical spin texture in momentum space [1,11]. The helical spin texture of the TSSs suppresses backscattering due to lattice defects or nonmagnetic impurities [31,32], leading to a prolonged quasiparticle lifetime and enhanced electrical conductivity and mobility. The metallic nature of the TSSs is robust under perturbations that conserve the topological numbers, which is determined by the symmetry properties of the band structures under the SOC [1,2]. The 3D TIs have attracted much interest not only for their intriguing physical properties, such as the QSHE [6], QAHE [34], Majorana fermions in the superconducting state [35,36], and magnetic monopole [37], but also for their potential spintronic applications [33].

Based on Fermi liquid theory, the transport properties at finite temperature are directly related to the quasiparticle properties near the E_F [67]. Depending on the magnitudes of the many-body interactions, such as the EPI and electron-electron interaction (EEI), the effective mass of electrons is enhanced, and the lifetime of the quasiparticle varies [67]. The quasiparticle properties at finite temperature can be formulated by using a single-particle thermal Green's function, which includes a self-energy (Σ) incorporating the EPI and EEI [67-69]. The $\text{Im}\Sigma$ is directly related to a reciprocal of the relaxation time ($1/\tau$) at a given electron momentum and energy, and the average value at the Fermi surface is proportional to the electrical conductivity and mobility, which are essential parameters for electronic applications. In particular, the EPI plays a significant role in the transport properties at a finite temperature [67,68] and temperature-dependent reduction of the bandgap [70,71]. Therefore, quantifying many-body interactions is essential to understanding the transport and magnetic properties derived from the TSSs on the 3D TIs from the microscopic viewpoint.

To date, intensive efforts have been applied to revealing the EPI in the TSSs of prototypical 3D TIs, Bi_2Se_3 , and Bi_2Te_3 . Despite the expected suppression of backscattering in the TSSs [72], the transport measurements on Bi_2Se_3 suggested signatures of scattering due to the EPI [73,74]. To directly probe the surface phonons on Bi_2Se_3 and Bi_2Te_3 , HAS¹ measurements have been performed [60-62,75-77]. Early experiments indicated a strong Kohn anomaly [60] and an EPI coupling parameter of $\lambda_{\text{ep}} \sim 0.43$ [23] for Bi_2Se_3 and an average branch-specific EPI coupling parameter of $\langle \lambda_{\text{ep}} \rangle \sim 1.44$ for Bi_2Te_3 [75,76]. However, a recent HAS investigation revealed a significant Rayleigh mode within the low energy region (<10 meV), no Kohn anomaly, and a lower EPI coupling parameter of $\lambda_{\text{ep}} \sim 0.23$ for Bi_2Se_3 [25]. For Bi_2Te_3 , the EPI coupling parameter was in the range of $\lambda_{\text{ep}} = 0.04-0.11$ and depended on the carrier concentration [62]. While the EPI coupling parameter for some phonon branches may be high, the average over all modes is lower [62].

High-resolution ARPES is a powerful tool for investigating quasiparticle properties because the ARPES spectrum corresponds to the imaginary part of the single-particle Green's function [54,78]. Temperature-dependent high-resolution

¹ In HAS experiment, the intense, nearly monochromatic helium beam is then projected towards a target surface at a specific angle of incidence, and the scattered intensity is measured using a mass spectrometer, which contains all the information about the surface structure and lattice dynamics.

ARPES measurements revealed EPI coupling parameters of $\lambda_{ep} \sim 0.25$ [57] and $\lambda_{ep} \sim 0.076-0.088$ [58] for Bi₂Se₃ and $\lambda_{ep} \sim 0.17$ [79] for Bi₂Te₃. High-resolution ARPES measurements on Bi₂Se₃ and Bi₂Te₃ further revealed a kink structure at low temperature due to the EPI in the band dispersion of the TSS [41,59]. Kondo *et al.* [59] observed an extremely large coupling parameter of $\lambda_{ep} \sim 3$ within the energy range of ~ 3 meV measured from the E_F , which was justified from the viewpoint of coupling to spin plasmons with an energy of 2.2 meV [80] and the Kohn anomaly of the surface phonon mode [60]. On the other hand, Chen *et al.* found that the coupling parameters were $\lambda_{ep} \sim 0.17$ for Bi₂Se₃ and $\lambda_{ep} \sim 0.19$ for *n*-type Bi₂Te₃ [41]. They also found that the EPI coupling parameter depended on the E_F position from $\lambda_{ep} \sim 0$ (*p*-type Bi₂Te₃) up to 0.19 (*n*-type Bi₂Te₃) [41].

Model calculations indicated that the electrical resistivity was linearly dependent on the temperature at the elevated temperatures, yielding an EPI coupling parameter of $\lambda_{ep} = 0.42$ [81,82]; that the magnitude of the coupling parameter was dependent on the carrier concentration and temperature [83]; and that the EPI between the Dirac electrons and Rayleigh phonon mode was weak, yielding a small coupling parameter of $\lambda_{ep} \sim 0.01$ [84]. An earlier first-principles calculation gave an EPI coupling parameter of $\lambda_{ep} \sim 0.05$ for Bi₂Te₃ [63]. Later, more extensive first-principles calculations were performed; the EPI coupling parameters were $\lambda_{ep} < 0.15$ for Bi₂Se₃ and Bi₂Te₃, and the value of λ_{ep} varied depending on the initial-state electron energy [64].

4.2 Motivation

Till now, the seemingly conflicting values of the EPI coupling parameters have been discussed in several studies [62,64,76]. One of the essential points of discussion is the position of chemical potential or carrier density of the TSSs [41,62,64,83]. The kink structure observed by the ARPES measurements exists within the Debye energy range near E_F [85]. While the EPI coupling parameter can be evaluated based on the magnitude of the kink, the ability to evaluate this parameter is limited at the E_F and Fermi wavenumber, which further vary depending on temperatures. Therefore, samples with different doping levels (varying chemical potential) should be prepared to examine the doping dependence of the EPI coupling parameter based on the kink structure [41]. On the other hand, the initial-state electron energy dependence of the

EPI coupling parameter can be evaluated by means of the temperature-dependent linewidth of the ARPES spectra. However, the potential chemical position concerning the DP in Bi₂Se₃ was reported to change with increasing temperature [57,58], and was not explicitly considered in the evaluation of the EPI coupling parameter [58]. For Bi₂Te₃, detailed temperature-dependent ARPES measurements have not been reported thus far. Therefore, in the coming section, I will focus on the evaluation of EPI using the temperature-dependent ARPES measurement.

4.3 A short Discussion on the Evolution of Coupling Parameter

An ARPES spectrum corresponds to a single-particle spectral function, $A(\vec{k}, \omega)$ [54,68,86], given by

$$A(\vec{k}, \omega) = -\frac{1}{\pi} \frac{\text{Im}\Sigma(\vec{k}, \omega)}{[\omega - \omega_k^0 - \text{Re}\Sigma(\vec{k}, \omega)]^2 + [\text{Im}\Sigma(\vec{k}, \omega)]^2} \quad (4.1)$$

Here, $\text{Re}\Sigma(\vec{k}, \omega)$ and $\text{Im}\Sigma(\vec{k}, \omega)$ are the real and imaginary parts of the self-energy, respectively, and ω_k^0 is the energy for the noninteracting band measured from the E_F . Assuming the noninteracting band dispersion is linear, $\omega_k^0 = \hbar v_F(k - k_F)$, where v_F is the Fermi velocity, and the spectral function as a function of momentum k for the fixed ω becomes

$$A(\vec{k}, \omega) = -\frac{1}{\pi} \frac{1}{\hbar v_F} \frac{\frac{\text{Im}\Sigma(\vec{k}, \omega)}{\hbar v_F}}{\left[k - k_F - \frac{\omega - \text{Re}\Sigma(\vec{k}, \omega)}{\hbar v_F}\right]^2 + \left[\frac{\text{Im}\Sigma(\vec{k}, \omega)}{\hbar v_F}\right]^2} \quad (4.2)$$

If the momentum dependence of the self-energy is negligible ($\text{Im}\Sigma(\vec{k}, \omega) \sim \text{Im}\Sigma(\omega)$), namely, the interaction is local, the spectral function as a function of k becomes a Lorentzian function. Indeed, the experimental MDC is well reproduced by a Lorentzian function, confirming the validity of the present assumptions. Then, the full-width-half-maxima (FWHM) of the MDC peak, Δk , is directly connected to the imaginary part of the self-energy by $\Delta k = 2|\text{Im}\Sigma(\omega)/\hbar v_F|$. The imaginary part of the self-energy is connected to the linewidth broadening by $\Gamma(\omega) = 2|\text{Im}\Sigma(\omega)| = \hbar/\tau$, where τ is the lifetime. Thus, the linewidth at fixed ω can be evaluated based on the MDC width Δk and the group velocity of the noninteracting

band v_F . If the magnitude of the self-energy is small enough, the quasiparticle scattering rate can be directly evaluated from the peak width, $\Delta\varepsilon$, of the energy distribution curve (EDC) at fixed k , namely, $\Gamma(\omega) = 2|\text{Im}\Sigma(\omega)| = \Delta\varepsilon$. If the noninteraction band is given, the self-energy is directly obtained based on the measured peak positions and line widths. The advantage of the ARPES lineshape analyses is that we can determine the self-energy due to the many-body interactions in wide energy and momentum ranges at given temperatures. This allows us to distinguish each magnitude of the electron-phonon and electron-electron interactions.

There are two methods to determine the EPI coupling parameter based on the ARPES lineshape analyses. One method is to analyze the kink structure or reduction in the group velocity due to the EPI near the E_F at low temperature. The group velocity of the energy band is reduced by a factor of $1/(1 + \lambda_{ep})$, where λ_{ep} is the EPI coupling parameter. At finite temperatures, the self-energy due to the EPI ($\Sigma_{ep}(\vec{k}, \omega; T)$) is represented by the thermal Green's function [68]. Therefore, the coupling parameter determined by the gradient of the real part of the self-energy at E_F ,

$$\lambda_{ep}(T) = - \left. \frac{\partial \text{Re}\Sigma_{ep}(\vec{k}, \omega; T)}{\partial \omega} \right|_{\omega=E_F} \quad (4.3)$$

should be temperature dependent [54,58,68,86,87]. Note that the magnitude of λ_{ep} decreases as the temperature increases [68,86].

The other method for determining the EPI coupling parameter is to use the slope of the temperature dependence of the self-energy $|\text{Im}\Sigma_{ep}(\vec{k}, \omega; T)|$ at an initial-state electron energy ω measured from the E_F with a momentum \vec{k} [41,54,57-59,68,86]. The ARPES linewidth due to the EPI interaction at ω and \vec{k} is given by

$$\begin{aligned} \Gamma_{ep}(\vec{k}, \omega; T) &= 2|\text{Im}\Sigma_{ep}(\vec{k}, \omega; T)| \\ &= \pi \int_0^{\omega_D} d\tilde{\omega} \alpha^2 F(\vec{k}, \omega; \tilde{\omega}) [1 + f(\omega + \tilde{\omega}, T) \\ &\quad - f(\omega - \tilde{\omega}, T) + 2n(\tilde{\omega}, T)], \end{aligned} \quad (4.4)$$

where $n(\nu, T)$ is the Bose-Einstein function, $f(\nu, T)$ is the Fermi-Dirac distribution function, and ω_D is the Debye energy [64,68]. The function $\alpha^2 F(\vec{k}, \omega; \tilde{\omega})$ is defined by

$$\alpha^2 F(\vec{k}, \omega; \tilde{\omega}) = \sum_f \delta(\omega - \omega_f \pm \tilde{\omega}) \sum_{\vec{q}, \nu} |g^{i,f}(\vec{k}; \vec{q}, \nu)|^2 \delta(\tilde{\omega} - \omega_{\vec{q}, \nu}) \quad (4.5)$$

where \vec{q} and ν represent the phonon momentum and phonon mode, respectively; $\omega_{\vec{q}, \nu}$ is the phonon energy with \vec{q}, ν ; and $g^{i,f}(\vec{k}; \vec{q}, \nu)$ is the matrix element of the electron-phonon scattering from the initial-state electron with \vec{k} and ω to the final-state electron with momentum $\vec{k} + \vec{q}$ and energy ω_f [64]. At elevated temperatures, $\omega > k_B T > \omega_D \geq \tilde{\omega} \geq 0$, the temperature dependence of the linewidth can be approximated by

$$\Gamma_{ep}(\vec{k}, \omega; T) \sim 2\pi \int_0^{\omega_D} \alpha^2 F(\vec{k}, \omega; \tilde{\omega}) d\tilde{\omega} - 2\pi \cdot 2 \int_0^{\omega_D} \frac{\alpha^2 F(\vec{k}, \omega; \tilde{\omega})}{\tilde{\omega}} d\tilde{\omega} \cdot \quad (4.6)$$

$$k_B T = C - 2\pi \lambda_{ep}(\vec{k}, \omega) k_B T,$$

where C is a constant and

$$\lambda_{ep}(\vec{k}, \omega) = 2 \int_0^{\omega_D} \frac{\alpha^2 F(\vec{k}, \omega; \tilde{\omega})}{\tilde{\omega}} d\tilde{\omega} \quad (4.7)$$

is the EPI coupling parameter at zero temperature at the initial electronic state with ω and \vec{k} . Therefore, the EPI coupling parameter $\lambda_{ep}(\vec{k}, \omega)$ can be calculated from the slope of the temperature-dependent ARPES linewidth $\Gamma_{ep}(\vec{k}, \omega; T)$. When the electron-phonon matrix element is weakly dependent on the initial-state electron energy and the electron-phonon scattering can be regarded as nearly elastic, namely, $\omega \sim \omega_f$, assuming that $|\omega_D/\omega| \ll 1$, we may have the relation

$$\alpha^2 F(\vec{k}, \omega; \tilde{\omega}) \sim D(\omega) \sum_{\vec{q}, \nu} |g^{i,f}(\vec{k}; \vec{q}, \nu)|^2 \delta(\tilde{\omega} - \omega_{\vec{q}, \nu}), \quad (4.8)$$

where $D(\omega) = \sum_f \delta(\omega - \omega_f)$ is the density of states (DOS) at ω . In this case, the magnitude of $\alpha^2 F(\vec{k}, \omega; \tilde{\omega})$ as well as $\lambda_{ep}(\vec{k}, \omega)$ is proportional to $D(\omega)$ [54,64], which is indeed what we observe in this study.

4.4 Results and Discussion

4.4.1 Low Energy Kink Structure

Figs. 4.1 (a) and 4.1(d) show the ARPES result, exhibiting a Dirac cone-like band dispersion of the TSSs along the $\bar{\Gamma} - \bar{K}$ momentum direction and the FS, respectively, which agrees well with previous reports [41]. In Figs. 4.1(a), the CB exists near E_F around the $\bar{\Gamma}$ point, indicating that the present sample is an n -type semiconductor. The ARPES spectral features above the DP are more homogeneous

and narrower for the $k_{//} < 0$ side than for the $k_{//} > 0$ side, as seen in Fig. 4.1(b). The difference is likely due to the matrix element effect of the dipole transition, which depends on the experimental geometry and excitation photon energy [45]. Here, we examine the MDCs for the $k_{//} < 0$ side and above the DP energy (E_D) and analyse the peak position by fitting to a Lorentzian function.

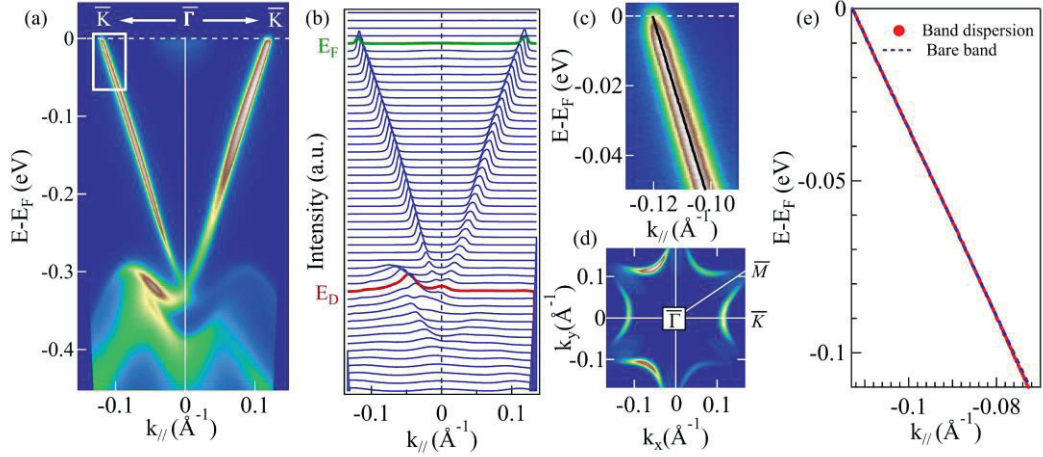


Figure 4.1: ARPES map (a) ARPES intensity plot of Bi₂Te₃ measured along $\bar{\Gamma}-\bar{K}$ at $h\nu=6.3$ eV and at 17 K. (b) MDCs of Bi₂Te₃ along the $\bar{\Gamma}-\bar{K}$ momentum direction. The MDCs at E_F and DP (E_D) are shown in green and red, respectively. (c) Magnified view of the ARPES intensity plot of the rectangle region in figure 4.1 (a). The solid black line represents peak positions obtained from MDC analyses. (d) Observed FS at 17 K. (e) Red circles indicate peak positions determined by the MDC analyses. To see the linearity, we plotted a blue dotted line connecting a band point at E_F and a band point at -100 meV.

Fig. 4.1(c) shows a magnified view of the ARPES intensity plot corresponding to the rectangle region in Fig. 4.1(a) together with band points obtained from the MDC peak analyses. As the surface Debye temperature of Bi₂Te₃ was reported to be $\Theta_D = 82 \pm 6$ K ($k_B\Theta_D \sim 7$ meV) [62], the kink structure should exist within this energy range near E_F [85]. The solid red circles in Fig. 4.1(e) show the band points obtained from the MDC analyses, and they are on a blue dashed line connecting two points, one at E_F and another at -100 meV. This indicates that there is no appreciable kink structure in the energy band dispersion at 17 K.

4.4.2 Effect of Temperature on the ARPES Band Dispersion

As we did not find kink at low temperature. Next, we examine the temperature dependence of the imaginary part of the self-energy to evaluate the EPI coupling parameter as a function of the initial-state electron energy along the $\bar{\Gamma} - \bar{K}$ momentum

direction. In the temperature-dependent measurements, we should pay special attention to the adsorption of the residual gas molecules in the ARPES measurement system because it may significantly modify the DP energy (E_D) position [88,89]. Therefore, we carefully check the stability of the ARPES spectral features and the reproducibility of the DP energy (E_D) after the heating and cooling processes and confirm that the present evaluations are intrinsic.

Fig. 4.2 shows the ARPES intensity plots (lower panel) and FS (upper panel) at various temperatures. The ARPES spectral features after cleavage are highly stable in ultrahigh vacuum, and we do not detect a DP energy (E_D) shift or linewidth broadening over time at 17 K in Fig. 4.2(a). Then, we perform ARPES from 17 K to 300 K. One can see in the Fig. 4.2 (b) and (c), that the DP and bulk valence bands are shifted upwards with increasing temperature. The bulk band and TSS energies vary with temperature, as evident from the DP energy; E_D is ~ 320 meV at 17 K [see Fig. 4.2(a)] to 256 meV at 300 K [Fig. 4.2(c)], implying that the TSSs carrier density decreases as temperature increases. We cool the sample to 17 K after 58 hrs of cleaving and obtain an ARPES spectrum, as shown in Fig. 4.2(d). Even after the heating and cooling cycle, the ARPES linewidth and the DP energy ($E_D \sim 321$ meV) at 17 K are highly reproducible. In Fig. 4.2 (upper panels), we can see a reduction in the Fermi Surface area and the Fermi wave vector (k_F) with increasing temperature because the whole bands are shifting upwards. In addition, the bulk CB is centered at the $\bar{\Gamma}$ point, as indicated by the arrows in the upper panels of Fig. 4.2.

To confirm the reproducibility of the sample, we have measured another crystal of Bi_2Te_3 . We cleaved sample #2 below 20 K then heated up to RT and measured from RT to 17 K (cooling cycle). ARPES intensity plot of sample #2 is shown in Fig. 4.3(a) at 17 K, exhibiting an E_D of ~ 327 meV is almost identical to those of sample #1. In addition, one can see in the Fig. 4.4, the MDC peak widths and $\text{Im}\Sigma$ of both samples are also almost identical. Fig. 4.3(b) shows that the temperature dependence of the E_D in the heating process of sample #1 and that in the cooling process of sample #2 are almost the same, confirming the reproducibility of these observations.

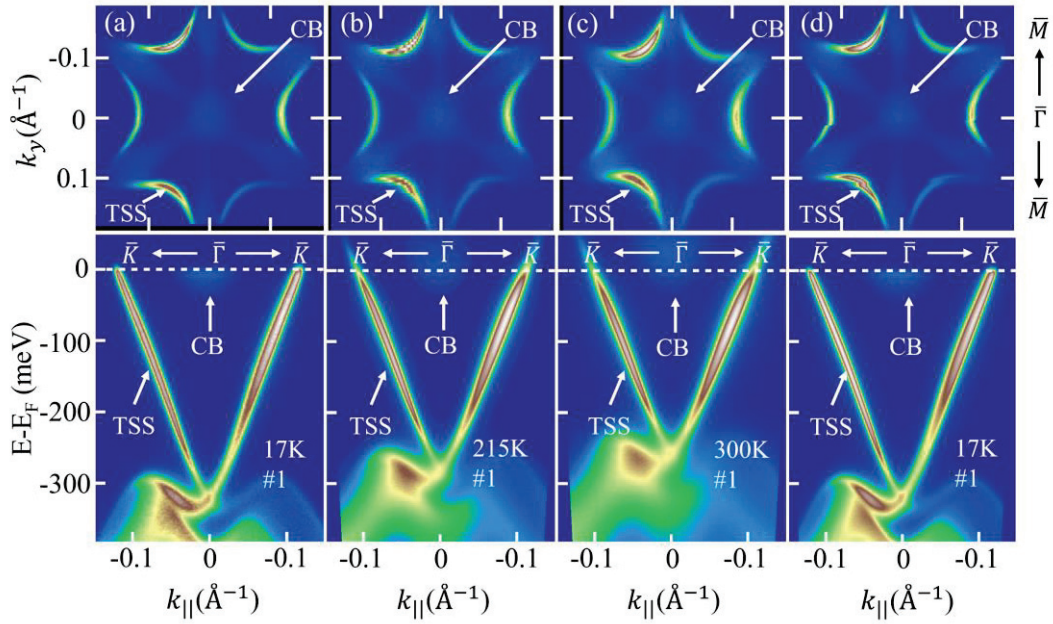


Figure 4.2: ARPES map. (a) to (d) APRES results from Bi₂Te₃ at various temperatures, showing the FS (upper panels) and band dispersion along the $\bar{\Gamma}$ - \bar{K} momentum direction (lower panels). Measurements were taken at (a) 17 K, (b) 215 K, and (c) 300 K in the heating process. (d) ARPES result taken at 17 K after RT measurement and re-cooling. The arrows mark the TSS and CB in the figure.

Although we did not move the sample during temperature-dependent measurements, we noticed that the sample position changed slightly as the temperature changed, probably due to the expansion or shrinkage of the manipulator. Therefore, we performed FS mapping as we changed the temperature and obtained ARPES spectra precisely at the $\bar{\Gamma}$ point at each temperature up to RT. The Fig. 4.5 (a) and (b) depict the constant energy contour of Bi₂Te₃ measured at two temperatures: 17 K and at 300 K, respectively. Here, E_D represents the DP energy, and the energy is referred to as E_F . The E_D values are 320 meV and 255 meV at 17 K and 300 K, respectively.

Fig. 4.6(a) shows the EDCs of sample #1 at the $\bar{\Gamma}$ point at 17 K and at 300 K. The DP peak and the VB peak are shifted upwards closer to E_F as the temperature increases. Recently, Nayak *et al.* reported a similar temperature dependence in the TSS on Bi₂Te₂Se [90] and explained this phenomenon through the temperature-dependent

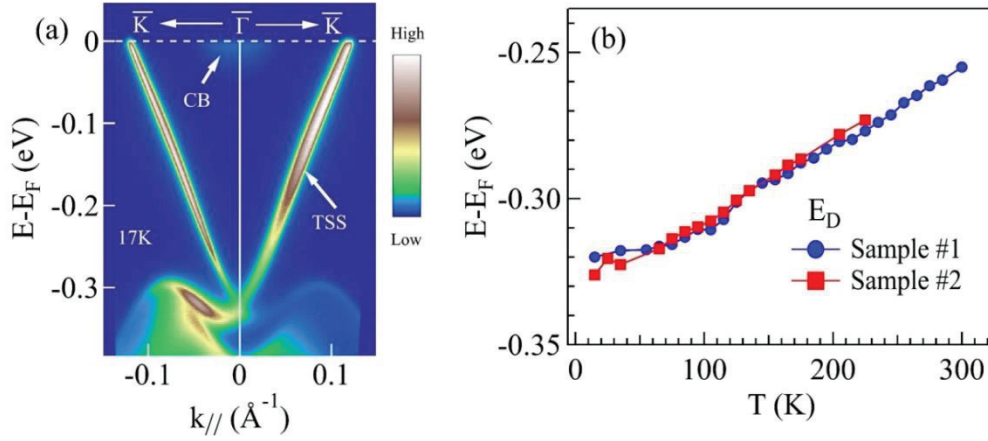


Figure 4.3: ARPES intensity map. (a) Band dispersion of sample #2 at 17 K. (b) Temperature-induced energy shift in the E_D . The DP energy (E_D) of sample #1 was determined in the heating process from 17 K to 300 K and that of sample #2 in the cooling process from 300 K to 17 K.

chemical potential shift [72]. To examine the temperature dependence of the energy position for the CB and VB in more detail, we analyze the EDCs and evaluate the energies for the VB peak (E_{VBP}) and CB bottom (E_{CBB}) positions at the $\bar{\Gamma}$ point in the lower panel of Fig. 4.6(b). As we cannot identify the CB peak at lower temperatures due to the Fermi edge, we estimate the zero-point crossing energy (E_{CBB}) of the tangent line of the CB spectral feature. In Fig. 4.6(b), E_{VBP} increases as temperature increases, while E_{CBB} is almost constant over temperature. As a result, the energy difference ($\Delta E_1 = E_{CBB} - E_{VBP}$) between VB and CB decreases as the temperature increases, which is consistent with the ubiquitous bandgap reduction with increasing temperature in semiconductors [70,91]. The temperature-dependent energy shift or reduction in the bandgap is formulated by

$$\Delta E(\vec{k}, \omega; T) = \int_0^{\omega_D} d\tilde{\omega} \alpha^2 F(\vec{k}, \omega; \tilde{\omega}) [n(\tilde{\omega}, T) + \frac{1}{2}]. \quad (4.9)$$

Note that at high temperatures where $k_B T > k_B \Theta_D = \omega_D$ or large electron excitation energies where $|\omega_D/\omega| \ll 1$, the right-hand side becomes identical to $\frac{1}{\pi} |\text{Im}\Sigma_{ep}(\vec{k}, \omega; T)|$ because we obtain the relation $1 + f(\omega + \tilde{\omega}, T) - f(\omega - \tilde{\omega}, T) \sim 1/2$. Indeed, ΔE_1 and $|\text{Im}\Sigma_{ep}(\vec{k}, \omega; T)|$ show a linear correlation in Fig. 4.6(e), confirming that the temperature dependence of the energy gap in the bulk is derived from the EPI.

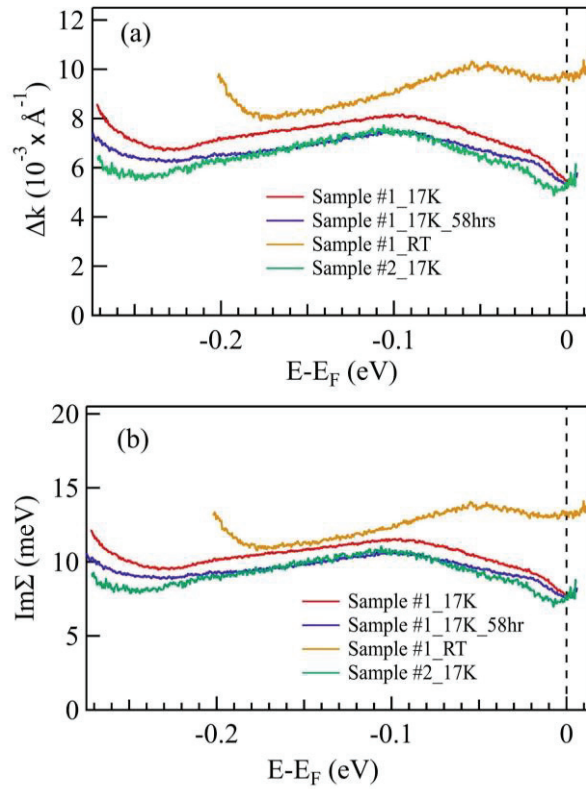


Figure: 4.4: Effect of temperature on TSSs peak width and $-\text{Im}\Sigma(\omega, T)$ of Bi₂Te₃ crystals along $\bar{\Gamma}-\bar{K}$ direction. (a) and (b) illustrates energy-dependent FWHM and the $-\text{Im}\Sigma(\omega, T)$ extracted from MDCs fit by Lorentzian peaks, respectively. Red lines represent sample #1 at 17 K measured after 2 hrs of cleave; after that same sample was measured at various temperatures up to RT continuously, and yellow lines of sample #1 at 300 K. After that sample was further cooled down to low temperature, and band dispersion was measured again at 17 K after 58 hrs of cleave, as FWHM and the $-\text{Im}\Sigma(0, T)$ shown by blue lines. Green lines represent FWHM and the $-\text{Im}\Sigma(0, T)$ of sample #2 at 17 K, showing similarity with sample #1. The magnitude of FWHM and the $-\text{Im}\Sigma(0, T)$ are very small. Furthermore, as we found, the band dispersion and the $\text{Re}\Sigma$ have no discernible kink structure, implying that electron-phonon coupling is negligible. The intrinsic scattering rate for the electron in the TSSs is relatively tiny, as evidenced by these results (small magnitude of $\text{Im}\Sigma$ and no kink structure in the $\text{Re}\Sigma$) [92].

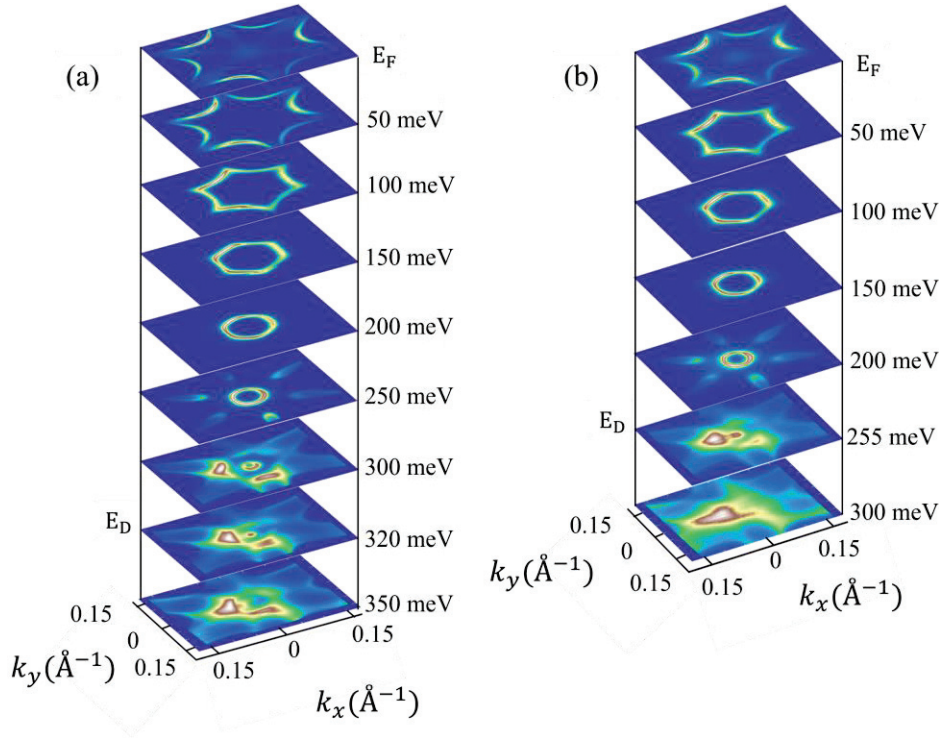


Figure 4.5: ARPES tilt mapping. (a) Constant energy contours of the Bi_2Te_3 at 17 K were measured after cleavage. (b) Constant energy contours at 300 K in the heating process.

We mention the temperature dependence of the chemical potential shift represented by

$$\mu(T) = E_F - \frac{\pi D'(E_F)}{6 D(E_F)} (k_B T)^2, \quad (4.10)$$

where $E_F = \mu(0)$ is the Fermi level, $D(E_F)$ is the DOS at the E_F , and $D'(E_F)$ is the gradient of the DOS at the E_F [72,90]. If the E_F is closer to the CB bottom, as in the present case, the gradient of the DOS is positive; $D'(E_F) > 0$. The chemical potential decreases as temperature increases, which causes the CB and VB peaks to shift with the same amount of energy towards higher energy. However, this is not what we observe in Fig. 4.6(b), indicating the significant role of the EPI.

As the energy gap at the $\bar{\Gamma}$ point (ΔE_1) decreases as temperature increases, the temperature-dependent band modification is obviously not rigid-band-like. Thus, we examine the temperature dependence of the band dispersion of the TSS in more detail. In Fig. 4.6(c), we plot the temperature dependence of the wavenumber (k) and the group velocity (v) at the initial-state electron energy at 100 meV above the DP and along the $\bar{\Gamma} - \bar{K}$ momentum direction. We can clearly see an increase in k and decrease

in (v) as temperature increases. This indicates that the band dispersion of the TSS is compressed along the energy direction, as the energy gap in the bulk decreases as temperature increases. Fig.4.6(f) shows a schematic diagram of temperature-dependent non-rigid-band-like band modification observed in this study.

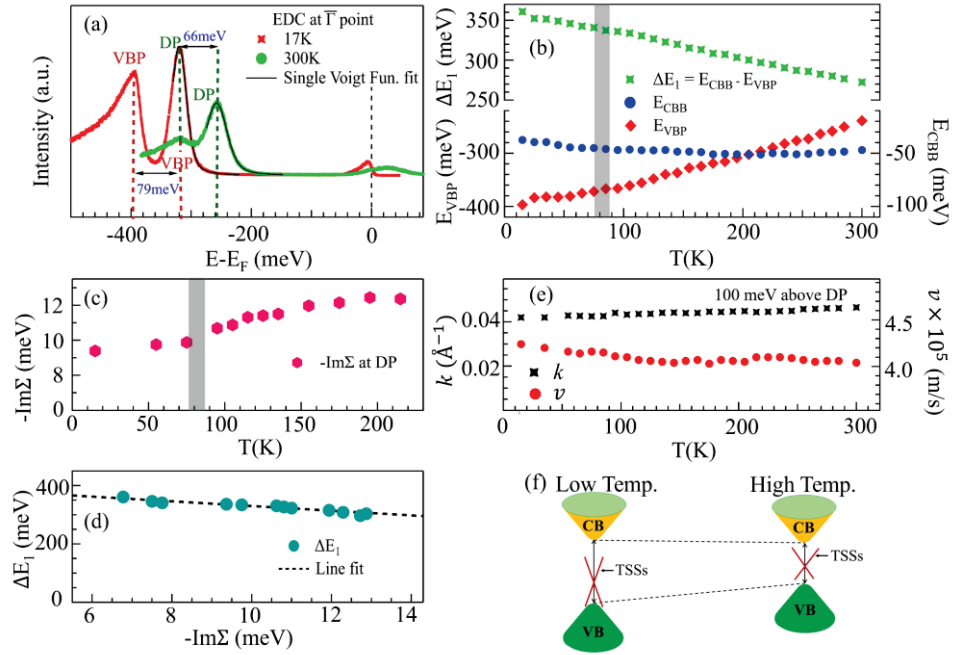


Figure 4.6: Effect of temperature on bulk and surface bands. (a) EDCs of sample #1 at the $\bar{\Gamma}$ point at 17 K (red) and 300 K (green). Solid black lines show the fitting results using a single peak Voigt function. (b) The lower panel depicts the energy position of the VB peak (E_{VBP}) and CB bottom (E_{CBB}). The upper panel shows the temperature dependence of the energy difference $\Delta E_1(T) = E_{CBB}(T) - E_{VBP}(T)$ at the $\bar{\Gamma}$ point. (c) The temperature-dependent $|\text{Im}\Sigma(|\vec{k}| = 0, \omega = E_D; T)|$ at the DP obtained from EDC line widths. The grey shaded areas in (b) and (c) show the reported surface Debye temperature [62]. (d) Plot of $\Delta E_1(T)$ as a function of $-\text{Im}\Sigma(0, E_D; T)$ with a line fit. (e) Temperature dependence of the wave vector (k) and the group velocity (v) at fixed energy (100 meV above the DP). (f) Schematic diagram of effect of temperature on surface and bulk bands.

Despite the nontrivial temperature-dependent band modification, we cannot detect an appreciable gap opening at the DP. Fig. 4.6(a) shows the fitting results of the EDCs at 17 K and 300 K using a single Voigt function. This confirms that the TSS is robust against bulk band modification in the presence of the EPI, which is consistent with topological protection [2].

4.4.3 Effect of Adsorption/Desorption of Residual Gas Molecules on the TSSs

As we have did long-time measurement, therefore TSSs are known to be altered by the adsorption/desorption of residual gas molecules in ultrahigh vacuum chambers [88]. If residual gas molecules act as electron donors, adsorption results in downwards band bending (shifts to lower energy) of the TSSs on the 3D TIs [93,94]. A strong band bending induced by adsorbed surface atoms may quantize the bulk CBs and VBs [95,96]. In fact, the surface state modification is sensitive to intrinsic parameters such as the sticking coefficient of the sample surface and extrinsic parameters such as the vacuum of the measurement chamber, time constant of surface modification, photon flux, and photon energy [88,97-99].

In this study, we ran ARPES experiments only under ultrahigh vacuum conditions of 2.4×10^{-9} Pa, which was one order of magnitude better than those of the measurements reported in refs. [88,94]. The residual gas analyses of our chamber using mass spectrometer showed that the main residual gas molecules were hydrogen molecules, which is always the case for any ultrahigh vacuum chamber.

We started our temperature-dependent measurement almost more than two hours after cleaving (we first performed FS mapping to confirm the $\bar{\Gamma}$ point). We did not observe any noticeable shift of the E_D during long-term measurement using laser energy of 6.3 eV at 17 K. However, we could not completely exclude an energy shift due to H_2 molecule adsorption. We observed a sudden change in the lifetime in the range of approximately 160-180 K in the heating process, which did not occur in the cooling process (see Figs. 4.7, 4.9, and 4.10). This might be correlated with the desorption threshold temperature of H_2 molecules on the sample surface [100,101]. However, apart from this narrow temperature range of 160-180 K, the temperature dependence of the lifetime was highly reproducible in the heating and cooling processes. It should be noted that there was no such anomalous behavior in the E_D for the heating and cooling processes, as shown in Fig. 4.3(b). This result suggests that there was no significant charge transfer for adsorption and desorption of the residual gas. Therefore, the value of the EPI coupling parameter we evaluated was robust.

Previously, the temperature-dependent upwards shift of the energy band has been attributed to the desorption of molecules with increasing temperature [88].

However, based on our observations in the heating process at approximately 160-180 K, physisorbed H₂ molecules are unlikely to alter the E_D position upon desorption. Furthermore, we do not expect the physisorbed H₂ monolayer to significantly modify the phonon frequency because the atomic mass of H₂ is much smaller than that of a Te atom on the surface (the atomic mass ratio is $\sim 2/128=0.016$). As the boiling temperature of H₂ molecules is 20 K, condensation of H₂ molecules on the sample surface above 20 K is unlikely, although the desorption temperature of H₂ molecules may be much higher [70,71].

4.5 Initial-state Energy Dependence of the EPC Parameter

After carefully analyzing the effect of temperature and time on the band dispersion in the previous sections. In this section, we evaluated the initial-state electron energy dependence of the EPI coupling parameters $\lambda_{ep}(\omega')$ based on the gradient of the temperature-dependent $-\text{Im}\Sigma(\vec{k}, \omega'; T)$ at the initial-state electron energies of 0, 50, 100, 150, 200, and 250 meV measured from the DP (DP set to be 0) in the heating process. We obtained $-\text{Im}\Sigma(\vec{k}, \omega'; T)$ from the EDC and MDC analyses.

In the EDC analyses, we fitted the EDCs using a Voigt function at a fixed Gaussian width at each temperature. The $-\text{Im}\Sigma(\omega, T)$ can be directly evaluated from the peak width ($\Delta\varepsilon$) of the EDC at fixed \vec{k} ; namely, $\Gamma(\omega) = 2|\text{Im}\Sigma(\omega)| = \Delta\varepsilon$. Fig. 4.7 (a) shows the temperature dependence of $-\text{Im}\Sigma(\vec{k}, \omega'; T)$ at 0, 50, and 100 meV, and Fig. 4.7(b) at 150, 200, and 250 meV obtained from the EDC analyses.

In the MDC analysis, we fitted the MDCs using the Lorentzian function. We evaluated v_F and ultimately obtained $\text{Im}\Sigma(\vec{k}, \omega; T)$ using relation $\Gamma(\omega) = 2|\text{Im}\Sigma(\omega)| = \hbar v_F \Delta k$. Fig. 4.10(c) shows the temperature-dependent $-\text{Im}\Sigma(\vec{k}, \omega'; T)$ at the initial-state electron energies 50, 100, and 150 meV above the DP obtained from MDC analyses.

The upper panel of Fig. 4.8(a) shows the EPI coupling parameter $\lambda_{ep}(\omega')$ as a function of the initial-state electron energy measured from the DP energy ($\omega' = \omega - E_D$, here E_D is set to zero) along the $\bar{\Gamma} - \bar{K}$ momentum direction. The coupling parameters obtained from the MDC and EDC analyses agree well with each other. The EPI coupling parameter takes a maximum value of $\lambda_{ep} \sim 0.13$ at the DP ($\omega' = 0$), then

decreases with increasing ω' and takes a minimum value of $\lambda_{ep} \sim 0.02$ at $\omega' = 100 - 150$ meV. Then, the coupling parameter slightly increases as the energy increases up to $\lambda_{ep} \sim 0.06$ at $\omega' = 250$ meV. For comparison, we plot the theoretical coupling parameters obtained from the first-principles calculations [64] in Fig. 4.8(a).

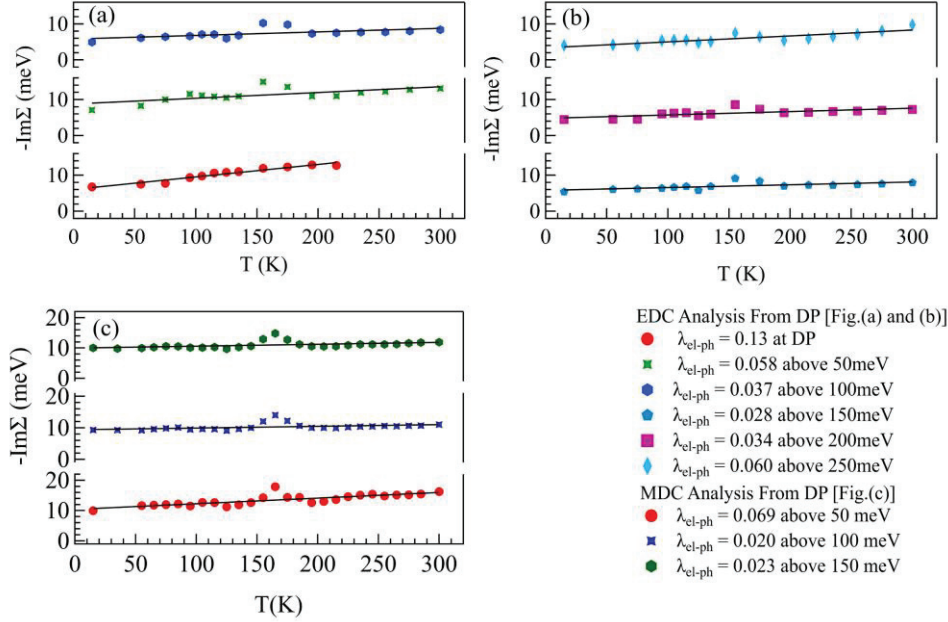


Figure 4.7: Evaluation of coupling parameter. (a) Evaluated $-\text{Im}\Sigma(\vec{k}, \omega'; T)$ at the initial-state electron energies of 0, 50, and 100 meV obtained from EDC analyses. (b) Evaluated $-\text{Im}\Sigma(\vec{k}, \omega'; T)$ at the initial-state electron energies of 150, 200, and 250 meV obtained from EDC analyses. (c) Evaluated $-\text{Im}\Sigma(\vec{k}, \omega'; T)$ at the initial-state electron energies of 50, 100, and 150 meV obtained from the MDC analyses.

The theoretical EPI coupling parameter is $\lambda_{ep} = 0.09-0.12$ near the DP and reduces to $\lambda_{ep} \sim 0.03$ at 150 meV above E_D [64]. Note that the magnitude and the energy dependence of the coupling parameter of the experiments and the first-principles calculations agree well. Our results are also in line with a previous ARPES study, where $\lambda_{ep} \sim 0$ at 100 meV above DP (*p*-type Bi_2Te_3) and $\lambda_{ep} \sim 0.19$ at 350 meV above DP (*n*-type Bi_2Te_3) [41]. First-principles calculations have revealed that the magnitude of the coupling parameter mainly depends on the number of scattering channels rather than the momentum dependence of the EPI matrix element [64]. Hence, the coupling parameter varies in accordance with the theoretical DOS, as shown in the lower panel of Fig. 4.8(a). To confirm this point, we show the imaginary part of the self-energy $-\text{Im}\Sigma(\vec{k}, \omega'; T)$ obtained at 17 K and the angle-integrated photoemission spectrum (AI-PES) in the lower panel of Fig. 4.8(a). Note that taken at a photon energy

of $h\nu = 6.3$ eV, angle integration is conducted only around the TSS over the momentum range of at most $\Delta k_{\parallel} \sim 0.34 \text{ \AA}^{-1}$. Therefore, the AI-PES mainly reflects the DOS derived from the TSS. The energy dependence of the EPI coupling parameter coincides well with that of $-\text{Im}\Sigma(\vec{k}, \omega'; T)$, which clearly indicates a correlation between $\lambda(\omega')$ and the scattering probability. If we compare $-\text{Im}\Sigma(\vec{k}, \omega'; T)$ and the AI-PES, the enhancement of $-\text{Im}\Sigma(\vec{k}, \omega'; T)$ near the DP is more rapid, which suggests more scattering channels into the bulk band near the DP.

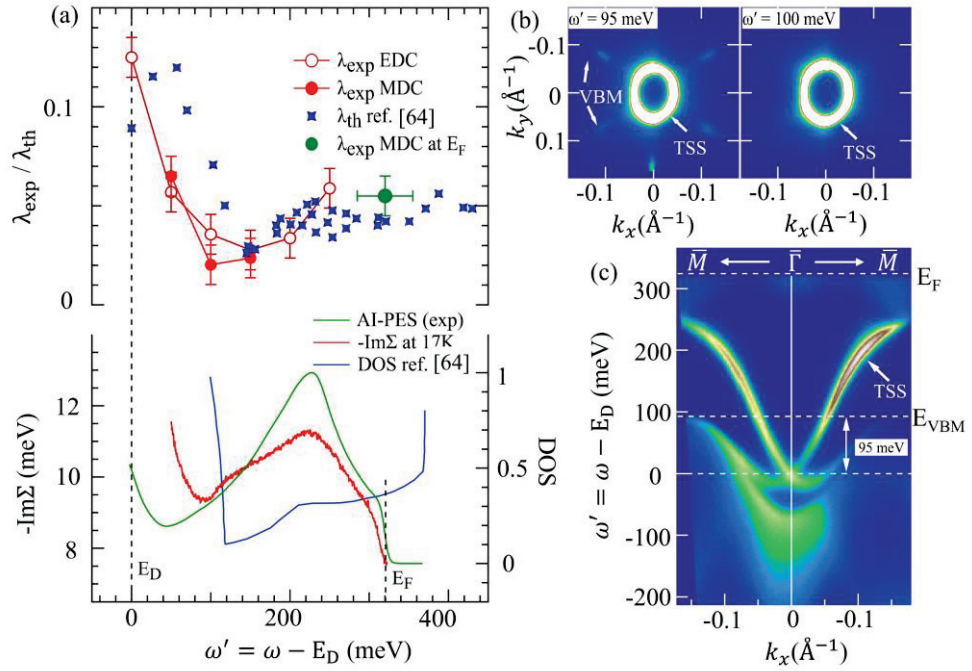


Figure 4.8: Initial energy-dependent EPI coupling parameter. (a) The upper panel shows the EPI coupling parameter as a function of initial-state electron energy with respect to the DP obtained from EDC analyses (open red circles) and MDC analyses (filled red circles). Stars in blue represent the theoretical EPI coupling parameter extracted from ref. [64]. The lower panel illustrates the experimental $-\text{Im}\Sigma(\omega, T)$ at 17 K (red), theoretical DOS (blue), and angle-integrated photoemission spectra (AI-PES in green). (b) Constant energy contours at 17 K showing the appearance (left) and disappearance (right) of the VB maximum. Energies are measured from the DP. (c) ARPES intensity plot along $\bar{\Gamma}-\bar{M}$ at 17 K.

The peak at $\omega' = 0.23$ eV in the AI-PES originated from the maximum of the TSS band along the $\bar{\Gamma} - \bar{M}$ momentum direction, as shown in Fig. 4.8(c). Therefore, the similarity of the TSS-derived AI-PES and $-\text{Im}\Sigma(\vec{k}, \omega'; T)$ in the energy dependence around $\omega' = 0.23$ eV indicates that the scattering channel is mainly restricted inside the TSS. The magnitude of the EPI coupling parameter and

$-\text{Im}\Sigma(\vec{k}, \omega'; T)$ reach the minimum at approximately 100 meV above the DP, where the VB maximum exists along the $\bar{\Gamma} - \bar{M}$ momentum direction, as shown in Fig. 4.8(b). Based on the theoretical and our experimental results, the EPI coupling parameter at E_F is weak, at most $\lambda_{ep} \sim 0.1$, which is consistent with the lack of an appreciable kink structure within the Debye energy range, as shown in Fig. 4.1(d) at 17 K. Our results indicate that EPI scattering can be minimized if we adjust the E_F position to approximately 100 meV above the DP in the case of Bi_2Te_3 .

4.6 Temperature Dependence of the Linewidth at the Fermi Level

As we explained the effect of temperature on band dispersion of Bi_2Te_3 in section 4.4.2. We noticed an upward shift in the whole band spectrum with increasing temperature. In this section, we analyzed the band dispersion at E_F without considering the shift with temperature. Fig. 4.9 shows the temperature dependence of the linewidth at E_F , namely $-\text{Im}\Sigma(0, T)$. one can see that a sudden enhancement is detected at approximately 165 K in $\text{Im}\Sigma(0, T)$ of sample #1 in the heating process. However, in the cooling process (from 300 K to 17 K) measured for sample #2, there is no such anomalous behavior. Besides the narrow temperature range of around 165 K, the temperature dependence of $\text{Im}\Sigma(0, T)$ for both samples overlaps, as shown in Fig. 4.9 (lower panel). Despite the existence of a temperature-dependent energy shift, if we were to evaluate the EPI coupling parameter at E_F based on this result, the value would be 0.05. While this value is lower than those obtained from the kink structure near the E_F at low temperature [41,59], it is closer to the *ab initio* calculation results [64].

4.7 Relaxation Time and Mean Free Path at the Fermi Level

Fig. 4.10 illustrates the temperature-dependent relaxation time and mean free path at E_F . The magnitude of $\text{Im}\Sigma(0, T)$ increased systematically with temperature, as shown in Fig. 4.9, implying an increase in the scattering rate by the phonons. Quasiparticle relaxation time (τ) and mean free path (l) have a direct correspondence with MDC line width [54]. The relaxation time is given by

$$\Gamma(\omega) = \frac{\hbar}{\tau} = 2|\text{Im}\Sigma(\omega)| = \hbar v_F \Delta k. \quad (4.11)$$

The mean free path (l) is given by

$$l = \frac{1}{\Delta k}, \quad (4.12)$$

where v_F is the Fermi velocity, and Δk is the FWHM of the MDC peak evaluated by two Lorentzian peak fits.

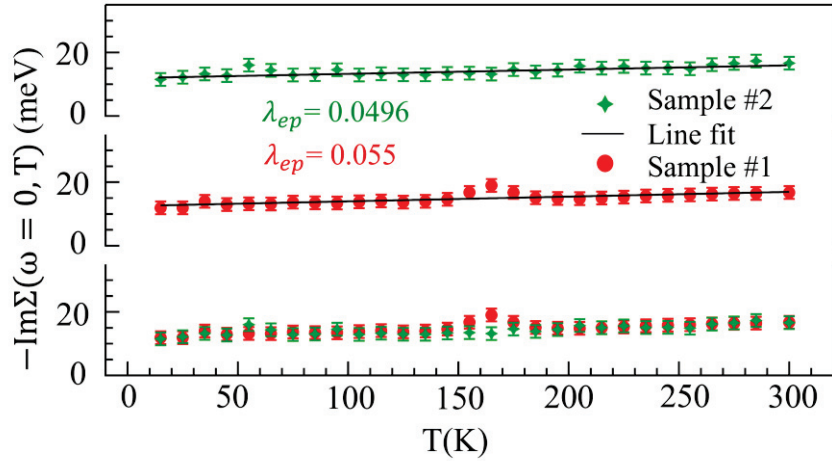


Figure 4.9. Temperature dependence of the linewidth at E_F , $-\text{Im}\Sigma(0, T)$, for two different Bi₂Te₃ samples. Red solid circles and green diamond-like solid shapes denote sample #1 and sample #2, respectively. The lower panel represents the magnitude of the $-\text{Im}\Sigma(0, T)$ of two different samples that overlap. On the other hand, the middle and upper panels represent line fit in the temperature-dependent $-\text{Im}\Sigma(0, T)$ at E_F of sample #1 and sample #2, respectively.

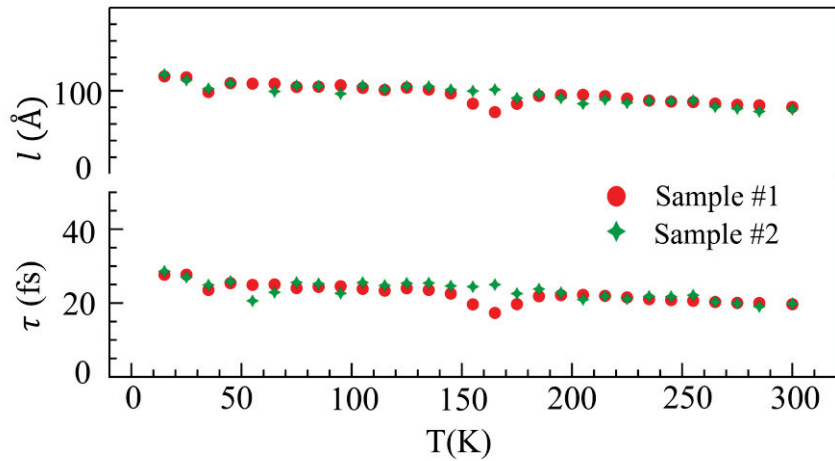


Figure 4.10. Relaxation time (lower panel) and mean free path (upper panel) at the E_F of two samples were evaluated from the temperature-dependent ARPES spectra. Red solid circles and green diamond-like solid shapes are used for sample #1 and sample #2, respectively. The magnitude of the relaxation time and mean free path are almost constant with temperature, implying a negligible change in the scattering at elevated temperatures.

4.8 Temperature Dependence Imaginary part of Self-energy

As we noticed the effect of temperature on the DP energy (E_D) in the previous sections. Here in this section, we will see the effect of temperature on the energy-dependent $-\text{Im}\Sigma(\omega, T)$. Fig. 4.11 shows the temperature dependence of $-\text{Im}\Sigma(\omega, T)$. One can see, $-\text{Im}\Sigma(\omega, T)$ shifted to higher energy with increasing temperature in accordance with the VB and the DP moving towards higher energy. This is consistent with the fact that $-\text{Im}\Sigma(\omega, T)$ reflects the scattering probability (see section 4.6), which is mainly determined by the DOS. The enhancement of $-\text{Im}\Sigma(\omega, T)$ with increasing temperature is mainly derived from the temperature dependence of the Bose–Einstein function.

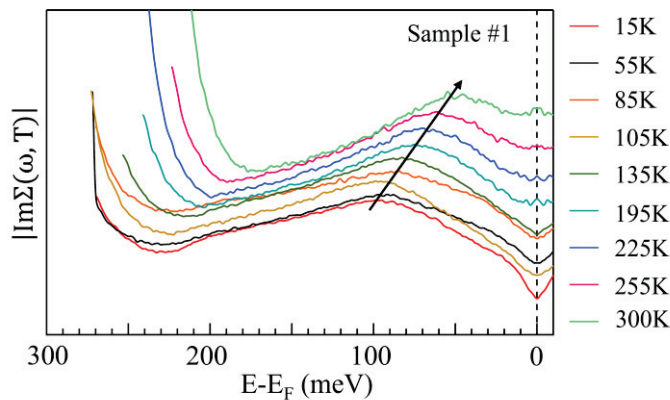


Figure 4.11. The imaginary part of the self-energy ($-\text{Im}\Sigma(\omega, T)$) at various temperatures. The arrow highlights that the peak in $-\text{Im}\Sigma(\omega, T)$ is shifting towards E_F with increasing temperature. We use a vertical offset for better visibility.

4.9 Summary

In conclusion, we examined temperature-dependent band structures and energy dependence of the EPI of the TSS on the n -type Bi_2Te_3 using high-resolution ARPES. We did not find an appreciable kink structure near E_F at low temperature, suggesting fewer EPI in this material. However, we found that temperature-dependent band modification was nonrigid-band-like, and the EPI played a significant role. Despite the temperature-dependent band modification in the bulk, the EDC peak at DP was perfectly fitted at RT using a single Voigt function, suggesting the degeneracy at the DP was robust, showing topological protection. Depending on the initial energy state, the EPI coupling parameter varied from 0.13 (at the DP) to 0.02 (100 meV above the

DP), which was consistent with the reported first-principles calculations. The imaginary part of the self-energy indicated the EPI coupling parameter was determined by the number of scattering channels. Our results provided insight into the physical properties at finite temperatures originated from the TSSs on the 3D TI.

Chapter 5: Conclusion

This thesis is concerned with the investigation of the many-body effects, especially the electron-phonon interaction, of 3D TIs Bi₂Te₃ using laser-based high-resolution angle-resolved photoemission spectroscopy. In the electronic applications of the 3D TIs at room temperature, information on the electron-phonon interaction on the TSS is very crucial because it limits the mean free path, which is directly related to the transport properties of materials derived from the TSS. We should note that the temperature-dependence of the electron-defects interaction and electron-electron interaction is almost negligible. However, the electron-phonon interaction plays a significant role at elevated temperatures. Therefore, in this thesis, we have investigated electron-phonon interaction on the TSSs of Bi₂Te₃ in detail.

In this study, we have grown a Bi₂Te₃ single crystal using the modified Bridgeman method. High-resolution ARPES measurements indicated that the grown sample was an *n*-type semiconductor, showing the bulk CB near E_F . We did not observe an appreciable kink structure in the band dispersion close to the E_F within the energy resolution limit ($< 3\text{meV}$) at 17K. Therefore, we ran the temperature-dependent ARPES measurement from low temperature to RT. Early temperature-dependent band dispersion indicated that the DP was shifting upward with increasing temperature. However, we found that the magnitude of the shift is different from the shift in the DP, which indicate that the bulk band shift is non-rigid-band like. We also analyzed the temperature dependence of the topological surface state 100 meV above the DP, we found that wave vector (k) is increasing and group velocity (v) is decreasing with increasing temperature. It indicates that the Dirac cone is suppressed along the energy axis with increasing temperature, which is also non-rigid-band like behavior. This non-rigid-band like TSSs modification is one of the major findings of the present study. Despite the non-rigid-like bulk and topological surface state nature, we did not observe any gap at DP at both low temperature and RT, which clearly indicates topological protection. As we noticed bulk and surface bands are shifting with increasing temperature, we selected initial states at fixed energy with respect to DP energy at each temperature and evaluated the electron-phonon coupling parameter at each fixed initial energy. By analyzing the momentum distribution curve and energy distribution

curve, the magnitude of the coupling parameter is found to weakly depend on the initial electron state energy. The magnitude of the electron-phonon coupling parameter varies from 0.13 (at the DP) to 0.02 (100 meV above the DP). These values are consistent with the first-principle calculations.

Our findings reveal the delicate temperature-dependent band modification (Surface and bulk) and lifetime derived from the electron-phonon interaction in Bi_2Te_3 . Our method to evaluate the electron-phonon coupling can be also applied to other TIs such as Bi_2Se_3 .

References

- [1] X.-L. Qi and S.-C. Zhang, *Reviews of Modern Physics* **83**, 1057 (2011).
- [2] M. Z. Hasan and C. L. Kane, *Reviews of Modern Physics* **82**, 3045 (2010).
- [3] K. von Klitzing, G. Dorda, and M. Pepper, *Physical Review Letters* **45**, 494 (1980).
- [4] W. Tian, W. Yu, J. Shi, and Y. Wang, *Materials (Basel)* **10** (2017).
- [5] C. L. Kane and E. J. Mele, *Physical Review Letters* **95**, 4, 226801 (2005).
- [6] B. A. Bernevig, Hughes, T. L. & Zhang, S. C, *Science* **314**, 1757 (2006).
- [7] X.-L. Qi and S.-C. Zhang, *Physics Today* **63**, 33 (2010).
- [8] L. Fu and C. L. Kane, *Physical Review B* **76**, 17, 045302 (2007).
- [9] H. J. Zhang, C. X. Liu, X. L. Qi, X. Dai, Z. Fang, and S. C. Zhang, *Nat Phys* **5**, 438 (2009).
- [10] J. G. Analytis, J.-H. Chu, Y. Chen, F. Corredor, R. D. McDonald, Z. X. Shen, and I. R. Fisher, *Physical Review B* **81** (2010).
- [11] D. Hsieh *et al.*, *Nature* **460**, 1101 (2009).
- [12] Y. L. Chen *et al.*, *Science* **325**, 178 (2009).
- [13] N. Kumar, S. N. Guin, K. Manna, C. Shekhar, and C. Felser, *Chem Rev* **121**, 2780 (2021).
- [14] Y. Ando, *Journal of the Physical Society of Japan* **82**, 102001 (2013).
- [15] M. Z. Hasan and J. E. Moore, *Annual Review of Condensed Matter Physics* **2**, 55 (2011).
- [16] J. E. Moore, *Nature* **464**, 194 (2010).
- [17] D. R. Cooper *et al.*, *ISRN Condensed Matter Physics* **2012**, 1 (2012).
- [18] R. B. Laughlin, *Physical Review Letters* **50**, 1395 (1983).
- [19] D. C. Tsui, H. L. Stormer, and A. C. Gossard, *Physical Review Letters* **48**, 1559 (1982).
- [20] F. D. M. Haldane, *Physical review letters* **61**, 2015 (1988).
- [21] K. He, Y. Wang, and Q.-K. Xue, *Natl. Sci. Rev.* **1**, 38 (2013).
- [22] M. V. Berry, *Proc. R. Soc. Lond. A-Math. Phys. Sci.* **392**, 45 (1984).
- [23] T. Ando and Y. Uemura, *Journal of the Physical Society of Japan* **36**, 959 (1974).
- [24] D. J. Thouless, M. Kohmoto, M. P. Nightingale, and M. den Nijs, *Physical review letters* **49**, 405 (1982).
- [25] J. Maciejko, T. L. Hughes, and S.-C. Zhang, *Annual Review of Condensed Matter Physics* **2**, 31 (2011).
- [26] L. Fu, C. L. Kane, and E. J. Mele, *Physical Review Letters* **98**, 4, 106803 (2007).
- [27] D. Hsieh, D. Qian, L. Wray, Y. Xia, Y. S. Hor, R. J. Cava, and M. Z. Hasan, *Nature* **452**, 970 (2008).
- [28] A. Nishide *et al.*, *Physical Review B* **81**, 4, 041309 (2010).
- [29] Y. Xia *et al.*, *Nat Phys* **5**, 398 (2009).
- [30] D. Hsieh *et al.*, *Physical Review Letters* **103**, 4, 146401 (2009).
- [31] P. Roushan *et al.*, *Nature* **460**, 1106 (2009).
- [32] L. Plucinski, *J Phys Condens Matter* **31**, 183001 (2019).
- [33] D. Pesin and A. H. MacDonald, *Nat. Mater.* **11**, 409 (2012).
- [34] W. Z. Rui Yu, Hai-Jun Zhang, Shou-Cheng Zhang, Xi Dai, and Zhong Fang, *Science* **329**, 61 (2010).
- [35] L. Fu and C. L. Kane, *Physical Review Letters* **100**, 4, 096407 (2008).
- [36] L. A. Fu and E. Berg, *Physical Review Letters* **105**, 4, 097001 (2010).
- [37] R. L. Xiao-Liang Qi, Jiadong Zang, and Shou-Cheng Zhang, *Science* **323**, 1184 (2009).
- [38] Y. S. Hor, A. Richardella, P. Roushan, Y. Xia, J. G. Checkelsky, A. Yazdani, M. Z. Hasan, N. P. Ong, and R. J. Cava, *Physical Review B* **79**, 5, 195208 (2009).
- [39] R. J. Cava, H. W. Ji, M. K. Fuccillo, Q. D. Gibson, and Y. S. Hor, *J. Mater. Chem. C* **1**, 3176 (2013).

-
- [40] T. Shinjo, *Nanomagnetism and spintronics* (Elsevier, 2013).
- [41] C. Chen *et al.*, *Sci Rep* **3**, 2411 (2013).
- [42] B. K. Gupta *et al.*, *Scientific Reports* **8**, 6, 9205 (2018).
- [43] A. Singh *et al.*, *Materials Research Bulletin* **98**, 1 (2018).
- [44] H. F. Yang, A. J. Liang, C. Chen, C. F. Zhang, N. B. M. Schroeter, and Y. L. Chen, *Nature Reviews Materials* **3**, 341 (2018).
- [45] A. Damascelli, Z. Hussain, and Z. X. Shen, *Reviews of Modern Physics* **75**, 473 (2003).
- [46] D. H. Lu, I. M. Vishik, M. Yi, Y. L. Chen, R. G. Moore, and Z. X. Shen, in *Annual Review of Condensed Matter Physics, Vol 3*, edited by J. S. Langer (Annual Reviews, Palo Alto, 2012), pp. 129.
- [47] B. Q. Lv, T. Qian, and H. Ding, *Nature Reviews Physics* **1**, 609 (2019).
- [48] D. Lu, I. M. Vishik, M. Yi, Y. Chen, R. G. Moore, and Z.-X. Shen, *Annual Review of Condensed Matter Physics* **3**, 129 (2012).
- [49] H. Hertz, *Ann. Phys.-Berlin* **267**, 983 (1887).
- [50] A. Einstein, *Ann. Phys.-Berlin* **4** (1905).
- [51] S. Hüfner, *Photoelectron spectroscopy: principles and applications* (Springer Science & Business Media, 2013).
- [52] A. Zangwill, *Physics at surfaces* (Cambridge university press, 1988).
- [53] H. Iwasawa, E. F. Schwier, M. Arita, A. Ino, H. Namatame, M. Taniguchi, Y. Aiura, and K. Shimada, *Ultramicroscopy* **182**, 85 (2017).
- [54] P. Hofmann, I. Y. Sklyadneva, E. D. L. Rienks, and E. V. Chulkov, *New Journal of Physics* **11**, 125005 (2009).
- [55] N. Fischer, S. Schuppler, R. Fischer, T. Fauster, and W. Steinmann, *Physical Review B* **43**, 14722 (1991).
- [56] S. R. Park, W. S. Jung, C. Kim, D. J. Song, C. Kim, S. Kimura, K. D. Lee, and N. Hur, *Physical Review B* **81**, 041405 (2010).
- [57] R. C. Hatch, M. Bianchi, D. Guan, S. Bao, J. Mi, B. B. Iversen, L. Nilsson, L. Hornekaer, and P. Hofmann, *Physical Review B* **83**, 241303 (2011).
- [58] Z. H. Pan, A. V. Fedorov, D. Gardner, Y. S. Lee, S. Chu, and T. Valla, *Phys Rev Lett* **108**, 187001 (2012).
- [59] T. Kondo *et al.*, *Phys Rev Lett* **110**, 217601 (2013).
- [60] X. Zhu, L. Santos, R. Sankar, S. Chikara, C. Howard, F. C. Chou, C. Chamon, and M. El-Batanouny, *Phys Rev Lett* **107**, 186102 (2011).
- [61] X. Zhu, L. Santos, C. Howard, R. Sankar, F. C. Chou, C. Chamon, and M. El-Batanouny, *Phys Rev Lett* **108**, 185501 (2012).
- [62] A. Tamtögl *et al.*, *Physical Review B* **95**, 195401 (2017).
- [63] G. Q. Huang, *EPL (Europhysics Letters)* **100**, 17001 (2012).
- [64] R. Heid, I. Y. Sklyadneva, and E. V. Chulkov, *Sci Rep* **7**, 1095 (2017).
- [65] H. J. Goldsmid, *Materials* **7**, 2577 (2014).
- [66] T. Hanaguri, K. Igarashi, M. Kawamura, H. Takagi, and T. Sasagawa, *Physical Review B* **82**, 081305 (2010).
- [67] P. Nozieres, *Theory of interacting Fermi systems* (Benjamin, 1964).
- [68] G. Grimvall, (The Electron-Phonon Interaction in Metals NorthHolland, Amsterdam, 1981).
- [69] G. D. Mahan, *Many-particle physics* (Kluwer Academic/Plenum Publishers, New York, 2000).
- [70] P. B. Allen and M. Cardona, *Physical Review B* **23**, 1495 (1981).
- [71] X. C. K. P. O'Donnell, *Applied Physics Letters* **58**, 2924 (1991).
- [72] N. W. Ashcroft and a. N. D. Mermin, *Solid state physics* (Sanders College Publishing, Philadelphia, 1976) Chap. 2

-
- [73] D. Kim, Q. Li, P. Syers, N. P. Butch, J. Paglione, S. Das Sarma, and M. S. Fuhrer, *Phys Rev Lett* **109**, 166801 (2012).
- [74] M. V. Costache, I. Neumann, J. F. Sierra, V. Marinova, M. M. Gospodinov, S. Roche, and S. O. Valenzuela, *Physical Review Letters* **112**, 086601 (2014).
- [75] C. Howard, M. El-Batanouny, R. Sankar, and F. C. Chou, *Physical Review B* **88**, 035402 (2013).
- [76] C. Howard and M. El-Batanouny, *Physical Review B* **89**, 075425 (2014).
- [77] A. Ruckhofer, D. Campi, M. Bremholm, P. Hofmann, G. Benedek, M. Bernasconi, W. E. Ernst, and A. Tamtögl, *Physical Review Research* **2**, 023186 (2020).
- [78] E. W. Plummer, J. R. Shi, S. J. Tang, E. Rotenberg, and S. D. Kevan, *Progress in Surface Science* **74**, 251 (2003).
- [79] J. Sánchez-Barriga, M. R. Scholz, E. Golias, E. Rienks, D. Marchenko, A. Varykhalov, L. V. Yashina, and O. Rader, *Physical Review B* **90**, 195413 (2014).
- [80] S. Raghu, S. B. Chung, X. L. Qi, and S. C. Zhang, *Phys Rev Lett* **104**, 116401 (2010).
- [81] S. Giraud and R. Egger, *Physical Review B* **83**, 245322 (2011).
- [82] S. Giraud, A. Kundu, and R. Egger, *Physical Review B* **85**, 035441 (2012).
- [83] S. Das Sarma and Q. Li, *Physical Review B* **88**, 081404 (2013).
- [84] V. Parente, A. Tagliacozzo, F. von Oppen, and F. Guinea, *Physical Review B* **88**, 075432 (2013).
- [85] N.W. Ashcroft and N. D. Mermin, *Chap. 26. Solid State Physics* Sanders College Publishing, Philadelphia, 1976).
- [86] J. Jiang, K. Shimada, H. Hayashi, H. Iwasawa, Y. Aiura, H. Namatame, and M. Taniguchi, *Physical Review B* **84**, 155124 (2011).
- [87] G. Grimvall, (*The Electron-Phonon Interaction in Metals*(NorthHolland, Amsterdam, 1981)).
- [88] E. Frantzeskakis *et al.*, *Physical Review B* **91**, 15, 205134 (2015).
- [89] R. Jiang, L. L. Wang, M. L. Huang, R. S. Dhaka, D. D. Johnson, T. A. Lograsso, and A. Kaminski, *Physical Review B* **86**, 4, 085112 (2012).
- [90] J. Nayak, G. H. Fecher, S. Ouardi, C. Shekhar, C. Tusche, S. Ueda, E. Ikenaga, and C. Felser, *Physical Review B* **98**, 075206 (2018).
- [91] K. P. Odonnell and X. Chen, *Applied Physics Letters* **58**, 2924 (1991).
- [92] S. R. Park *et al.*, *New Journal of Physics* **13**, 013008 (2011).
- [93] P. D. C. King *et al.*, *Physical Review Letters* **107**, 5, 096802 (2011).
- [94] K. Sakamoto *et al.*, *Nano Lett.* **21**, 4415 (2021).
- [95] M. S. Bahramy *et al.*, *Nat. Commun.* **3**, 7, 1159 (2012).
- [96] Z. H. Zhu *et al.*, *Physical Review Letters* **107**, 5, 186405 (2011).
- [97] E. Frantzeskakis *et al.*, *Sci Rep* **5**, 16309 (2015).
- [98] E. Frantzeskakis *et al.*, *Physical Review X* **7**, 16, 041041 (2017).
- [99] A. A. Kordyuk, T. K. Kim, V. B. Zabolotnyy, D. V. Evtushinsky, M. Bauch, C. Hess, B. Buchner, H. Berger, and S. V. Borisenko, *Physical Review B* **83**, 4, 081303 (2011).
- [100] M. S. Hofman, D. Z. Wang, Y. Yang, and B. E. Koel, *Surf. Sci. Rep.* **73**, 153 (2018).
- [101] R. A. Ciufu, S. M. Han, M. E. Floto, J. E. Eichler, G. Henkelman, and C. B. Mullins, *Phys. Chem. Chem. Phys.* **22**, 15281 (2020).

Acknowledgments

First and foremost, I would like to express my sincere gratitude to my advisor Prof. K. Shimada for his mentorship and support. He has been a constant source of support, encouragement, and advice throughout my graduate studies. Prof. Shimada is a very busy person, but he always makes time for me to discuss whenever I ask, and he patiently explains everything until I am satisfied. Prof. Shimada has provided me with a lot of care and support in my daily life, making me feel unendingly warm. Moreover, I am very grateful to him for the freedom and positive research environment he gave me. He allowed me to proceed with my own project and consult with experts in material synthesis, ARPES technique, etc. I sincerely thank Prof. K. Shimada for every single aspect of my graduate research.

I owe a debt of gratitude to my group's colleagues and friends. I wish to thank Dr. Shiv Kumar, Mr. Yudai Miyai, Dr. Eike F. Schwier, Dr. Zhank ke, and Mr. Wumiti Mansuer for introducing me to the group and helping me to settle down. When I joined my Ph.D, Miyai helped me a lot with doing initial paperwork which was in Japanese, and continuously helped throughout my Ph.D., Whenever I received some documents in Japanese. We often discuss ARPES, data analysis, etc. I would like to say special thanks to Shiv Kumar; He teach me to how to prepare the sample and run experiments in my initial days; and also helped me a lot in my personal life and make me comfortable during my initial days. I thank Eike F. Schwier for his infinite curiosity, although he left HiSOR after eight months of my joining but he taught me a lot about ARPES and always explained it in many different ways. Wumiti Mansuer taught me about Laser ARPES and was extremely generous as a teacher cum friend when I started to work with ARPES on topological insulators. I would like to thank my other lab members Mr. Yogendra Kumar, Mr. Ishiba, Mr. Sobota.

I would like to express my sincere gratitude for the kind and intellectual guidance from Prof. Taichi Okuda, Prof S. Ideta, Prof. Kenta Kuroda, Prof. Akio Kimura, and Prof. K. Miyamoto. Prof. Sato, for the kind support and professional advice during my graduate study. Prof. Taichi Okuda always points out an essential idea whenever I discussed with him. I would like to express special thanks to Prof. M. Arita; he is the one who knows the solution of everything inside HiSOR.

I would also like to thank Prof T. Onimaru, and Prof. Matsumura for allowing me to use their facilities such as X-ray diffraction, and magnetic and resistivity measurements during my graduate studies. Furthermore, I would say special thanks to Ms. Rikako for giving her precious time during XRD measurement and for helping me with magnetic measurements.

I am thankful to the HiSOR office staff, especially Ms. Shinno San and Ms. Shimokubo for helping in the documentation during my graduate study. I am also grateful to the Graduate School of Science, Department of physics, for their constant support during my studies. I would like to thank Ms. Akimura San for always providing important information about scholarships.

I would like to thank my friends Gajender Thakur, Shumojit Ghosh, and Thomas, which I earn during my graduate studies at Hiroshima University.

I am incredibly grateful to Prof. Surekha Tomar for her kind support, and motivation and for treating me as her own child. I am also very thankful to Prof. Gaurang Misra for his continuous guidance. I would like to express my sincere gratitude for the kind and intellectual guidance from Prof. Preetam Singh.

I would like to thank my senior cum friends from India Dr. Abhishek Singh, Dr. Bhijmohan Prajapati, Dr. Keshav Kumar, Dr. Satyaveer Singh, and Dr. Pragya Singh. I spent my best time with Abhishek Singh at the IIT (BHU), and frequently discussed research problems with him during my graduate studies, whenever I was stuck in something. Keshav Kumar and Pragya Singh were the best labmates during the Master's course I ever met. In fact, I learn how to do research from them.

I would like to thank my best friend Ramgopal Agrawal for his constant support, guidance, listening to my silly talks, and the good time we shared together. I would also like to thank Himanshu Mishra for the useful discussion. I earned some good friends during my BHU days, I would like to thank Abhay, Shyam, Manish, Pragyan, Anupam, Kapil, Shivam, Saurabh, Priya, Shanu, Pooja, Krishna, and Rajnandini. I spend quality time with them all during my BHU days. I special thanks to Rajnandini Sharma for helping me with the interview preparation and for her positive thinking and encouragement.

I want to express my deepest gratitude to my family, who always supported me unconditionally throughout my entire career. I especially thank my mother, father, and Mama, who has been the greatest source of inspiration in my whole life. I also thank my sister for her love and care. I also thank Ms. Sonam, for her unconditional support and sticking with me.

Last but not least, I would like to thank **Lord Krishna**.

Thank you all!

Amit Kumar

22 August 2022

